

Spring 5-30-2015

# The Investigation of the Low Temperature Combustion of Mesitylene and Tert-Amyl Methyl Ether by Synchrotron Photoionization Mass Spectrometry

Martin Yu-Hin Ng  
martinngyh@gmail.com

Follow this and additional works at: <https://repository.usfca.edu/thes>

 Part of the [Analytical Chemistry Commons](#), and the [Physical Chemistry Commons](#)

---

## Recommended Citation

Ng, Martin Yu-Hin, "The Investigation of the Low Temperature Combustion of Mesitylene and Tert-Amyl Methyl Ether by Synchrotron Photoionization Mass Spectrometry" (2015). *Master's Theses*. 145.  
<https://repository.usfca.edu/thes/145>

This Thesis is brought to you for free and open access by the Theses, Dissertations, Capstones and Projects at USF Scholarship: a digital repository @ Gleeson Library | Geschke Center. It has been accepted for inclusion in Master's Theses by an authorized administrator of USF Scholarship: a digital repository @ Gleeson Library | Geschke Center. For more information, please contact [repository@usfca.edu](mailto:repository@usfca.edu).

**The Investigation of the Low Temperature Combustion of  
Mesitylene and Tert-Amyl Methyl Ether by Synchrotron  
Photoionization Mass Spectrometry**

To the Department of Chemistry  
of the University of San Francisco  
in partial fulfillment of the requirements of  
Masters of Science in Chemistry

A thesis written by

Martin Yu-Hin Ng

Bachelor of Science in Biochemistry and Molecular Biology

the University of California, Davis

The Thirtieth of May, 2015

**The Investigation of the Low Temperature Combustion of  
Mesitylene and Tert-Amyl Methyl Ether by Synchrotron  
Photoionization Mass Spectrometry**

Thesis written by Martin Yu-Hin Ng

This thesis is written under the guidance of Faculty Advisory Committee, and approved by all its members, has been accepted in partial fulfillment of the requirements of the degree of

**Masters of Science in Chemistry  
at  
the University of San Francisco**

Thesis Committee

Giovanni Meloni, PhD.  
Research Director

Lawrence Margerum, PhD.  
Professor

William Melaugh, PhD.  
Professor

Marcelo Camperi, PhD.  
Dean, College of Art and Sciences

## **Acknowledgement**

Before attending the Masters' program in chemistry here at USF, I would not have imagined that I could do science in the field of physical chemistry, publish a paper in a scientific journal and visit the state of the art synchrotron radiation facility at the Advanced Light Source that one can only read from textbooks. I am extremely grateful to Dr. Giovanni Meloni for giving me these wonderful opportunities and guidance that made me a little more skillful scientist. I also thank our collaborators at the Sandia National Laboratories, Craig Taatjes, David Osborn, Oliver Welz and John Savee. It was a joy to work with them and learn from these good scientists.

The Chemistry Department at USF has provided me with their support during my stay there. Special thanks go to Dr. Lawrence Margerum and Dr. William Melaugh for their resourceful input on my thesis. I also enjoyed teaching laboratories classes, and I want thank Javier Lacayo and Angela Qin for their help with laboratories supplies. Furthermore, I would like to thank Deidre Shymanski for coordinating the program, conversing with me when she was extremely busy and of course helping me in the thesis submission process.

Finally, I want to thank my family for their nourishment over the years. Without their support, I could not have walked this far. In addition, the consultations I obtained from my friends were a tremendous help.

## Table of Contents

<b>Abstract</b>	<b>1</b>
<b>Chapter 1 - Introduction</b>	<b>2</b>
1.1 Energy Consumption	2
1.2 Health Problems and Climate Change Due to Air Pollution—the Price for Urban Development	3
1.3 Understanding Combustion	4
1.4 Homogenous Charged Compression Ignition (HCCI) Engine—a Newer and Cleaner Engine.	5
1.5 An Overview of the Thesis	7
1.6 References	8
<b>Chapter 2 - Experimental Set-up: The Multiplexed Chemical Kinetics Mass Spectrometer Coupled to the Advanced Light Source</b>	<b>10</b>
2.1 The Advanced Light Source	10
2.2 The ALS Components	11
2.2.1 Linear Accelerator	12
2.2.2 Booster Ring and Storage Ring	13
2.2.3 Insertion Devices	14
2.2.4 Gas Filter and Monochromator at Beamline 9.0.2	15
2.3 The Experimental Apparatus	17
2.3.1 Tracing the Molecules—From the Slow-Flow Reaction Cell to the MCP Ion Detector	18
2.3.2 The Excimer Laser	20
2.3.3 Vacuum Pumps	23
2.3.4 Time-of-flight Mass Spectrometer and Microchannel Plates	26

2.4 References	29
<b>Chapter 3 - Data Analysis, Photoionization Theories, and Ab Initio Computational Methods</b>	<b>32</b>
3.1 Data Cycles and Data Processing	32
3.2 Photoionization	35
3.3 Vertical transitions, Frank-Condon Principle and Frank-Condon Factor	36
3.4 Photoionization Spectra and Photoionization Cross-Section	40
3.5 Electronic Structure Calculations	42
3.5.1 Density Functional Theory	43
3.5.2 B3LYP Method and Basis Sets	43
3.5.3 Coupled-Cluster Methods	45
3.5.4 CBS-QB3 Method	46
3.6 Using Theoretical Methods	47
3.7 References	49
<b>Chapter 4 - Synchrotron Photoionization Study of Mesitylene Oxidation Initiated by Reaction with Cl (<sup>2</sup>P) or O (<sup>3</sup>P) Radicals</b>	<b>53</b>
4.1 Abstract	53
4.2 Introduction	53
4.3 Experiment	57
4.4 Computational Methods	62
4.5 Result and Analysis	63
4.5.1 Mesitylene + Cl + O <sub>2</sub> Reaction at Room Temperature	63
4.5.2 Mesitylene + O ( <sup>3</sup> P) at Room Temperature and 823 K	73
4.6 Conclusions	78
4.7 Figures and Tables	79

4.8 References	93
<b>Chapter 4S - Supporting Information for Chapter 4</b>	<b>99</b>
4S.1 Supporting Material	99
4S.1.1 Photoionization of 3,5-Dimethylbenzaldehyde	99
4S.1.2 Identification of Secondary Products	100
4S.2 Supplemental Figures	101
4S.3 References	103
<b>Chapter 5 - The Study of Tert-Amyl Methyl Ether Low Temperature Oxidation Using Synchrotron Photoionization Mass Spectrometry</b>	<b>104</b>
5.1 Abstract	104
5.2 Introduction	104
5.3 Experiment	106
5.4 Computational Methods	110
5.5 Discussion and Analysis	111
5.5.1 Product Identification of TAME + Cl + O <sub>2</sub> at 298 K	112
5.5.2 Product Identification of TAME + Cl + O <sub>2</sub> at 550 K	114
5.5.3 Product Identification of TAME + Cl + O <sub>2</sub> at 700 K	116
5.6 Proposed mechanism of TAME + Cl + O <sub>2</sub>	119
5.7 Branching Fractions	132
5.8 Conclusions	136
5.9 References	138
5.10 Figures and Tables	142

## **Abstract**

This thesis describes the combustion experiments performed at the Chemical Dynamics Beamline of the Advanced Light Source (ALS) located at the Lawrence Berkeley National Laboratories (LBNL). The need for renewable fuel sources, the need for the study of their combustion in the contexts of homogenous charge combustion ignition (HCCI) engines can be found in Chapter 1. The components of the experimental set-up used throughout this thesis—time-of-flight mass spectrometer, Excimer laser, vacuum pumps and other components—and the components of ALS responsible in synchrotron radiation generation and processing—the linear accelerator, the booster ring, insertion devices, gas filters and monochromator are explained in Chapter 2. The data analysis method and the computational method used in the data analysis are expounded in Chapter 3.

There are two combustion systems being investigated in this thesis. Mesitylene, an aromatic fuel additive, is proposed to be jet fuel, and its combustion is described in Chapter 4. Semi-biorenewable tert-amyl methyl ether (TAME) is studied in Chapter 5. Thermodynamic calculations, proposed mechanism, product identification and branching fractions are included in the analysis of the combustion of all these molecules.



## **Chapter 1 - Introduction**

### **1.1 Energy Consumption**

Thousand years ago, civilizations developed along regions where water was abundant. A sustainable source of water was essential to the everyday lives of our ancestors because it facilitated agriculture, which provided food in the form of grains and livestock. In ancient times, animals were the means of transportation. Also, simple machineries for agriculture were powered by both humans and animals. Hence, food was the main source of energy. With large and sophisticated water infrastructures and agriculture that provided ample energy, these ancient civilizations were able to expand their territories by constructing more buildings and roads.

In the modern age, the global society still requires energy in order to sustain itself and develop. Nevertheless, transportation is no longer powered by animals, but mainly by electricity and fossil fuels, such as oil, coal, and natural gas. These energy sources are also used in agriculture. Therefore, energy can be easily considered as a cost for civilization development. As seen in Figure 1-1, the total world fossil fuel consumption has an acclivity since 1965 according to British Petroleum.<sup>1</sup>

The demand of fossil fuel has increased, but so has the demand of electricity. According to Koomey, the total electricity used in the world had doubled from 2000 to 2005.<sup>2</sup> Communication has changed from physical (letters) to semi-physical (telephone conversations) then to entirely electronic (emails and text messages). Contemporary communication methods do not require transportation means, but electronic devices like personal computers, smartphones, and tablet computers. Electricity, which is becoming more essential to our daily lives, mainly originates from

fuel sources like fossil combustibles. In 2014, about 67% of the electricity was produced from fossil fuel in the United States.<sup>3</sup>

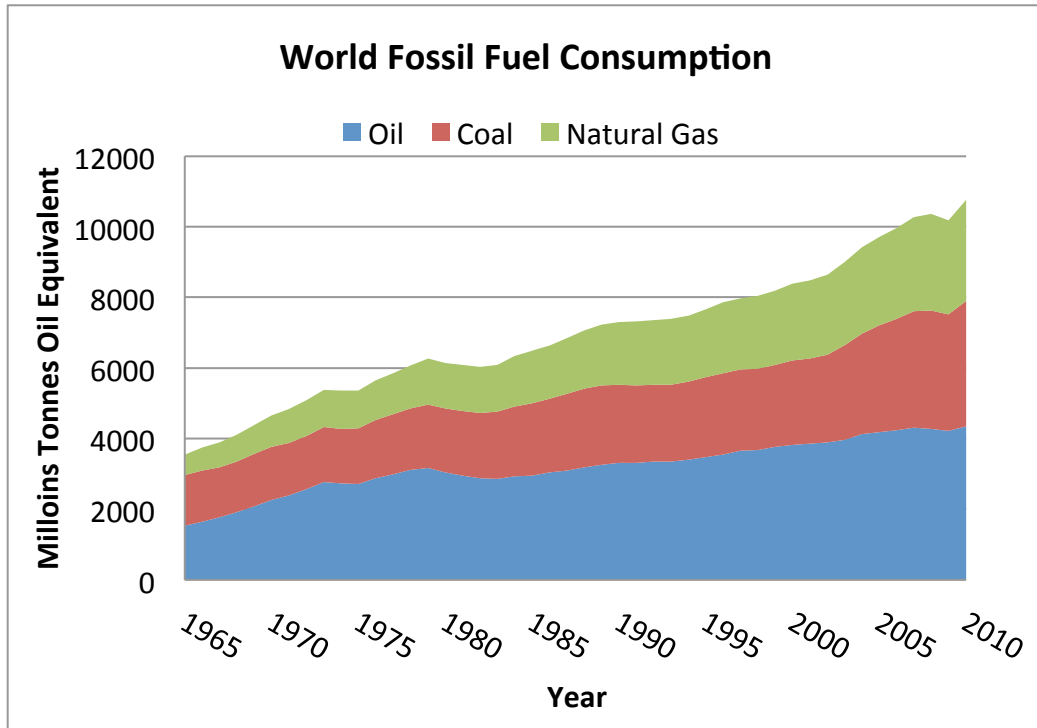


**Figure 1-1.** Historic data of the world consumption of fossil fuel. Data are adopted from the BP Statistical Review of World Energy June 2011.<sup>1</sup>

## 1.2 Health Problems and Climate Change Due to Air Pollution—the Price for Urban Development

Fossil fuels have to be burned either in power plants or in internal combustion engines to produce energy or electricity. When fossil fuels burn, particulate matter (PM), nitrogen oxides (NO<sub>x</sub>), and carbon oxides (CO<sub>x</sub>) are emitted in combustion exhaustion.<sup>4</sup> These chemicals are harmful to the environment and human health.<sup>5-7</sup> NO<sub>x</sub> and CO<sub>x</sub> are green house gases, which may increase the Earth surface temperature through greenhouse effect. Besides impacting climate, NO<sub>x</sub> increases

susceptibility to respiratory infection, airway resistance in asthmatics, and decreases pulmonary function.<sup>5-7</sup> On the other hand, PM is thought to be causing health problems like premature death, respiratory and cardiovascular diseases,<sup>7</sup> whereas some PMs are carcinogens.<sup>8-9</sup>

### 1.3 Understanding Combustion

Because combustion is related to energy consumption and air pollution, there is a need to understand the chemistry behind the energy-giving process. By understanding combustion chemistry, more efficient and cleaner engines can be designed and produced. Combustion is traditionally represented using the following equation:



Judging from the variety of chemicals detected from combustion exhaust, it is intuitive that combustion of fossil fuels, which are usually hydrocarbons, is far more complicated than the simple reaction equation above. Indeed, the combustion of natural gas, which is methane and the simplest hydrocarbon, involves many pathways, leading to many reaction intermediates and products, depicted in a simplified schematic (Figure 1-2). As depicted in the schematic below, hydroxyl radical (OH) plays a very important role in the combustion of a hydrocarbon. The ground state oxygen atom, symbolized by  $\text{O}(^3\text{P})$ , where 3 denotes the spin multiplicity and P its term symbol, is also involved in oxidation processes. The combustion of a hydrocarbon is initiated through hydrogen abstraction. This reaction is one of the main foci of this thesis. Also it is noteworthy that formaldehyde, methyl radical,

methoxy radical, and carbon monoxide are amongst the by-products of the combustion of methane when the fuel is not completely combusted.

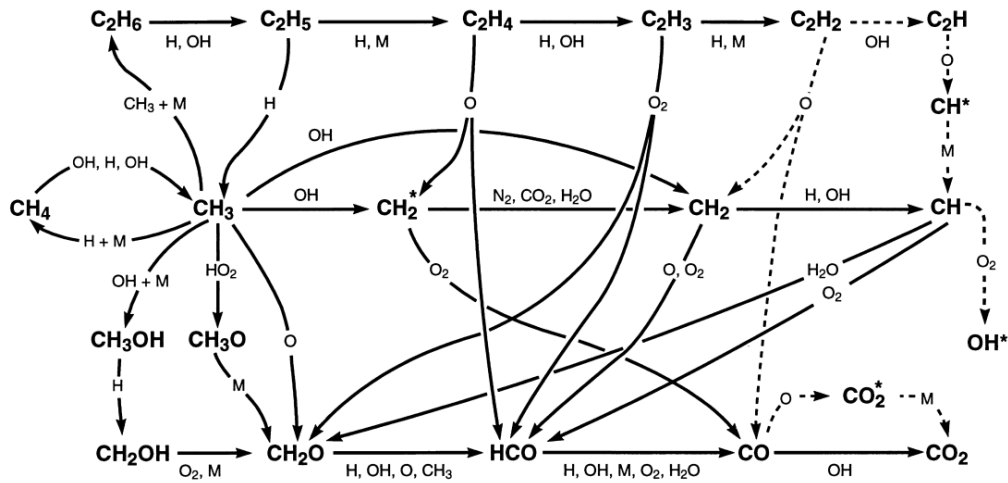


**Figure 1-2.** A simplified combustion mechanism of methane in a premixed methane-air flame with a stoichiometric 20% nitrogen-diluted reactant mixture at room temperature.<sup>10</sup>

#### 1.4 Homogenous Charged Compression Ignition (HCCI) Engine—a Newer and Cleaner Engine.

Currently, energy from fuel is produced in two types of internal combustion engines, gasoline and diesel. As depicted in Figure 1-3, these two engines require an ignition source, usually provided by a spark. Then, the combustion flame propagates among the air/fuel mixture and throughout the entire combustion chamber. Because there is only one point of ignition, there is one propagation front. The efficiency of gasoline engines is limited because the air/fuel mixture has to be near-stoichiometric, and the compression ratio is limited to 10:1 (the ratio of the largest capacity of a combustion chamber to the smallest capacity of the same chamber) to avoid knocking.<sup>11</sup> Engine knocking occurs when unburnt gases are

expanded and autoignite ahead of the propagation front. This scrapes off the surface of the combustion chamber, damaging engines in time.<sup>12</sup>

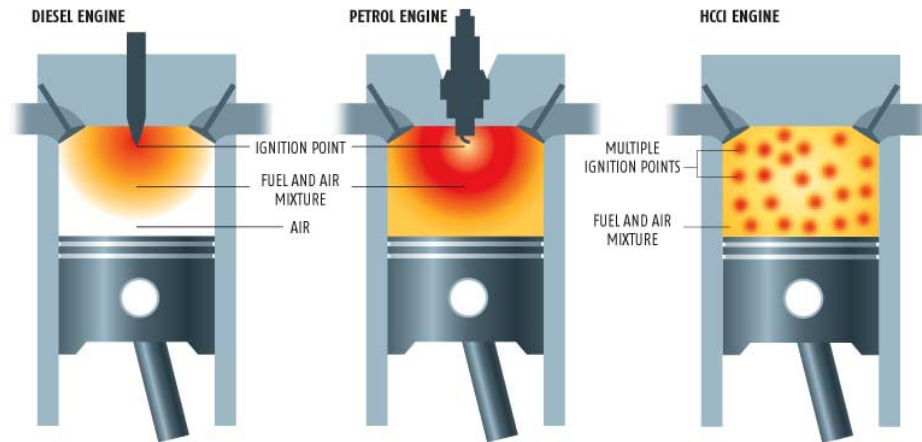


**Figure 1-3.** The juxtaposition of diesel, petrol engine and HCCI engine.<sup>13</sup>

On the other hand, diesel engines have higher compression ratio (18:1), which is contributing to their higher fuel efficiency. In addition to higher efficiency, carbon monoxide and unburnt hydrocarbon production is less in diesel engines.<sup>14-15</sup> Unfortunately,  $\text{NO}_x$ , PM, and soot emissions are still significant.<sup>16</sup> Homogenous charged compression ignition (HCCI) engines have high fuel efficiency as diesels, but with lower  $\text{NO}_x$  and PM emission.<sup>17</sup> In contrast to gasoline and diesel motors, there are multiple ignition points achieved by rise in pressure and temperature during compression.<sup>11</sup> Because the combustion is not initiated by an external source like a spark, in HCCI engines the timing of the reaction becomes a very important combustion characteristic. Therefore, knowledge of combustion mechanisms allows for accurate kinetic modeling of the engine reactions. With clear kinetic information, the right fuel mixtures can be designed to optimize combustion conditions in new generation engines.

## 1.5 An Overview of the Thesis

In this thesis, the mechanisms of two combustion systems are investigated: mesitylene and tert-amyl methyl ether (TAME). Mesitylene is proposed as a possible jet fuel.<sup>18</sup> Its combustion mechanism will be discussed in Chapter 4. Due to stringent mandates, oxygenated additives like ETBE and TAME are added to fuels to control the amount of oxygen in transportation combustibles to at least 2.7% by weight.<sup>19</sup> Although TAME itself is not generated from renewable sources, there is a general interest in producing methanol, one of the ingredients in making TAME, from biomass. Because renewable fuels are preferable, this ether is selected for investigation. Its reaction is elucidated in Chapter 5.

In order to study the combustion of these molecules, the reactions reported in this thesis are carried out using a multiplex energy-resolved photoionization mass spectrometer at the Advanced Light Source (ALS) located at Lawrence Berkeley National Laboratory (LNBL). Reactions are initiated in a slow-flow reactor by photolysis of radical precursors using an excimer laser. The reaction species are then probed by a multiplex time-of-flight mass spectrometer. The synchrotron radiation generated at the ALS is used to ionize molecules for detection. The ALS, excimer laser, and the experimental apparatus are discussed in Chapter 2. Photoionization spectra are the most vital data gathered from the mass spectrometer. The theory of photoionization, the principle governing the behavior of these curves, and computational methods predicting photoionization spectra are explained briefly in Chapter 3.

## 1.6 References

1. BP Statistical Review of World Energy June 2011; BP: London, 2011.
2. Koomey, J. G., Estimating total power consumption by servers in the US and the world. February: 2007.
3. *What is U.S. electricity generation by energy source?*; U.S. Energy Information Administration: 2014.
4. Westphal, G. A.; Krahl, J.; Brüning, T.; Hallier, E.; Bünger, J., Ether Oxygenate Additives in Gasoline Reduce Toxicity of Exhausts. *Toxicology* **2010**, *268*, 198-203.
5. Motor Vehicle-Related Air Toxics Study; EPA 420-R-93-005; U.S. Environmental Protection Agency, Office of Mobile Sources: Ann Arbor, MI, 1993.
6. Murakami, Y.; Oguchi, T.; Hashimoto, K.; Nosaka, Y., Density Functional Study of the High-Temperature Oxidation of o-, m- and p-Xylyl Radicals. *J. Phys. Chem. A* **2009**, *113*, 10652-10666.
7. Walsh, M. P., Vehicle Emissions and Health in Developing Countries. In *Air Pollution & Health in Rapidly Developing Countries*, McGranahan, G.; Murray, F., Eds. Earthscan Publications: Sterling, VA, 2003; pp 146-175.
8. Seagrave, J.; McDonald, J. D.; Gigliotti, A. P.; Nikula, K. J.; Seilkop, S. K.; Gurevich, M.; Mauderly, J. L., Mutagenicity and *In Vivo* Toxicity of Combined Particulate and Semivolatile Organic Fractions of Gasoline and Diesel Engine Emissions. *Toxicol. Sci.* **2002**, *70*, 212-226.
9. Seagrave, J.; Mauderly, J. L.; Seilkop, S. K., *In Vitro* Relative Toxicity Screening of Combined Particulate and Semivolatile Organic Fractions of Gasoline and Diesel Engine Emissions. *J. Toxicol. Env. Heal. A* **2003**, *66*, 1113-1132.
10. Nguyen, T. L.; Peeters, J.; Vereecken, L., Theoretical Reinvestigation of the O(3P) + C6H6 Reaction: Quantum Chemical and Statistical Rate Calculations. *J. Phys. Chem. A* **2007**, *111*, 3836.
11. Kobayashi, T.; Nagakura, S., Photoelectron spectra of substituted benzenes. *Bull. Chem. Soc. Jpn.* **1974**, *47*, 2563.
12. Zádor, J.; Taatjes, C. A.; Fernandes, R. X., Kinetics of elementary reactions in low-temperature autoignition chemistry. *Prog. Energ. Combust.* **2011**, *37*, 371-421.
13. Marshall, J., Clean-burn engine dodges ever tighter regulations. *New Sci.* **2006**, *189*, 26-27.

14. Palmer, M. H.; Moyes, W.; Speirs, M.; Ridyard, J. N. A., The electronic structure of substituted benzenes; ab initio calculations and photoelectron spectra for phenol, the methyl- and fluoro-derivatives, and the dihydroxybenzenes. *J. Mol. Struct.* **1979**, *52*, 293.
15. Wallington, T. J.; Potts, A. R.; Andino, J. M.; Siegl, W. O.; Zhang, Z.; Kurylo, M. J.; Huie, R. E., Kinetics of the Reaction of OH Radicals with T-Amyl Methyl Ether Revisited. *Int. J. Chem. Kinet.* **1993**, *25*, 265-272.
16. Smith, D. F.; McIver, C. D.; Kleindienst, T. E., Kinetics and Mechanism of the Atmospheric Oxidation of Tertiary Amyl Methyl Ether. *Int. J. Chem. Kinet.* **1995**, *27*, 453-472.
17. Zeng, W.; Xie, M., A novel approach to reduce hydrocarbon emissions from the HCCI engine. *Chem. Eng. J.* **2008**, *139*, 380-389.
18. Roubaud, A.; Minetti, R.; Sochet, L. R., Oxidation and combustion of low alkylbenzenes at high pressure: comparative reactivity and auto-ignition. *Combust. Flame* **2000**, *121*, 535-541.
19. *Public Health and Welfare. US Code. 7401-7671, Title 42, 1977.*



## **Chapter 2 - Experimental Set-up: The Multiplexed Chemical Kinetics Mass Spectrometer Coupled to the Advanced Light Source**

All experiments are conducted at the Advanced Light Source (ALS) located in the Lawrence Berkeley National Laboratory. A multiplex time- and energy-resolved mass spectrometer is employed to probe oxidation products during the combustion reaction of selected biofuel molecules. The synchrotron radiation generated at the ALS was used as the ionization source for the mass spectrometer. This chapter describes the main ALS components and the experimental apparatus at the Chemical Dynamics Beamline 9.0.2.3 endstation.

### **2.1 The Advanced Light Source**

When charged particles travel at relativistic velocities using a bent trajectory with a large curvature, synchrotron radiation is generated.<sup>1</sup> The ALS is a third generation synchrotron facility that generates high intensity X-ray beams through accelerating a beam of electrons.<sup>2</sup> Brightness is one of the reasons for which the light emitted at the ALS is chosen as the ionization source in the experiments described in this thesis. As can be seen in Figure 2-1, which compares the brilliance of different light sources available in the United States, the ALS is one of the brightest sources. The ALS light is at least  $10^6$  times brighter than a conventional x-ray tube and  $10^5$  times brighter than the Sun.

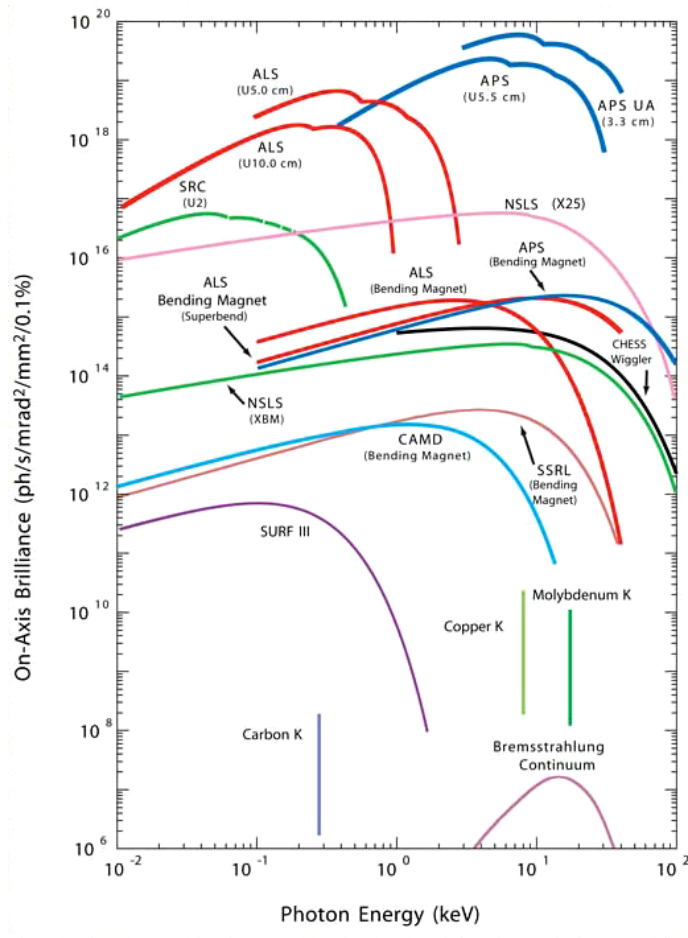


**Figure 2-1.** A chart comparing the brilliance of different X-ray light sources in the United States, provided by courtesy of the Advanced Photon Source at the Argonne National Laboratory.<sup>3</sup>

## 2.2 The ALS Components

Like other synchrotron radiation facilities, the ALS produces light by accelerating a beam of particles, electrons in this case, via a linear accelerator (Linac). Then, the beam is injected into the 1.9 GeV synchrotron booster ring and kept in the 200-meter-long storage ring. Beam introduction is accomplished by bending magnets. By bending the electron beam through applying an alternate magnetic field, undulators generate synchrotron radiation, which can be used at

different beamlines. Figure 2-2 is a general floor plan of the ALS, which includes some of the ALS component mentioned above. A brief description of each component will be given in the following sections.

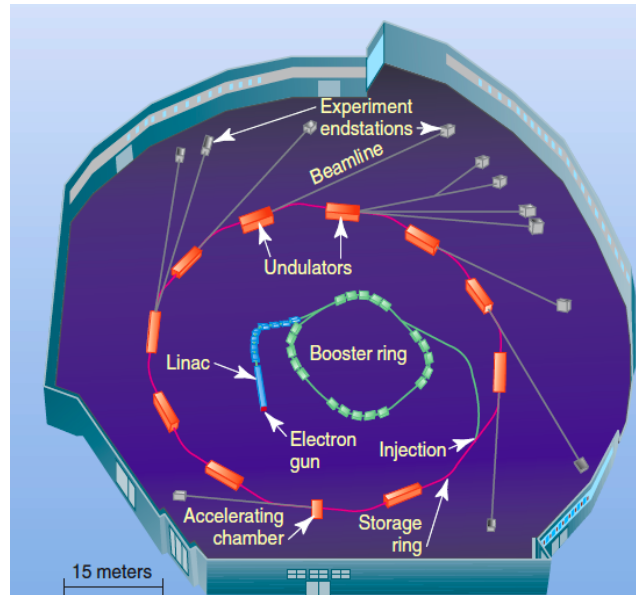


**Figure 2-2.** A general floor plan of the Advanced Light Source, provided by courtesy of the Advanced Light Source at the Lawrence Berkeley National Laboratory.<sup>4</sup>

### 2.2.1 Linear Accelerator

A linear accelerator (Linac) generates electrons and speeds them up to almost the speed of light. The Linac at the ALS is four-meter long and consists of an electron gun and a buncher (Figure 2-3). Electrons are produced at the cathode of the electron gun. There, they are emitted when about 1 cm<sup>3</sup> of barium aluminate is heated. When a material emits charged particles upon heating, the substance is said to be thermoionic.<sup>5</sup> These thermoionic emitted electrons are then attracted towards the gate because of a strong positive potential pulsed at a frequency of 500 MHz. Passing through the gate, the electrons are pulled towards the main anode.<sup>6</sup> The

electric field generated by the doughnut-shaped main anode guides electron into the buncher.

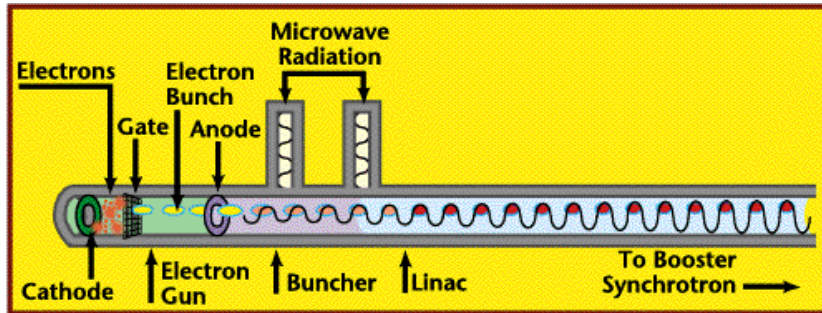


**Figure 2-3.** A schematic of the Linac describing how an electron beam is generated.<sup>7</sup>

The buncher of the Linac accelerates the electron beam by applying microwave radiation, which is generated by a klystron.<sup>8</sup> Gaining 60% of the speed of light, the electron beam enters the linear accelerator itself, which is an extension of the buncher. The linear accelerator speeds up the beam further to almost the speed of light by applying radio-frequency (RF) waves. Then, the 0.2 mm × 0.2 mm thin electron beam leaves the Linac and goes into the booster ring.

### 2.2.2 Booster Ring and Storage Ring

The electron beam travels around the circular booster ring and accelerates each time it revolves in the RF cavity, where an RF wave of 500 MHz further bunches the beam to 99.999996% of the speed of light. The beam makes 1,300,000 revolutions in less than one second and gains the energy of 1.5 MeV. The beam is then injected into the storage ring, which consists of 12 arc-shaped and 12 straight sections joined by undulators or wigglers forming a ring surrounding the booster ring. The beam can travel circularly through the storage ring because of undulators and wigglers.

### 2.2.3 Insertion Devices

Undulators and wigglers, located at each straight section of the storage ring, are insertion devices that alter the direction of the electron beam so that the beam can travel in an orbit inside the storage ring. Undulators and wigglers both comprise of arrays of magnets, which are oriented so that the poles are alternating.<sup>1</sup> This configuration creates an alternating magnetic field that oscillates or “wiggles” the electron beam trajectory several times, and synchrotron radiation is emitted along the travel direction.<sup>1</sup> The photon energy of the undulator is related to the reduced Planck constant ( $\hbar$ ), the speed of light ( $c$ ), the beam energy ( $\gamma$ ), the undulator period ( $\lambda_L$ ) or the spacing between the magnets, the wiggler strength parameter ( $K$ ) and the light emission direction ( $\theta_L$ ). The photon energy ( $\hbar\omega$ ) of the undulator can be expressed by the equation provided by Margaritondo as follows:<sup>9</sup>

$$\hbar\omega \cong \left( \frac{4\hbar\pi c\gamma^2}{\lambda_L} \right) \left( \frac{1}{1 + \frac{1}{2}K^2 + \theta_L^2\gamma^2} \right) \quad (2.1)$$

$\gamma$  can be expressed as:

$$\gamma = \frac{E}{m_0c^2} \quad (2.2)$$

where ( $E$ ) is the electron energy, and  $m_0$  is the rest mass of an electron, whereas  $K$  can be expressed as:

$$\kappa = \frac{eB_L\lambda_L}{2\pi cm_0} \quad (2.3)$$

where  $e$  is the electron charge, and  $B_L$  denotes the magnetic field strength. From the undulator equation, it can be concluded that the smaller the spacing between the magnets, the higher the energy that the undulator produces.

Figure 2-4 illustrates that, when an electron beam passes through the undulator magnets, its wave trajectory curves. Light is emitted tangentially from each crest of the curved trajectory, which sum up to form the synchrotron radiation. The undulators are 4.5 meter long and weigh about 20 Tons, but are built with extremely high precision of approximately  $50\ \mu\text{m}$  (high tolerance). Compared to undulators, wigglers have fewer magnetic poles and produce radiation with a broader spectrum. Also, if the parameter  $K$  in equation 2.3 is greater than 1, the insertion device is called wiggler. Undulators are used at the ALS to generate synchrotron radiation.

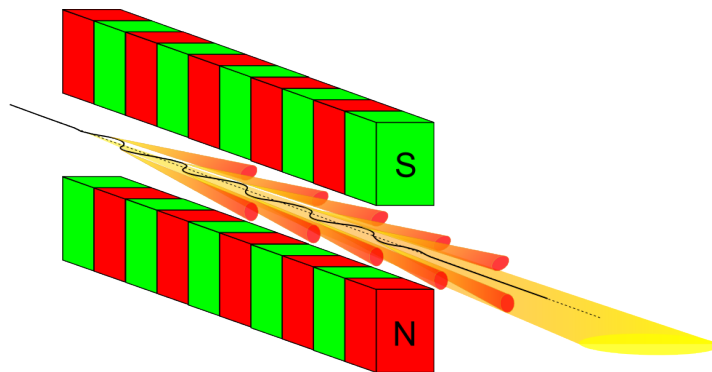


**Figure 2-4.** A diagram of an electron beam passing through the undulator magnets and generating synchrotron radiation, by courtesy of the Hamburger Synchrotronstrahlungslabor HASYLAB at the Deutsches Elektronen-Synchrotron DESY.<sup>10</sup>

#### 2.2.4 Gas Filter and Monochromator at Beamline 9.0.2

At each linear section of the storage ring, synchrotron radiation generated by the electron beam with the aid of undulators is directed into each beamline. The

energy range of the radiation that could be used at the Chemical Dynamics Beamline (9.0.2) is 7.4-24.6 eV. The synchrotron radiation passes through a gas filter, which is a windowless absorption cell filled with 30 Torr of either Ar or Kr gas. Higher harmonics radiation that is higher in energy than the ionization energies of the noble gases just mentioned (15.76 eV for Ar and 14.00 eV for Kr) are removed.

The bandwidth of the filtered radiation is then further narrowed by a 3-m off-plane Eagle monochromator to a 10-50 meV resolution.<sup>11</sup> A monochromator can narrow the bandwidth of the incoming radiation simply by reflecting the incoming radiation according to the Bragg's Law:

$$n\lambda = 2d\sin\theta \quad (2.4)$$

where  $n$  is an integer, and  $d$  is the distance between two parallel atomic layers of the monochromator lattice (reflecting plane). According to this law, when an incident beam hits the lattice at a certain incident angle ( $\theta$ ), which is the angle between the incident beam and the normal of the surface, only a certain wavelength ( $\lambda$ ) from the incident radiation can be reflected.<sup>12</sup> Hence, varying the angle between the normal of the monochromator surface and the incident synchrotron radiation allows the selection of wavelengths, and thus narrowing the bandwidth of the incoming radiation. The observed resolving power of the off-plane Eagle monochromator used at the Chemical Dynamics Beamline is demonstrated to be 70,000 with the photoionization efficiency of neon.<sup>13</sup> This monochromator can achieve narrower spectral bandwidth of 10-50 meV at the expense of photon flux.<sup>11</sup>

Finally, the light is directed into the ionization chamber of the experimental apparatus at the endstation 3.

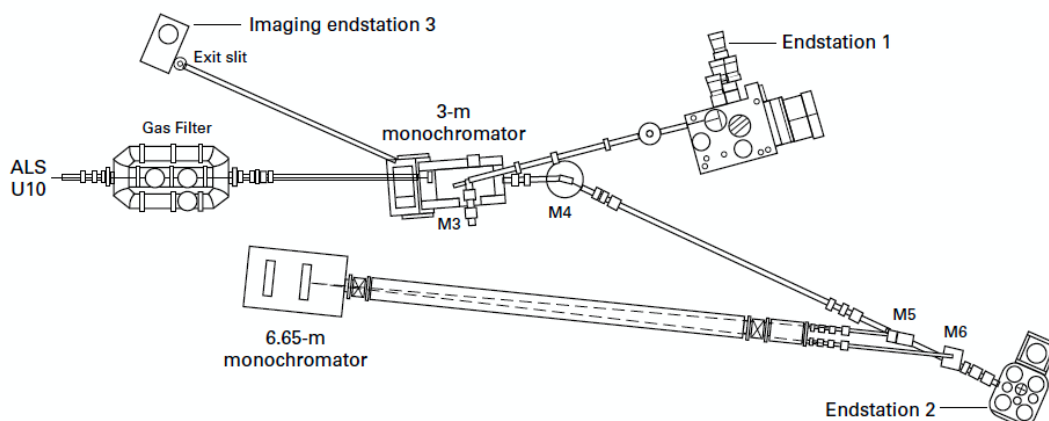


**Figure 2-5.** A schematic presenting the gas filter and the monochromators used at Beamline 9.0.2 (Chemical Dynamics) at the ALS.<sup>13</sup>

### 2.3 The Experimental Apparatus

The experimental apparatus consists of a slow-flow reaction cell, an excimer laser, an ionization chamber, a time-of-flight mass spectrometer (TOFMS), and a microchannel plates (MCP) ion detector. All regions of the instrument are kept under vacuum by vacuum pumps (See Figure 2-6).

All reactants (including biofuels, aerosol precursors, and radical precursors) are brought into the gas phase. When the vapor pressure of the reactants is low (like mesitylene), the species are put into glass bubblers placed in a thermo-stated bath. Helium is bubbled into the liquid chemicals, allowing an efficient transportation of their low vapor pressure. On the other hand, if the vapor pressure of the reactants is high (such as TAME, Cl<sub>2</sub>, and NO<sub>2</sub>), the chemical of interest is diluted to a concentration of about 1% with helium in a gas tank at a specified total pressure.



Chlorine gas and nitrogen dioxide, used as precursor of Cl and O(<sup>3</sup>P) radicals, respectively, are also diluted to about 1% with helium. All gaseous reactants are flowed into the reaction cell.

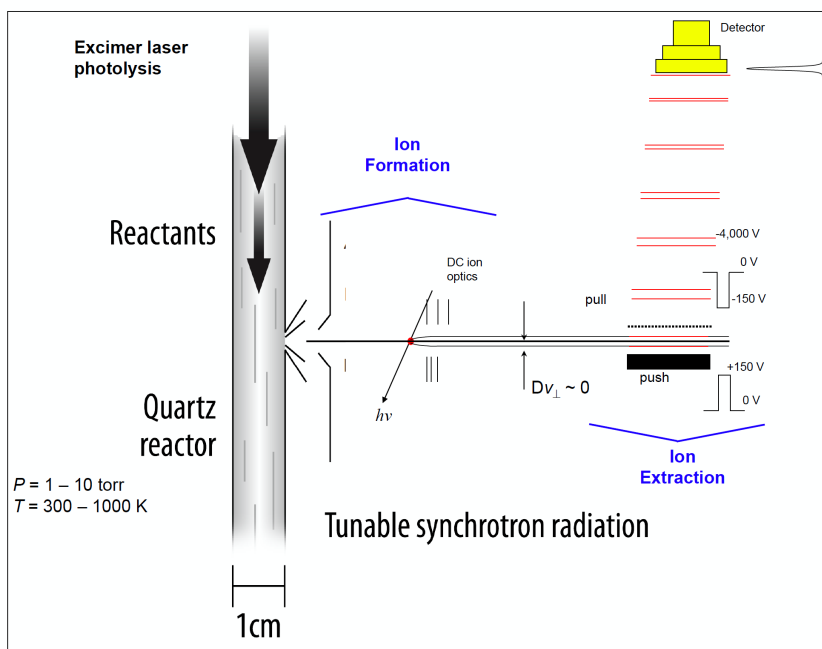


**Figure 2-6.** A simplified schematic of the multiplex chemical kinetics orthogonal mass spectrometer.<sup>14</sup>

2.3.1 Tracing the Molecules—From the Slow-Flow Reaction Cell to the MCP Ion Detector

All reactions take place in the slow-flow reaction cell, which is a 62 cm long quartz tube with an outer diameter of 1.27 cm and inner diameter of 1.05 cm.<sup>11</sup> Calibrated mass flow controllers (with flows ranging from 10 to 200 standard cubic centimeters per minute (SCCM)) meter reactant gases into the reaction cell. SCCM is a measurement of flow rates of gases, where “standard” denotes that the flow rate assumes standard temperature and pressure. The pressure in the reaction tube is

monitored via ion gauges in the range 1-10 Torr. Pressure control is achieved through gas removal using a closed-loop feedback throttle valve connected to a Roots pump. The pressure is monitored by a capacitive manometer. If a reaction is carried out at room temperature, the pressure inside the reaction cell is typically maintained at 4 Torr.

The temperature of the cell can be varied (300-1500 K) using resistive heating, and the outer surface of the cell is wrapped with an 18  $\mu\text{m}$  thick nichrome heating tape.<sup>11</sup> The tube is further insulated to assure thermal homogeneity by a layer of square-weave, yttria-stabilized zirconia cloth (ZYM-15, Zircar Zirconia, Inc.), which is wrapped by two-halves of a gold-plated copper sheath.<sup>11</sup>

A reaction is photolytically initiated by an excimer laser, which is used to photolyze the chosen precursors. For example  $\text{Cl}_2$  and  $\text{NO}_2$  are used to produce Cl and  $\text{O}(^3\text{P})$  radicals, respectively, at the appropriate wavelength (i.e., 248 nm for OH and 351 nm for Cl and O atoms).<sup>15-16</sup> The unfocused photolysis laser travels collinearly down the reaction tube and is pulsed at a repetition rate of 4 Hz. A more detailed description of the excimer laser is provided in the next section (2.3.2). After the reaction is initiated, the gas mixture containing reactants and products is sampled on the side of the tube through a 650 (most commonly used) or 400  $\mu\text{m}$  diameter pinhole. A  $3200 \text{ L s}^{-1}$  oil-free molecular pump evacuates gases in the source chamber.<sup>11</sup> The effusive beam is, then, skimmed by a skimmer with a 0.15 cm diameter, which is 0.2-0.3 cm downstream of the pinhole, and enters the ionization chamber. Here, all the species are crossed by the synchrotron radiation. If the photon energy is higher than a species ionization energy, the species will be

ionized. A  $1600 \text{ L s}^{-1}$  turbomolecular pump evacuates this region. The ions are then accelerated, focused, and collimated towards the detection region. This region is kept under high vacuum by a  $700 \text{ L s}^{-1}$  turbomolecular pump. All the mentioned turbomolecular pumps are backed by scroll pumps.<sup>11</sup>

### 2.3.2 The Excimer Laser

The photons from the excimer laser are used to photolyze precursors to produce radicals. Photons are emitted during the process of lasing because of inversion population, which describes a state when the population of an atom or a molecule at its excited state exceeds the population at its ground state.<sup>17</sup> When the excited molecule relaxes to its ground state, a photon with an energy equal to the gap between the excited state and the ground state is emitted. The gap is called the laser band as shown in Figure 2-7.

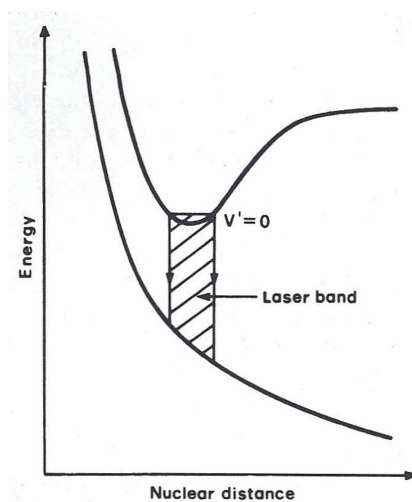


**Figure 2-7.** Potential energy diagram of the bound excited state and the unbound ground state. Lasing happens when the energy is released in the form of photons.<sup>18</sup>

To produce photons at 351 nm, a xenon fluoride (XeF) excimer laser is used. A XeF molecule does not exist naturally because XeF is unbound at its ground state but is bound at its excited state. Therefore, excited XeF molecules, or (XeF)\*, have to be generated so that (XeF)\* can relax to the unbound ground state and emit photons. Figure 2-8 is a schematic very similar to the excimer laser used in the experiments carried out for this thesis.

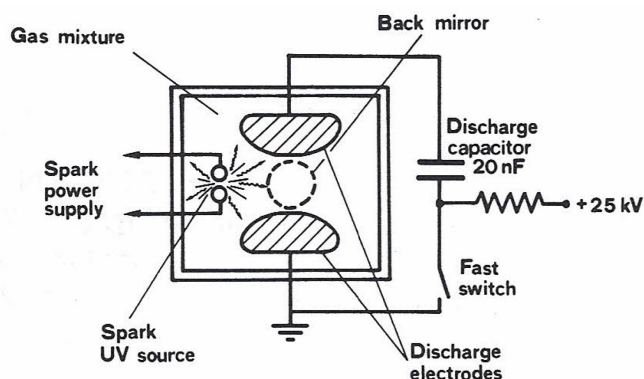


**Figure 2-8.** A schematic of a general excimer laser configuration.<sup>18</sup>

In the laser set-up, a mixture of Xe and F<sub>2</sub> gas is pumped into a gas chamber. An electrical discharge produces a spark, which ionizes Xe molecules forming Xe<sup>+</sup> ions and exciting Xe atoms (Xe\*). Since Xe\* atoms behave similarly to alkali atoms, the excited noble gas atoms collide and bond with fluorine molecules, forming excited XeF molecules, (XeF)\*, according to the following reaction:



Excited rare gas halide like (XeF)\* is properly known as “heterexcimer” or exiplex, but “excimer” is universally accepted, which actually describes a diatomic situation

(excited dimer). On the other hand, dissociation attachment reaction or the bombardment of electrons to fluorine molecules forms  $F^-$  ions



Through a three-body collision process,  $Xe^+$  and  $F^-$  recombine to conserve total momentum and energy

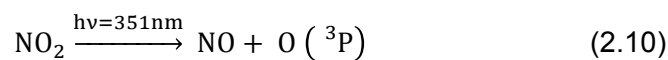


where M can be either He or Ne. The unstable and excited species  $(XeF)^*$  immediately relaxes to the ground state and dissociates back to Xe and F atoms, releasing energy in the form of photons, which are at a wavelength of 351 nm. This light is known as an excimer laser.<sup>19</sup>

Photons at 351 nm are used to produce Cl and  $O(^3P)$  radicals. To produce chlorine radicals,  $Cl_2$  gas molecules are photolyzed according to the following reaction.



The recommended quantum yield of this photolysis at 351 nm is 1.00 listed by the IUPAC Subcommittee for Gas Kinetic Data Evaluation.<sup>20</sup> Maric et al.<sup>21</sup> reported that the  $Cl_2$  absorption cross section at 351 nm is  $1.82 \times 10^{-19} \text{ cm}^2$ . On the other hand, ground state oxygen atoms,  $O(^3P)$ , are formed by photolysis of  $NO_2$  with a recommended quantum yield equal to unity (1.00) when the wavelength is below 398 nm,<sup>21</sup> while the absorption cross section is  $4.62 \times 10^{-19} \text{ cm}^2$  according to Vandaele and co-workers.<sup>22</sup>



193 nm photons can be produced using the same set-up replacing krypton with argon. The unfocused excimer laser used in these experiments has a fluence of 10–60 mJ cm<sup>-2</sup> and a pulsewidth of 20 ns. The excimer laser is usually fired at a repetition rate of 4 Hz.<sup>11</sup>

### 2.3.3 Vacuum Pumps

During the experiments, it is essential to keep the reaction cell, the source chamber, the ionization region, and the TOF detector free of contaminants. To achieve this, three types of vacuum pump systems are used, including Roots pumps, turbomolecular, and scroll pumps.

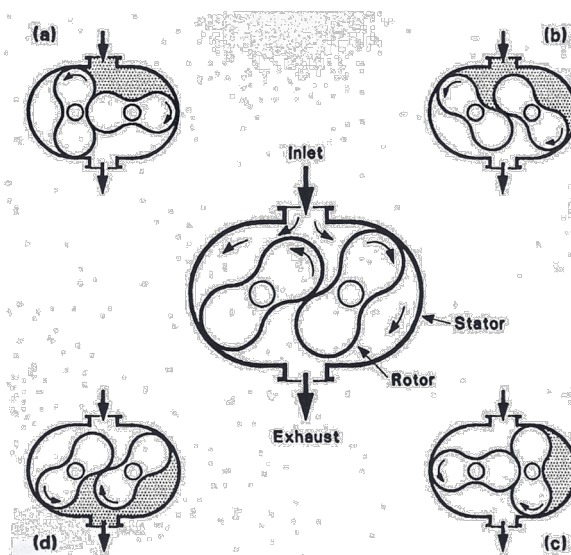


**Figure 2-9.** The diagram of the cross section of a Roots pump showing the operation cycle.<sup>23</sup>

A Roots pump evacuates the reaction tube and help controlling the pressure in it. Roots pump contains two figure-eight-shaped rotors secured on parallel shafts that revolve in synchronism but in reversed directions.<sup>24</sup> The rotors are just 0.05-0.25 mm apart and can rotate at a speed of 500-3500 rpm, depending on the size of the pump and final pressure ( $20-10^{-4}$  Torr).<sup>23-24</sup> The capacities available of the Roots pumps range from 75 to 30,000 m<sup>3</sup>/hr.<sup>23</sup>



**Figure 2-10.** A compound turbomolecular pump with the rotor shown.<sup>25</sup>

Turbomolecular pumps consist of a stationary stator and rotor blades, which are slotted at an angle to increase the gas molecules traveling from inlet to outlet rather than the opposite.<sup>23-24, 26</sup> This mechanical configuration transfers a momentum to the gas molecules by high speed spinning rotating blades.<sup>24</sup> The rotor can rotate at a maximum speed of 80,000 rpm that is equivalent to a velocity of  $500 \text{ m s}^{-1}$  when measured at a blade tip.<sup>24</sup> The lowest achievable pressure can be as low as  $10^{-9}$  Torr when turbomolecular pumps are used in tandem.<sup>27</sup> Turbomolecular pumps of three

different capacities are utilized in the experimental apparatus. A  $3200 \text{ L s}^{-1}$  pump evacuates the source chamber, whereas smaller turbomolecular pumps with capacities of  $1600$  and  $700 \text{ L s}^{-1}$  are used to evacuate the ionization chamber and the TOF detector, respectively.<sup>11</sup>

All turbomolecular pumps used here are backed by scroll pumps. Found in each scroll pump are two identical scrolls; one is stationary while the other is moving.<sup>23</sup> As seen in the arrangement of the spiral scrolls depicted in Figure 2-11b, there are pockets between the orbiting scroll and the fixed scroll. When the orbiting scroll moves, the pockets, along with gases housed in the pockets, are pushed, or compressed, towards the pump center. Gases escape from the exit port located at the pump center. The ultimate pressure of the oil-free scroll pumps is  $10^{-2}$  Torr, and the capacity ranges from  $15$  to  $40 \text{ m}^3 \text{ h}^{-1}$ .<sup>24</sup>

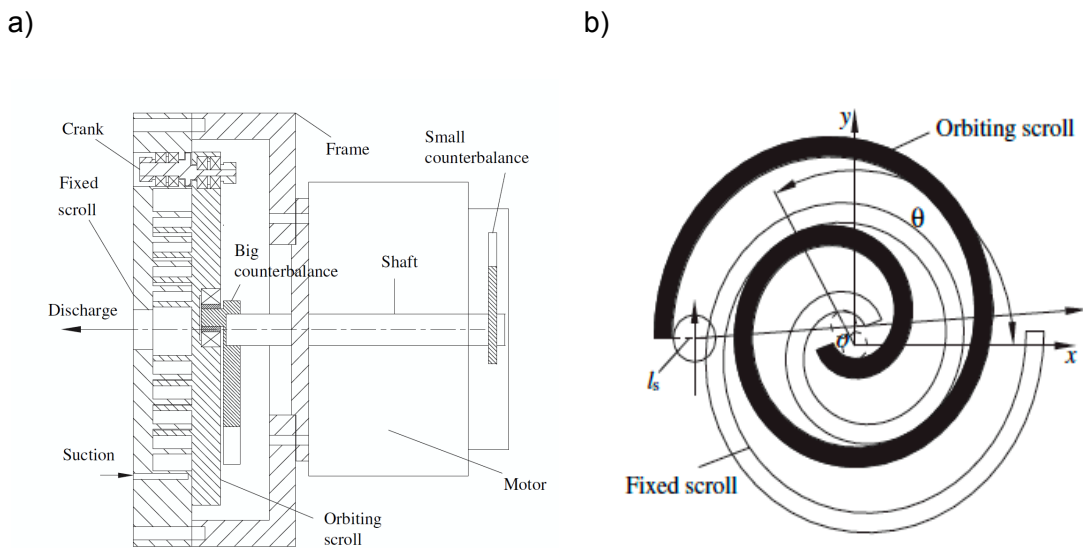


**Figure 2-11.** a) Vertical cross section of a scroll pump. The stationary and the movable scrolls are shown on the left. b) The horizontal cross section of the scroll showing their orientation.<sup>28</sup>



### 2.3.4 Time-of-flight Mass Spectrometer and Microchannel Plates

After crossing the synchrotron radiation generated by an undulator at the ALS, all molecules are ionized in the ionization chamber whenever the energy of the light is higher than their ionization energy. These cations are subject to a series of electric fields that focus and collimate the ionic species towards the end of the first part of the flight tube. At this point, a “pusher”, which is a positive electric field of  $\sim 150$  V, and a “puller”, a negative electric field of  $\sim -150$  V are used to change the initial ions direction by  $90^\circ$  to guide them towards the detector. Since all ions experience the same electric field (U), the initial kinetic energy gained is the same for all charged species, so their velocities are inversely proportional to the square root of the mass-to-charge ratios ( $m/z$ ).<sup>29</sup> Because a heavier molecule has a smaller velocity than a lighter molecule, mass separation can be achieved. The time (t) it takes to travel a distance (s) to reach the ion detector in the TOF analyzer depends on  $m/z$ .<sup>30</sup> This time is referred as TOF and is related to the travel distance of the molecule, the charge of an electron (e), the electric field, mass of the ion ( $m_i$ ) and the integer number of the charge (z) of the species.<sup>31</sup>

$$t = \frac{s}{\sqrt{2eU}} \sqrt{\frac{m_i}{z}} \quad (2.11)$$

From equation 2.11, the TOF, t, and the square root of  $m/z$  are linearly related. A plot of t against the square-root of  $m/z$  of known species (calibrants) can be obtained experimentally yielding a mass calibration curve

$$t = \alpha + \beta\sqrt{m/z} \quad (2.12)$$

where  $\alpha$  is the y-intercept, and  $\beta$  is the slope of the mass calibration curve.

The “destination” of all cations is the 44 mm Chevron style Microchannel plates (MCP) detector consisting of two individual MCPs stacked. MCP and the Chevron configuration will be discussed below. Individual MCPs are bundles of channel electron multiplier (CEM) tubes, which are made of semiconducting material. The task of the CEM tubes and MCPs in the mass spectrometer is to magnify the ion signal. Amplification is achieved because secondary electrons are generated when energetic ions impact on a semiconductor or metal surface.<sup>31</sup> The higher the velocity of the incoming ion and the lower the electron work function of the impacted surface, more secondary electrons are generated. As seen in Figure 2-13, when an incident ion beam hits the multiplier tube at an angle, a beam of electrons is generated. If a voltage is applied to the tube in a way that the side, opposite to the direction of the incident ion beam, becomes an electrode with a more positive charge, the electron beam is accelerated generating more secondary electrons, also known as cascade effect. Electron gain of a CEM tube is limited to  $10^4$ .<sup>31</sup>

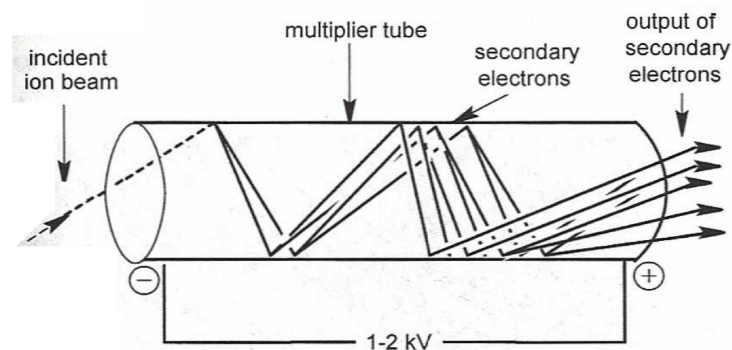


**Figure 2-13.** A schematic of the cross section of a channel electron multiplier tube showing the generation of secondary electrons.<sup>31</sup>

By joining many CEM tubes together, even more secondary electrons can be generated. Each MCP can achieve an electron gain of  $10^3$ - $10^4$ .<sup>31</sup> MCPs are built so

that each multiplier tube is tilted at a certain angle so that incident ion beam enters into the tube not collinearly to the tube but at an angle. This orientation allows the incident beam to collide with the surface of the tube so that secondary electrons are produced through the process described above. However, if the MCPs were not slanted at an angle, the incident ion beam would enter the CEM tube linearly, and the likelihood of the bombardment of the ion beam with the surface of the tube would be lessened. In this case, fewer secondary electrons would be produced, and hence, less amplification would be accomplished. In the Chevron configuration used in this experimental set-up, two MCPs are stacked together just like the the one in the middle of Figure 2-14 in that the axes of the two MCP line up to form V-shaped microchannels, facilitating even more secondary electrons than a single MCP. In this case the electron gain is  $10^6$ - $10^7$ .<sup>31</sup> If three MCPs are stacked together so that the axes of all MCPs form zig-zag-shaped microchannels (also known as z-stack), the electron gain increases up to  $10^8$ .<sup>31</sup>

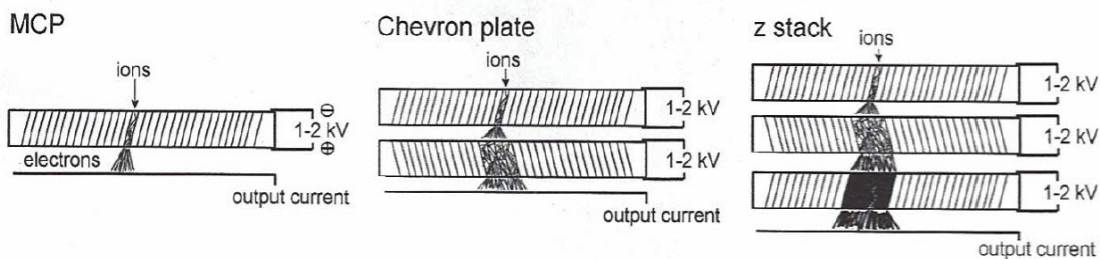


**Figure 2-14.** Single MCP, Chevron orientation MCPs, and z-stack configuration MCPs. Electron gain increases from left to right.

## 2.4 References

1. Margaritondo, G., Introduction to Synchrotron Radiation; Oxford University Press: New York, 1988.
2. ALS Quick Facts and New Tools: Make New Investigations Possible. <http://www-als.lbl.gov/index.php/about-the-als/quick-facts.html>.
3. Overview of the Aps. [http://www.aps.anl.gov/About/APS\\_Overview/index.html](http://www.aps.anl.gov/About/APS_Overview/index.html).
4. Probing the Liquid Water Surface Sci. Tech. Rev. [Online], 2001, p. 20-23. <http://www.llnl.gov/str/November01/Tobin.html>.
5. Brodie, I.; Jenkins, R. O., The Nature of the Emitting Surface of Barium Dispenser Cathodes. British Journal of Applied Physics **1957**, 8, 27.
6. Wiedemann, H., Particle Accelerator Physics Basic Principles and Lear Beam Dynamics; Springer-Verlag: New York, 1993.
7. The Advanced Light Source-a Tool for Solving the Mysteries of Materials. <http://www.lbl.gov/MicroWorlds/ALSTool/>.
8. Sessler, A. M.; Yu, S. S., Relativistic Klystron Two-Beam Accelerator. Physical Review Letters **1987**, 58, 2439.
9. Margaritondo, G., A Primer in Synchrotron Radiation: Everything You Wanted to Know About Sex (Synchrotron Emission of X-Rays) but Were Afraid to Ask. Journal of Synchrotron Radiation **1995**, 2, 148-154.
10. Storage Rings as Synchrotron Radiation Sources. [http://hasylab.desy.de/science/studentsteaching/primers/storage\\_rings\\_beamlines/index\\_eng.html](http://hasylab.desy.de/science/studentsteaching/primers/storage_rings_beamlines/index_eng.html).
11. Osborn, D. L., et al., The Multiplexed Chemical Kinetic Photoionization Mass Spectrometer: A New Approach to Isomer-Resolved Chemical Kinetics. Rev. Sci. Instrum. **2008**, 79, 104103.
12. Palmer, C.; Loewen, E., Diffraction Grating Handbook. 6th ed.; Newport Corporation: New York, 2004. <http://gratings.newport.com/information/handbook/handbook.asp>.

13. Heimann, P. A., et al., Performance of the Vacuum Ultraviolet High-Resolution and High-Flux Beamline for Chemical Dynamics Studies at the Advanced Light Source. **1997**, 68, 1945-1951.
14. Ray, A. Characterization of Ethene + OH Products and Cyclohexene Ring-Opening Mechanism Elucidation Via Synchrotron Photoionization Mass Spectrometry. University of San Francisco, San Francisco, 2010.
15. Welz, O., et al., Low-Temperature Combustion Chemistry of Biofuels: Pathways in the Initial Low-Temperature (550 K-750 K) Oxidation Chemistry of Isopentanol. *Physical Chemistry Chemical Physics* **2012**, 14.
16. Taatjes, C. A., et al., Products of the Benzene + O(3p) Reaction†. *J. Phys. Chem. A* **2010**, 114, 3355-3370.
17. Khanin, Y. I., *Fundamentals of Laser Dynamics*; Cambridge International Science Publishing: Cambridge, 2006.
18. Svelto, O.; Hanna, D. C., *Principles of Lasers*; 3rd ed.; Plenum Press: New York, 1989.
19. David N. Whiteman, W. F. M., Nita W. Walsh, and Keith D. Evans, Temperature Sensitivity of an Atmospheric Raman Lidar System Based on a Xef Excimer Laser. *Opt. Lett.* **1993**, 18, 247-249.
20. Iupac Subcommittee on Gas Kinetic Data Evaluation – Data Sheet Pcl11. <http://iupac.pole-ether.fr/>.
21. Troe, J., Are Primary Quantum Yields of No<sub>2</sub> Photolysis at  $\lambda \leq 398$  Nm Smaller Than Unity? *Z. Phys. Chem.* **2000**, 214, 573-581.
22. Vandaele, A. C.; Hermans, C.; Simon, P. C.; Carleer, M.; Colin, R.; Fally, S.; Mérienne, M. F.; Jenouvrier, A.; Coquart, B., Measurements of the NO<sub>2</sub> Absorption Cross-Section from 42000 cm<sup>-1</sup> to 10000 cm<sup>-1</sup> (238-1000 nm) at 220 K and 294 K. *J. Quant. Spectrosc. Ra.* **1998**, 59, 171-184.
23. Lafferty, J. M., *Foundations of Vacuum Science and Technology*. Wiley: New York, 1998.
24. O'Hanlon, J. F., *A User's Guide to Vacuum Technology*; 3rd ed.; Wiley-Interscience: Hoboken, 2003.
25. Roth, A., *Vacuum Techology*; North-Holland: New York, 1976.

26. Enosawa, H.; Urano, C.; Kawashima, T.; Yamamoto, M., High Throughput Tandem Turbomolecular Pump for Extreme High Vacuum; AVS: 1990; Vol. 8, p 2768-2771.
27. Hablanian, M. H., Engineering Aspects of Turbomolecular Pump Design. Vacuum **2007**, 82, 61-65.
28. Li, Z.; Li, L.; Zhao, Y.; Bu, G.; Shu, P., Theoretical and Experimental Study of Dry Scroll Vacuum Pump. Vacuum **2009**, 84, 415-421.
29. Smith, R. M., Understanding Mass Spectra: A Basic Approach; Wiley: Hoboken, 2004.
30. Herbert, C. G.; Johnstone, R. A. W., Mass Spectrometry Basics; CRC Press: New York, 2003.
31. Gross, J. H., Mass Spectrometry: A Textbook; Springer: Berlin, 2004.

## **Chapter 3 - Data Analysis, Photoionization Theories, and Ab Initio Computational Methods**

After describing how data of the biofuel or aerosol precursor oxidation are collected, it is worthwhile discussing the data analysis. Time profile plots, which are graphs of reaction time against ion signal of a specific species, and the photoionization spectra, which are plots of the synchrotron photon energy versus the ion signal, are very important experimental graphs that are employed for identifying oxidation products and intermediates. The procedures for acquiring these plots are outlined in Section 3.1. Sections 3.2-3.5 describe the ab initio methods that are crucial in the data analysis interpretation, especially when literature values are not available for the systems investigated.

### **3.1 Data Cycles and Data Processing**

Each data cycle initiates 20 ms before each photolysis laser shot is fired, and the total reaction time is 150 ms. When the laser is fired, it initiates the oxidation by photolyzing radical precursors, as explained in Chapter 2. At a particular photon energy ( $E$ ), the reaction time ( $t$ ), mass-to-charge ratio ( $m/z$ ), and ion signal ( $S$ ) are recorded and co-added successively in order to improve signal-to-noise ratio.<sup>1</sup> There are typically 150 - 250 laser shots per photon energy (step). The photon energy is increased in increments of 25 meV, and the data collection is repeated at each photon energy. The total number of laser shots depends on the energy range that is investigated.

Using the in-house procedure written for IGOR Pro 6 developed by WaveMetrics,<sup>2</sup> background subtraction by the pre-laser-pulse ion signal is applied to remove time-independent signal. The ion signal is then normalized by the ALS photocurrent measured by a calibrated vacuum ultra-violet (VUV) sensitive photodiode to account for the variation in photon flux of the ALS light. To analyze the data,  $S$  is plotted against three variables,  $E$ ,  $t$ , and  $m/z$  to form a 3D data block as illustrated in Figure 3-1.

The 3D data block  $S(m/z, t, E)$  is difficult to visualize because there are three variables; therefore, it is necessary to simplify the data by integrating the ion signal over one variable ( $m/z$ ,  $t$  or  $E$ ) to yield a 2D image. This 2D image, with two variables, still needs to be simplified by plotting the ion signal over a selected range of one variables, keeping the other one fixed. For example, on the top right hand corner of the 3D data cube of Figure 3-1 the 2D image is acquired after integrating the ion signal over the entire photon energy range. This image is a plot of ion signal versus  $m/z$  ( $x$ -axis) and reaction time ( $y$ -axis), or  $S(m/z, t)$ . This time-resolved mass spectrum provides useful information of chemical species whose signals are time-dependent. This  $S(m/z, t)$  plot can be further reduced by plotting the ion signal of a selected  $m/z$  versus reaction time. This 1D graph yields a kinetic trace of the selected  $m/z$ . If a molecule is a reactant, its time profile will show a depletion pattern, consistent with the consumption (reaction) of the species. On the other hand, if a molecule is generated from the oxidation reaction, its time profile will show a formation pattern. The chemical nature of the molecule can also be roughly deduced from the time profile. Non-radical species will show a stable time trace, whereas the time trace of radical products will rise sharply and deplete rapidly. The difference



between the shapes of the time trace is due to the higher reactivity of radicals compared to non-radical species.

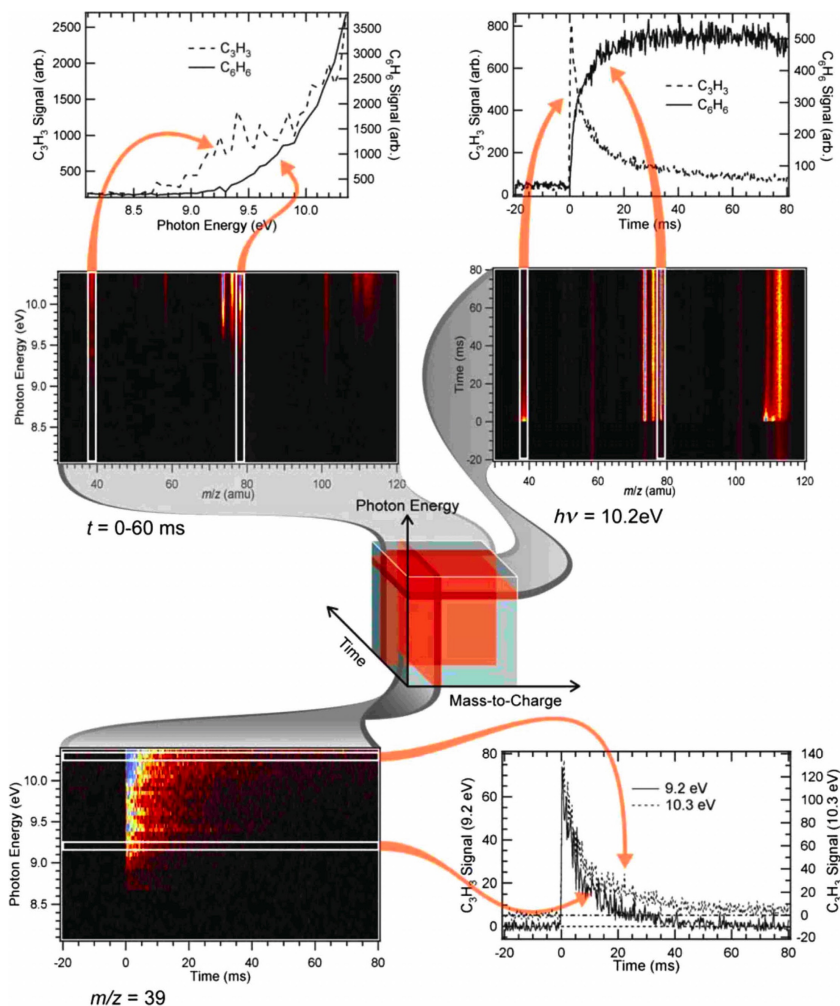


**Figure 3-1.** A pictorial representation of the 3D-data block with grey trails leading to three orthogonal 2D images. The red arrows point to 1D-plots extracted from the 2D images.<sup>1</sup>

In the same manner, when the ion signal is integrated over a specific time interval, such as 0-70 ms, a 2D plot of ion signal versus photon energy (y-axis) and  $m/z$  (x-axis), like the one on the top left corner of the 3D data cube in Figure 3-1, is generated. This  $S(m/z, E)$  2D image can then be reduced by plotting a specified  $m/z$

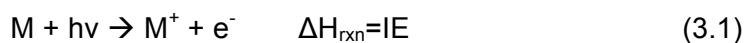
signal versus photon energy. This plot is called a photoionization spectrum. The energy at the onset of this spectrum is the observed ionization energy (IE). Since the IE and the photoionization spectrum shape of each molecule is unique, experimental spectra of a particular  $m/z$  can serve as powerful tool to identify chemical species. When the photoionization curve of a non-identified molecule is known, the literature spectrum can be superimposed onto the experimental data to compare the shapes of the two spectra. A match strongly suggests that the identified molecule is present in the reaction. In other words, photoionization spectra can be used as fingerprints in species identification. During data analysis, if the photoionization spectrum is not known, a Franck-Condon (FC) simulation can be performed. Alternatively, if the species is commercially available, it will be purchased, and its photoionization spectrum will be recorded. The theory behind the specificity of the spectral shape to each molecule and the simulation process will be explained in Sections 3.4 and 3.6, respectively.

### **3.2 Photoionization**

Conventional mass spectrometric methods use electron bombardment with an energy of 70 eV.<sup>3</sup> This process not only ionizes molecules, but the energy is sufficient to fragment them by breaking bonds. Therefore, when electrons are used as ionizing source, the mass spectrum shows multiple species, making the interpretation more difficult. The synchrotron radiation generated at the ALS is chosen as ionization source because the radiation utilized at the Chemical Dynamics endstation (described in Chapter 2) is tunable, with an energy range of 7.4-24.6 eV.

In addition, the energy resolution of 0.025 eV allows for accurate observation of the ionization threshold.

Photoionization processes can be represented as follow:



The minimum energy required to remove the first electron from an atom or molecule is the ionization energy. During photoionization, electrons are usually removed more easily from lone pairs orbitals than from  $\sigma$ - or  $\pi$ -bonds.<sup>3</sup> An atom or a molecule absorbs photon energy,  $h\nu$ , in a continuous fashion because any excess energy is transferred onto the electron in the form of kinetic energy ( $k^2$ ).<sup>4</sup>

$$h\nu = (V_i + k^2)e \quad (3.2)$$

where  $V_i$  denotes the ionization potential of the atom or molecule.

### 3.3 Vertical transitions, Frank-Condon Principle and Frank-Condon Factor

The principles of photoionization are discussed in more detail in this section. Figure 3-2 depicts different transitions in the photoionization process. There are three transitions: vertical, adiabatic, and dissociation. When a molecule is excited by a photon, it undergoes vertical transitions to its cationic states based on the Born-Oppenheimer approximation and the Frank-Condon principle, which will be explained in this section. When the cationic molecule is in an excited vibronic state, it undergoes non-radiative decay and relaxes to the ground vibronic state. The adiabatic transition is defined as the electronic transition from the neutral vibronic ground state to the vibronic ground state of the cation. The energy difference of

these two states is the adiabatic ionization energy (AIE). AIE of the suspect product can be calculated (calculations will be discussed in Section 3.6) and compared to the observed value. The match of the observed IE with the calculated AIE suggests the identification of the species. However, when molecules receive enough energy (i.e., AIE plus the cation dissociation energy  $D^\circ$ ), the molecule dissociatively ionizes, i.e., its cation fragments.

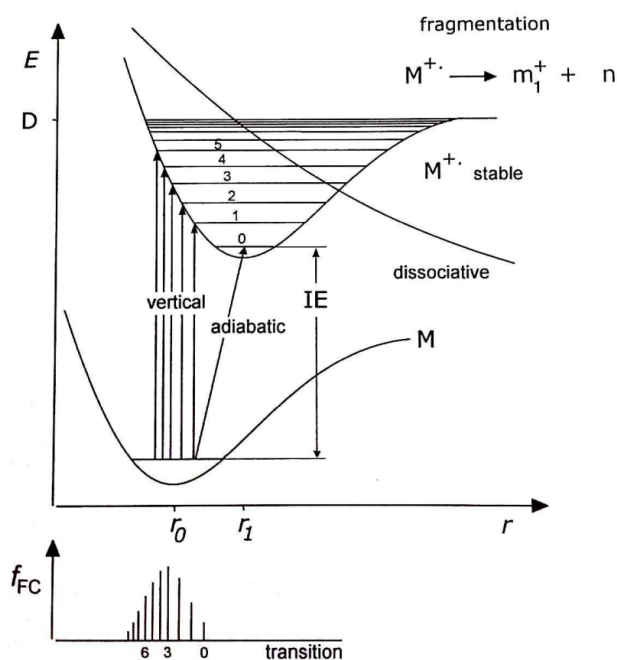


**Figure 3-2.** A diagram of two electronic potential energy curves for the neutral and cationic states. The vertical lines represent  $n' \leftarrow 0$  vibronic transitions.  $D$  is the dissociation energy of the cation, above which fragmentation occurs. A schematic of the Franck-Condon Factor ( $f_{FC}$ ) distribution is shown below the potential energy curves.<sup>3</sup>

As it is mentioned above, even in the ALS energy range in which the current experiments are carried out, dissociative ionization (formation of fragments upon photoionization) is observed, but at a lesser degree than conventional MS methods. The appearance energy of a specific fragment (AE) is simply the energy at which it

appears, and it can be calculated as the sum of AIE of the molecule and the cation dissociation energy (D) in the event that no dissociation barrier is present.

Electron transitions can be explained using the Born-Oppenheimer approximation and the Frank-Condon principle. The thermal velocity (a few  $100 \text{ ms}^{-1}$  at room temperature) of a molecule is insignificant compared to the velocity of an electron. Therefore, nuclei are considered to be stationary compared to the electron's motion. The Born-Oppenheimer approximation states that electronic and nuclear motions can be separated, and consequently, the positions of the atoms of the ionized molecule and the bond lengths do not change when the molecule is ionized.<sup>5-6</sup>

Electronic transitions can also be explained by the Franck-Condon principle. According to this principle, the highest probability of an electronic transition is achieved when the electronic wave functions of the initial and final states are at their maxima.<sup>7-8</sup> The  $E'_0 \leftarrow E''_0$  transition from the initial electronic state to the target state A in Figure 3-3 is a good example of this kind of transition. This yields a large Franck-Condon factor represented with the longest horizontal blue line just right to  $E''_0$  in Figure 3-3. A different result is obtained for the  $E'_1 \leftarrow E''_0$  transition where the electronic wave functions of the corresponding states of both the neutral and ionic molecule have an extremely small overlap. In this case, no vibrational peak is expected. In general, a large difference between the structures of the two states involved in a vibronic transition results in poor overlap of the corresponding wavefunctions.

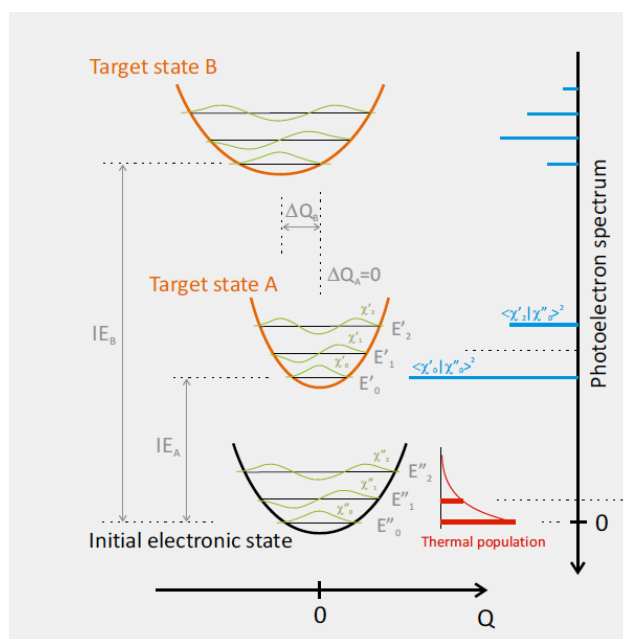


**Figure 3-3.** The black curve represents the potential energy surface of a neutral molecule, while the orange curves represent two different electronic states. These two target states have different overlaps with the neutral molecule, resulting in different Franck-Condon factors (blue sticks).<sup>9</sup>

The probability of a specific vertical transition from the vibrational ground state of the neutral molecule to a certain vibrational level of the ion is proportional to its Frank-Condon factor ( $f_{FC}$ ). The square of the matrix ( $M$ ), which expresses the overlap integrals between the vibrational wavefunctions of the neutral and cationic state is the Frank-Condon factor.<sup>10</sup>

$$M = \int \psi_{gm}^*(r) \psi_{xn}(r) dr \quad (3.3)$$

where  $\psi_{gm}$  is the  $m^{\text{th}}$  vibrational wavefunction of the neutral molecule and  $\psi_{xn}$  is the  $n^{\text{th}}$  vibrational wave function of the cationic molecule.  $r$  is the coordinate motion of the potential energy surface. The intensity is the highest when the overlap of the two wavefunctions is large, i.e., the molecular rearrangement is minimal upon

photodetachment, meaning the bond distances and angles do not change during the electronic transition.

### 3.4 Photoionization Spectra and Photoionization Cross-Section

As mentioned in Section 3.1, a plot of ion intensity versus photon energy is called the photoionization spectrum. The Frank-Condon principle in Section 3.3 correlates the ion intensity in a photoionization curve with the  $f_{FC}$ , i.e., the better the overlap of the neutral and cationic ground vibronic states, the higher the intensity of the first electronic transition and the steeper the onset slope of the photoionization spectrum. Because different molecules have different ionization energies and overlap between their neutral and cationic states, the onset and the shape of the photoionization spectrum is unique to each molecule. Therefore, the photoionization signal of a particular mass can be confidently assigned based on the spectral shape agreement and mass-to-charge ratio.

The ion signal ( $S_{(E)}$ ) at a specified photon energy  $E$  is related to the photoionization cross-section ( $\sigma_{(E)}$ ) according to the following relationship:

$$S_{(E)} = k\sigma_{(E)}\delta C \quad (3.4)$$

where  $k$  is the instrumentation constant,  $\delta$  the mass-dependent response, which is in our experiment approximately equal to the mass ( $m$ ) to the power of 0.67, and the concentration ( $C$ ) of the molecule. Photoionization cross-section can be explained as the effective area over which radiation ionizes a gaseous atom or molecule.<sup>11</sup> The cross-section is measured in Mb (megabarn) or  $10^{-18}$   $\text{cm}^2$ .<sup>4</sup> The relationship in equation 3.4 correlates the ion signal to concentration. Cool and co-workers<sup>12</sup>

calibrate the ion signal in the photoionization spectrum against a species with known photoionization cross-section and concentration, like propene. To convert the ion signal of a product ( $S_P$ ) to its photoionization cross-section ( $\sigma_T$ ), this thesis uses the following equation adopted from Cool et al.<sup>12</sup> and Welz et al.:<sup>13</sup>

$$\sigma_{T(E)} = \frac{\sigma_{R(E)} S_{P(E)} m_R^{0.67} C_R}{S_{R(E)} m_P^{0.67} C_P} \quad (3.5)$$

where  $C_R$  and  $C_P$  are the concentration of the calibrant and the product, respectively,  $m_R$  and  $m_P$  are the masses of the calibrant and the product, respectively,  $S_R$  is the calibrant reference signal, and  $\sigma_R$  the calibrant photoionization cross-section. All signals and photoionization cross-sections must be measured at the same photon energy ( $E$ ). If the calibrant is replaced with the reactant, equation 3.5 provides new information regarding the concentration of the product ( $C_P$ ) relative to that of the reactant ( $C_R$ ). The ratio of  $C_P/C_R$ , obtained by rearranging equation 3.5, is called the branching fraction. If all the branching fractions of the products are known, quantitative information about the reaction can be deduced. A more detailed explanation of the branching ratio calculation is included in Chapter 4.

When more than one structural isomer is present in a photoionization spectrum, the total cross section can be related to the cross-sections of individual isomers according to the following equations adopted from Cool and colleagues:<sup>14</sup>

$$\sigma_T = \sum_{i=1}^n \chi_i \sigma_i \quad (3.6)$$

$$\sum_{i=1}^n \chi_i = 1 \quad (3.7)$$



where  $\chi_i$  and  $\sigma_i$  are the mole fraction and photoionization cross-section of the  $i^{\text{th}}$  isomers, respectively. This ability to differentiate structural isomers makes the experimental setup an even more powerful tool in studying oxidations of biofuel or aerosol precursor molecules, because many oxidation products often have the same mass.

### 3.5 Electronic Structure Calculations

One can predict the ionization energy of products and simulate their photoionization spectra, using the computational method CBS-QB3, which enables the prediction of adiabatic ionization energy values by carrying out ab initio and density functional calculations. This section aims to outline the principle behind these theoretical methods.

The key equation in all electronic structure computations is the time-independent Schrödinger equation<sup>15</sup>

$$\hat{H}\psi = E\psi \quad (3.8)$$

where  $\hat{H}$  is the Hamiltonian operator, which comprises the kinetic and the potential energy operators,  $\psi$  is the multi-electron wave function describing the specific system, and  $E$  is the total electronic energy.

Electronic structure calculations when done using experimental data are called semi-empirical. Contrarily, calculations without the use of experimental data, but relying only on quantum mechanical means, are called ab initio (a loan word from Latin meaning “from the beginning”).<sup>16</sup> Another type of electronic structural calculations method used in this research is density-functional theory (DFT), which is

not as time consuming as ab initio methods and provides reliable molecular parameters.

### 3.5.1 Density Functional Theory

Density-functional theory uses the Hohenberg-Kohn theorem<sup>17</sup> to calculate properties of a molecule, such the ground state molecular energy and wave function. The theorem states that the energy and all other properties of a molecule at its ground state are related to ground-state electron probability density,  $\rho_0(x, y, z)$ . Later, Kohn and Sham<sup>18</sup> (KS) developed a DFT method that uses a fictitious non-interacting reference system to calculate the density-functional “exchange-correlation” energy ( $E_{XC}$ ). The total energy ( $E_{Total}$ ) can be expressed at the KS level of theory as follows:<sup>19</sup>

$$E_{Total} = T_0 + \int \rho V_{nuc} d^3r + \frac{1}{2} \iint \frac{\rho(r_1)\rho(r_2)}{r_{12}} d^3r_1 d^3r_2 + E_{XC} \quad (3.9)$$

where  $T_0$  is the kinetic energy of the non-interacting reference system. The second and third terms represents the nuclear interacting energy and the classical Columbic self-energy, respectively. Because  $E_{XC}$  is not known, it limits the accuracy of the DFT method.

### 3.5.2 B3LYP Method and Basis Sets

B3LYP<sup>19-20</sup> is a specific DFT method used in the CBS-QB3 composite model. This level of theory uses Becke 3-parameter functional with the Lee, Yang and Parr correlation functional. 6-311+G\*\* is an all-electron triplet-zeta valence basis set used for the B3LYP calculations. A basis set is a set of wave functions that describes the

best possible orbitals. In the case of 6-311+G\*\*, it includes a set of Gaussian basic functions, or Gaussian type orbitals (GTO). GTO can be expressed in terms of Cartesian coordinates as follows:

$$\chi_{\zeta,l_x,l_y,l_z}(x,y,z) = N x^{l_x} y^{l_y} z^{l_z} e^{-\zeta r^2} \quad (3.10)$$

N is a normalization constant. x, y, and z are Cartesian coordinates. The sum of  $l_x$ ,  $l_y$ , and  $l_z$  determines the type of orbital. If  $l_x$ ,  $l_y$ , and  $l_z$  sums up to 1, the orbital is p-type. Therefore, depending on the sum of the  $l_x$ ,  $l_y$ , and  $l_z$ , GTO can describe s, p, d, f, etc. orbitals. “6” signifies that six contracted primitive Gaussian type orbitals ( $\chi$ (PGTO)) are employed to estimated the core atom orbitals (AO), while “3” indicates that the inner valence AOs are expressed with three contracted PGTO ( $\chi$ (CGTO)), which can be represented as follows:<sup>16</sup>

$$\chi(\text{CGTO}) = \sum_i^k a_i \chi_i(\text{PGTO}) \quad (3.11)$$

where a refers to a contraction coefficient, while k represents the degree of contraction. Moreover, “1” represents that only one Gaussian function is used for outer valence component, and “+” denotes a set of diffuse s- and p-functions on heavy atoms to account for the significant electron density at large distances from the nuclei of anions, compounds with lone pairs, and hydrogen-bonded dimers. Finally, “\*\*” corresponds to a set of polarization functions that are of d and p types.<sup>16</sup> Polarization is achieved by mixing one orbital with another orbital to bend the shape of the first orbital to account for the uneven orbital shape of, say, hydrogen.

### 3.5.3 Coupled-Cluster Methods

Kohn and Sham (KS) theory postulates that electrons do not interact with each other. Even though the distance between the electrons and the nucleus is taken into consideration, the calculation using KS theory is limited because of the negligence of electron correlation. To correct for this deficiency, perturbational methods can be used. An example of such methods is Møller-Plesset (MP) perturbation theory.<sup>21</sup> MP expresses the  $\hat{H}$  as the sum of an unperturbed Hamiltonian  $\hat{H}^0$ , which operates on Hartree-Fock (HF) wave functions for the electrons in the molecule, and a perturbation  $\hat{H}'$ . The coupled-cluster (CC) methods further corrects for the electron correlation by applying Slater determinants, or antisymmetric wave functions that can be excited, to infinite order. Slater determinants are excited by replacing occupied molecular orbitals with virtual unoccupied orbitals. They can be singly, doubly, triply, quadruply, and so on excited, so these determinants can be referred as Singles (S), Doubles (D), Triples (T), Quadruples (Q), etc. The correction is done as follow:

$$\Psi_{cc} = e^{\mathbf{T}}\Phi_0 \quad (3.12)$$

where the CC wave function ( $\Psi_{cc}$ ) is the exact ground-state molecular electronic wave function, and  $\Phi_0$  is a normalized Hartree-Fock wave function.  $e^{\mathbf{T}}$  can be represented as

$$e^{\mathbf{T}} = 1 + \mathbf{T} + \frac{1}{2}\mathbf{T}^2 + \frac{1}{6}\mathbf{T}^3 + \dots = \sum_{k=0}^{\infty} \frac{1}{k!}\mathbf{T}^k \quad (3.13)$$

where  $\mathbf{T}$  represents an operator that can be written as

$$\mathbf{T} = \mathbf{T}_1 + \mathbf{T}_2 + \mathbf{T}_3 + \cdots + \mathbf{T}_N \quad (3.14)$$

The operators  $\mathbf{T}_1$ ,  $\mathbf{T}_2$ , are excitation operators that can promote one, two, ..., respectively, electrons into virtual spin orbitals. As mentioned above,  $\Psi_{cc}$  is the exact electronic wave function; therefore, inclusion of all  $\mathbf{T}$  operators provides the exact solution. Unfortunately, including all  $\mathbf{T}$  operators only applies to smaller systems. To make the calculation applicable to larger systems and reduce computational cost, the operator has to be truncated. Coupled cluster doubles (CCD) is the lowest approximation among the CC methods, and it only includes  $\mathbf{T}_2$ . Coupled cluster singles and doubles (CCSD) is a more comprehensive model than CCD because it comprises of both  $\mathbf{T}_1$  and  $\mathbf{T}_2$  into the cluster operator. To progress in inclusiveness, CCSD(T) adds singles, doubles and triples to the CC method. The more terms are included, the higher the computational cost.

#### 3.5.4 CBS-QB3 Method<sup>22-25</sup>

The computational method used extensively throughout this thesis is CBS-QB3, a composite model that uses different levels of theory like those outlined in sections 3.5.1 and 3.5.2 and extrapolates the total electronic energy to the infinite or complete basis set (CBS). Total electronic energy calculation without extrapolation is done using larger basis sets. Therefore, extrapolation at infinite basis set is advantageous because only smaller basis sets are needed, and computation time can be shortened. When calculating the electronic structure of a molecule using CBS-QB3, geometries optimization and frequency calculation are performed at the B3LYP level of theory with the CBSB7 basis set, which includes 6-311G(2d,d,p). The basis set 6-311G(2d,d,p) has an additional d polarization function for second row

elements.<sup>20, 26</sup> Then, single point energy are calculated at CCSD(T)/6-31+G (d') and MP4SDQ/CBSB4 levels, to correct for correlation energy to the forth order. Finally, the total energy is extrapolated to the infinite-basis-set limit utilizing pair natural-orbital energies to estimate the error due to using finite basis sets (basis set truncation approximation) at the MP2/CBSB3 level and additively corrected to the CCSD(T) level.<sup>27-28</sup> Spin contamination is also corrected in the open-shell species by adding an empirical correction based on the deviation of  $\langle S^2 \rangle$  from the theoretical value. CBS-QB3 gives reliable geometries and energies. For example, Sirjean et al.<sup>28</sup> estimated an error of only 1-1.5 kcal/mol during the calculation of the energetics for diradical species in the family of pentanediyls and hexanediyls isomers using CBS-QB3. This calculation error estimated by Sirjean can be converted from kcal/mol to eV, which becomes 0.04 - 0.06 eV.<sup>28</sup> Adiabatic ionization energy should also carry this range of error, which is acceptable in the data analysis presented in this thesis.

### 3.6 Using Theoretical Methods

CBS-QB3 calculations can greatly assist in the analysis of combustion or aerosol oxidation intermediates and/or products, specifically when literature values of their ionization energy and photoionization cross-section are not known. As shown in equation 3.1, the heat of reaction of the photoionization process is equivalent to ionization energy. Therefore, to calculate AIE, the following simple equation can be used:

$$AIE = ZPE_i^{CBS-QB3} - ZPE_n^{CBS-QB3} \quad (3.15)$$

The CBS-QB3 AIE is simply the difference between the zero-point energy (ZPE) corrected total electronic energies of the cationic (i) molecule and that of the neutral (n). The CBS-QB3 ZPE corrected total electronic energy is also useful for obtaining other thermodynamic quantities. In fact, we know from Hess's law that the difference between the summation of the formation enthalpy of the products (each multiplied by its own stoichiometric coefficient) and the summation of the formation enthalpy of the reactants (each multiplied by its own stoichiometric coefficient) is defined as reaction enthalpy. This law can be written in the following form using the computed energies:

$$\Delta H_{\text{rxn}} = \sum \text{ZPE}_{\text{products}}^{\text{CBS-QB3}} - \sum \text{ZPE}_{\text{reactants}}^{\text{CBS-QB3}} \quad (3.16)$$

In addition to providing important thermodynamic information, CBS-QB3 optimized geometries allow for prediction of photoionization spectra. All CBS-QB3 calculations are done in the Gaussian G09 (G09) program.<sup>29</sup> A typical procedure for simulating a photoionization spectrum is described as follows. Optimized geometries of a neutral molecule and its cationic counterpart are used as input in the FCFGAUSS program developed by Chen et al.<sup>30-31</sup> in order to extract the Duschinsky rotation<sup>32</sup> matrix ( $\mathbf{J}''$ ), and  $\mathbf{K}''$  vectors, which are geometrical displacements along each normal mode of vibration in the cation relative to the neutral molecule. Duschinsky rotation, or the rotation of the atoms in a molecule when the molecule is excited from the neutral ground-state to the excited electronic state, needs to be included for better accuracy.  $\mathbf{J}''$  and  $\mathbf{K}''$  are related to the mass-weighted Cartesian coordinates ( $\mathbf{Q}''$  and  $\mathbf{Q}'$ ) for the cation and the neutral molecule, respectively, by the relationship below.

$$\mathbf{Q}'' = \mathbf{J}''\mathbf{Q}' + \mathbf{K}'' \quad (3.17)$$

The calculated CBS-QB3 harmonic vibrational frequencies and the K vectors extracted by a different program, FCFGAUSS, can be used to calculate Franck-Condon factors by means of the PESCAL program,<sup>33-34</sup> which uses the Sharp-Rosenstock-Chen method.<sup>35-36</sup> Independent harmonic oscillators with the Duschinsky rotation<sup>32</sup> are included in all normal vibrational modes. This simulation generates a photoelectron spectrum (PE) for the electronic transition from the neutral to the cation. This PE spectrum is then integrated to produce a photoionization efficiency spectrum within the program. The Franck-Condon<sup>37-40</sup> and Franck-Condon-Herzberg-Teller (FCHT) method<sup>39</sup> within the G09 program<sup>29</sup> is also used to simulate photoionization spectra in this thesis. Utilizing the Duschinsky rotation matrix,<sup>32</sup> the FCHT method calculates the vibrational modes of the molecules. Then, the program approximates the FC overlap integrals using a set of recursive formulae developed by Ruhoff,<sup>41</sup> who uses the Sharp-Rosenstock<sup>35</sup> and the Lermé methods in his model.<sup>42</sup> Simulated PE spectra are calculated from the FC overlap integral, and are then integrated manually using IGOR,<sup>2</sup> yielding photoionization spectra. If the simulated spectrum of a species matches the experimental photoionization curve, an assignment can be made.

### 3.7 References

1. Osborn, D. L., et al., The Multiplexed Chemical Kinetic Photoionization Mass Spectrometer: A New Approach to Isomer-Resolved Chemical Kinetics. *Rev. Sci. Instrum.* **2008**, 79, 104103.
2. Igor Pro 6, WaveMetrics, Inc.: 2007.
3. Gross, J. H., *Mass Spectrometry: A Textbook*; Springer: Berlin, 2004.
4. Marr, G. A., *Photoionization Processes in Gases*; Academic Press: New York, 1967.



5. Born, M.; Oppenheimer, R., Zur Quantentheorie Der Molekeln. *Annalen der Physik* **1927**, 389, 457-484.
6. Seiler, R., A Remark on the Born–Oppenheimer Approximation. *Int. J. of Quant. Chem.* **1969**, 3, 25-32.
7. Franck, J.; Dymond, E. G., Elementary Processes of Photochemical Reactions. *Trans. Faraday Soc.* **1926**, 21, 536-542.
8. Condon, E., A Theory of Intensity Distribution in Band Systems. *Phys. Rev.* **1926**, 28, 1182-1201.
9. Mozhayskiy, V. A.; Krylov, A. I. *Ezspectrum*.  
<http://iopenshell.usc.edu/downloads>.
10. Dunbrack, R. L., Calculation of Franck-Condon Factors for Undergraduate Quantum Chemistry. *J. Chem. Educ.* **1986**, 63, 953.
11. Lee, P.; Weissler, G. L., The Photoionization Cross-Section of Neon. *P. Roy. Soc. Lond. A Mat.* **1953**, 220, 71-76.
12. Cool, T. A.; Wang, J.; Nakajima, K.; Taatjes, C. A.; McLlroy, A., Photoionization Cross Sections for Reaction Intermediates in Hydrocarbon Combustion. *Int. J. Mass. Spectrom.* **2005**, 247, 18-27.
13. Welz, O., et al., Low-Temperature Combustion Chemistry of Biofuels: Pathways in the Initial Low-Temperature (550 K-750 K) Oxidation Chemistry of Isopentanol. *Physical Chemistry Chemical Physics* **2012**, 14.
14. Cool, T. A., et al., Selective Detection of Isomers with Photoionization Mass Spectrometry for Studies of Hydrocarbon Flame Chemistry. *J. Chem. Phys.* **2003**, 119, 8356-8365.
15. Schrödinger, E., An Undulatory Theory of the Mechanics of Atoms and Molecules. *Phys. Rev.* **1926**, 28, 1049–1070.
16. Jensen, F., *Introduction to Computational Chemistry*; John Wiley & Sons: Chichester, 1999.
17. Hohenberg, P.; Kohn, W., Inhomogeneous Electron Gas. *Phys. Rev.* **1964**, 136, B864-B871.
18. Kohn, W.; J., S. L., Self-Consistent Equations Including Exchange and Correlation Effects. *Phys. Rev.* **1965**, 140, A1133–A1138.
19. Becke, A. D., A New Mixing of Hartree–Fock and Local Density-Functional Theories. *J. Chem. Phys* **1993**, 98, 1372-1377.

20. Becke, A. D., Density-Functional Thermochemistry. III. The Role of Exact Exchange. *J. Chem. Phys.* **1993**, 98, 5648-5652.
21. Møller, C.; Plesset, M. S., Note on an Approximation Treatment for Many-Electron Systems. *Phys. Rev.* **1934**, 46, 618-622.
22. Ochterski, J. W.; Petersson, G. A.; Montgomery, J. A., A Complete Basis Set Model Chemistry. V. Extensions to Six or More Heavy Atoms. *J. Chem. Phys.* **1996**, 104, 2598-2619.
23. Petersson, G. A.; Malick, D. K.; Wilson, W. G.; Ochterski, J. W.; Montgomery, J. A.; Frisch, M. J., Calibration and Comparison of the Gaussian-2, Complete Basis Set, and Density Functional Methods for Computational Thermochemistry. *J. Chem. Phys.* **1998**, 109, 10570-10579.
24. Montgomery, J. A., Jr.; Frisch, M. J.; Ochterski, J. W.; Petersson, G. A., A Complete Basis Set Model Chemistry. VI. Use of Density Functional Geometries and Frequencies. *J. Chem. Phys.* **1999**, 110, 2822-2827.
25. Montgomery, J. A., Jr.; Frisch, M. J.; Ochterski, J. W.; Petersson, G. A., A Complete Basis Set Model Chemistry. VII. Use of the Minimum Population Localization Method. *J. Chem. Phys.* **2000**, 112, 6532-6542.
26. Lee, C.; Yang, W.; Parr, R. G., Development of the Colle-Salvetti Correlation-Energy Formula into a Functional of the Electron Density. *Phys. Rev. B* **1988**, 37, 785-789.
27. Nyden, M. R.; Petersson, G. A., Complete Basis Set Correlation Energies. I. The Asymptotic Convergence of Pair Natural Orbital Expansions. *J. Chem. Phys.* **1981**, 75, 1843-1862.
28. Sirjean, B.; Fournet, R.; Glaude, P.-A.; Ruiz-López, M. F., Extension of the Composite Cbs-Qb3 Method to Singlet Diradical Calculations. *Chem. Phys. Lett.* **2007**, 435, 152-156.
29. Frisch, M. J. e. a. Gaussian 09, Revision A.1; Wallingford, 2009.
30. Ng, C. Y.; Baer, T.; Powis, I., Unimolecular and Biomolecular Ion-Molecule Reaction Dynamics; Wiley & Sons: Chichester, 1994.
31. Chen, P.; Logan, C. F.; co-workers., FCF, CDECK Fortran Programs; 1993.
32. Duschinsky, F., *Physicochim. URSS* **1937**, 7, 551.
33. Ervin, K. M., *Pescal*, Fortran Program; 2010.
34. Ervin, K. M.; Ho, J.; Lineberger, W. C., Ultraviolet Photoelectron Spectrum of Nitrite Anion. *J. Phys. Chem-US* **1988**, 92, 5405-5412.

35. Sharp, T. E.; Rosenstock, H. M., Franck—Condon Factors for Polyatomic Molecules. *J. Chem. Phys.* **1964**, 41, 3453.
36. Ervin, K. M.; Ramond, T. M.; Davico, G. E.; Schwartz, R. L.; Casey, S. M.; Lineberger, W. C., Naphthyl Radical: Negative Ion Photoelectron Spectroscopy, Franck–Condon Simulation, and Thermochemistry. *J. Phys. Chem. A* **2001**, 105, 10822-10831.
37. Santoro, F.; Improta, R.; Lami, A.; Bloino, J.; Barone, V., Effective Method to Compute Franck-Condon Integrals for Optical Spectra of Large Molecules in Solution. *J. Chem. Phys.* **2007**, 126, 1-13.
38. Oehlschlaeger, M. A.; Davidson, D. F.; Hanson, R. K., Experimental Investigation of Toluene + H → Benzyl + H<sub>2</sub> at High Temperatures. *J. Phys. Chem. A* **2006**, 110, 9867-9873.
39. Baulch, D. L., et al., Evaluated Kinetic Data for Combustion Modeling: Supplement II. *J. Phys. Chem. Ref. Data* **2005**, 34, 757-1397.
40. Cool, T. A.; McIlroy, A.; Qi, F.; Westmoreland, P. R.; Poisson, L.; Peterka, D. S.; Ahmed, M., Photoionization Mass Spectrometer for Studies of Flame Chemistry with a Synchrotron Light Source. *Rev. Sci. Instrum.* **2005**, 76, 094102.
41. Ruhoff, P. T., Recursion Relations for Multi-Dimensional Franck-Condon Overlap Integrals. *Chem. Phys.* **1994**, 186, 355-374.
42. Lermé, J., Iterative Methods to Compute One- and Two-Dimensional Franck-Condon Factors. Tests of Accuracy and Application to Study Indirect Molecular Transitions. *Chem. Phys.* **1990**, 145, 67-88.

## **Chapter 4 - Synchrotron Photoionization Study of Mesitylene Oxidation Initiated by Reaction with Cl (<sup>2</sup>P) or O (<sup>3</sup>P) Radicals**

[This chapter is adopted from an article with the same title published on the Journal of Physical Chemistry A (J. Phys. Chem. A, **2014**, 118 (21), pp 3735–3748). Authors include Martin Y. Ng, Jordan Nelson, Craig A. Taatjes, David L. Osborn and Giovanni Meloni]

### **4.1 Abstract**

This work studies the oxidation of mesitylene (1,3,5-trimethylbenzene) initiated by O (<sup>3</sup>P) or Cl (<sup>2</sup>P) atoms. O (<sup>3</sup>P) initiated mesitylene oxidation was investigated at room temperature and 823 K, while Cl-initiated reaction was carried out at room temperature only. Products were probed by a multiplexed chemical kinetics photoionization mass spectrometer using the synchrotron radiation produced at the Advanced Light Source (ALS) of Lawrence Berkeley National Laboratory. Reaction products and intermediates are identified based on their time behavior, mass-to-charge ratio, ionization energies, and photoionization spectra. Branching yields are derived for the O-initiated reaction at 823 K and the Cl-initiated reaction at room temperature. Reaction schematics are proposed and presented.

### **4.2 Introduction**

Aerosols are of special interest in understanding tropospheric chemistry because these chemicals can scatter and absorb solar and infrared light when suspended in the atmosphere.<sup>1</sup> These effects change the “radiative forcing,” defined in the IPCC Third Assessment Report as the perturbation of the Earth’s net radiation

energy, and is related to the change in climate parameters.<sup>2</sup> Secondary Aerosols (SAs), a subclass of aerosol, comprise both inorganic and organic compounds.<sup>3</sup> Specifically, organic carbon makes up 24% of fine continental aerosol.<sup>3</sup> The organic portion of SAs, or secondary organic aerosols (SOAs), are formed when biogenic and anthropogenic volatile organic compounds (VOCs) in the atmosphere are oxidized photochemically.<sup>4-5</sup> Among these VOC precursors of SOAs, aromatic hydrocarbons are thought to be particularly important.<sup>6-8</sup> Substituted aromatics possess high reactivity towards hydroxyl radical and may contribute to photochemical ozone formation.<sup>9</sup>

Mesitylene (MT) (1,3,5-trimethylbenzene) is an aromatic VOC that is a component of petroleum distillate fuels<sup>10</sup> and a known environmental pollutant. Mesitylene has been detected in field measurements of vehicle emissions,<sup>10</sup> and in the exhaust of research engines.<sup>11</sup> Besides being a pollutant, mesitylene is useful for understanding the combustion of aromatic fuels.<sup>12</sup> For example, sooting characteristics of kerosene are reproduced by a surrogate blend of 23% MT and 77% n-decane.<sup>13</sup> Mensch and co-workers<sup>14</sup> found that a blend of 54% iso-octane, 18% n-dodecane and 28% MT, matched the threshold soot index of JP-8, a jet fuel. Alkylated aromatic hydrocarbons like mesitylene can be used as fuels because they have high energy density, low reactivity,<sup>15</sup> appropriate volatility, and a high octane rating.<sup>12</sup> Therefore, it is important to understand the oxidation mechanism by which mesitylene is degraded under both atmospheric and combustion conditions.

Mesitylene oxidation is typically initiated by reaction with a radical, such as





The reaction proceeds by either addition of the radical to the aromatic ring or by hydrogen abstraction.<sup>16</sup> The reaction of MT with hydroxyl radical (OH) is important in atmospheric chemistry because OH is the dominant oxidizing species in the atmosphere.<sup>4</sup> The same reaction is also vital in combustion chemistry because OH is known to control ignition in the temperature range 850-1100 K.<sup>17-18</sup> Triplet oxygen atom is another important combustion radical, generated from the  $\text{H} + \text{O}_2 \rightarrow \text{OH} + \text{O} (^3\text{P})$  reaction.<sup>19-20</sup>

The kinetics of R1 has been studied by several groups. Kramp et al.<sup>8</sup> have reported the rate constant  $k_1$  of this reaction as  $(5.73 \pm 0.53) \times 10^{-11} \text{ cm}^3 \text{ molecule}^{-1} \text{ s}^{-1}$  in the temperature range of 295-325 K at atmospheric pressure (760 ( $\pm 10$ ) Torr). According to Calvert et al.,<sup>9</sup> the 298 K rate constant for this reaction is  $5.67 (\pm 1.14) \times 10^{-11} \text{ cm}^3 \text{ molecule}^{-1} \text{ s}^{-1}$ . Under similar conditions Aschmann et al.<sup>21</sup> have proposed the Arrhenius expressions of reaction R1 as  $k_1 = 4.40 \times 10^{-12} e^{(738 \pm 176)/T} \text{ cm}^3 \text{ molecule}^{-1} \text{ s}^{-1}$  (278-347 K) and measured the rate constant to be  $5.49 (\pm 0.66) \times 10^{-11} \text{ cm}^3 \text{ molecule}^{-1} \text{ s}^{-1}$  at 298 K. The kinetics of R2 has been studied by Cvetanovic,<sup>22</sup> and the rate expression is  $9.96 \times 10^{-12} e^{-3326 [\pm 1663 \text{ J/mole}]/RT} \text{ cm}^3 \text{ molecule}^{-1} \text{ s}^{-1}$ . Atkins et al.<sup>23</sup> have suggested that the rate expression of the MT + O reaction is  $2.79 \times 10^{-12} \pm 3.32 \times 10^{-13} \text{ cm}^3 \text{ molecule}^{-1} \text{ s}^{-1}$  at 300 K. In another study, Atkins et al.<sup>24</sup> have determined the rate expression to be  $1.0 \times 10^{-11} e^{-3218 [\pm 8314472 \text{ J/mole}]/RT} \text{ cm}^3 \text{ molecule}^{-1} \text{ s}^{-1}$  at 299 - 392 K.

In addition to kinetics studies, there have been several attempts to identify the products of mesitylene oxidation. Using FTIR spectroscopy in an aerosol

chamber study, Holes et al.<sup>25</sup> have concluded that the oxidation of mesitylene under atmospheric conditions produces aerosols whose constituent molecules have an average of three carbonyl and one hydroxyl groups. Smith and co-workers<sup>26</sup> sampled products of the hydroxyl-radical-initiated oxidation of mesitylene at 298 K and atmospheric pressure, using GC, HPLC, and GC-MS, and detected 3,5-dimethylbenzaldehyde, 2,4,6-trimethylphenol, and a range of multiple oxygenated products using the Master Chemical Mechanism (MCMv3.1; <http://mcm.leeds.ac.uk/MCM>) MT scheme developed from literature information on aromatic chemistry and evaluated via photosmog chamber experiments by Bloss et al.<sup>27-28</sup> Employing Chemical Ionization Reaction Time-of-Flight Mass Spectrometry (CIR-TOF MS), Wyche et al.<sup>5</sup> and Rickard et al.<sup>29</sup> studied the OH-initiated mesitylene oxidation at atmospheric pressure and room temperature ( $20 \pm 1$  °C). They observed that 2,4,6-trimethylphenol (246TMP) and 3,5-dimethylbenzaldehyde (35DMBZ) are the early stage ring retaining products formed.

While aromatics + O(<sup>3</sup>P) reactions are not important to atmospheric chemistry, they have been demonstrated to be potentially important in high concentration VOC and NO<sub>x</sub> chamber experiments or high-[NO<sub>2</sub>] polluted plumes.<sup>15</sup> The mesitylene + O(<sup>3</sup>P) reaction was studied by Sloane<sup>30</sup> using crossed molecular beams and low-energy-electron ionization mass spectrometric detection, and by Parker and Davis<sup>31</sup> in Ar matrices using an infrared spectroscopic probe. Sloane observed the O addition product at  $m/z = 136$ , with an ionization threshold near 8 eV; however, no isomeric assignment was made because the ionization energies of the possible products, i.e., 246TMP, 3,5-dimethylbenzyl alcohol (35DMBA), and 3,5-dimethylanisole, were unknown. Sloane also observed  $m/z = 134$ , which he tentatively assigned to 3,5-

dimethylbenzaldehyde, and  $m/z = 108$ , assigned as an open-chain olefin or a dissociative ionization fragment. The Ar matrix study by Parker and Davis<sup>31</sup> identified 246TMP as a product of O + mesitylene, and observed a ketene moiety containing ring-opening product 2,4-dimethyl-1,3,5-heptatrien-1-one. In the present work a multiplexed mass spectrometer coupled with a tunable synchrotron radiation source provides time-resolved profiles of reactants and products over the first 70 ms following pulsed-laser initiation. Tunable photoionization has the capability to identify isomeric species via photoionization spectra. Using this technique this investigation aims to supplement earlier studies<sup>5, 25-26, 29-31</sup> with a definitive identification of the species, intermediates and products, of the primary chemistry in the reaction with O atoms and in Cl-initiated oxidation of mesitylene. The study of mesitylene + O (<sup>3</sup>P) at room temperature and 823 K elucidates the O addition pathway, where a product of an intersystem crossing is observed. On the other hand, mesitylene + Cl + O<sub>2</sub> reaction at 298 K is used to study the H-abstraction pathways.

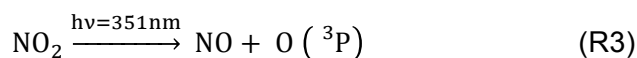
### 4.3 Experiment

All reactions are carried out at the Advanced Light Source (ALS) of Lawrence Berkeley National Laboratory. Reaction intermediates and products are probed by a multiplexed time- and energy-resolved mass spectrometer, using the continuously tunable synchrotron radiation produced at the ALS as photoionization source. A detailed description of the instrument has been provided previously.<sup>32-35</sup> Mesitylene ( $\geq 99.0\%$ ) is transported into the gas phase by bubbling helium through the temperature-controlled liquid. To produce oxygen atoms in their ground state (O (<sup>3</sup>P)), a mix of 1% NO<sub>2</sub> in helium is used as photolytic source, and similarly a 1% Cl<sub>2</sub> mix in



helium is used as a chlorine radical precursor. All gaseous reactants are introduced into a slow-flow quartz reaction tube via calibrated mass flow controllers. Nichrome heating tape is wrapped around the reaction tube, so that reactions can be studied from 298 K to higher temperatures. MT + O(<sup>3</sup>P) is studied at room temperature and 823 K, while MT + Cl + O<sub>2</sub> at room temperature only. The pressure can be varied (the present experiments employed 4 Torr at room temperature and 7 Torr at 823 K) by using a feed-back controlled throttle valve that connects the reaction cell to a Roots pump. The gas mixture effuses through a 650 μm-wide pinhole on the side of the reactor and is skimmed into the differentially pumped region of the instrument where tunable synchrotron radiation photoionizes the gas molecules. Then, ions are accelerated and detected by an orthogonal acceleration time-of-flight mass spectrometer pulsed at 50 kHz, which provides a mass resolution of approximately 1600. The repetition rate and the voltages of the extraction region of the instrument determine the maximum observable mass-to-charge ratio, which was m/z = 155 based on the setting of these two parameters at the time of these experiments.

The gas mixture is photolyzed by a 4 Hz-pulsed unfocused 351 nm (XeF) excimer laser. Number densities for mesitylene are  $5 \times 10^{12} - 6 \times 10^{13}$  molecules cm<sup>-3</sup>, for NO<sub>2</sub>  $8 \times 10^{14} - 1 \times 10^{15}$  molecule cm<sup>-3</sup>,  $5 \times 10^{16}$  molecules cm<sup>-3</sup> for O<sub>2</sub> and  $7 \times 10^{14}$  molecules cm<sup>-3</sup> for Cl<sub>2</sub>. O (<sup>3</sup>P) is generated by photolysis of NO<sub>2</sub> according to the following reaction:



At 351 nm, the quantum yield of triplet oxygen atom from NO<sub>2</sub> photolysis is 1.00 according to Troe,<sup>36</sup> and absorption cross section is 4.62 × 10<sup>-19</sup> cm<sup>2</sup> according to Vandaele and co-workers.<sup>37</sup> Calculated from the recommended quantum yield and the absorption cross section of the NO<sub>2</sub> photolysis, number densities for O (<sup>3</sup>P) varies between 3-4 × 10<sup>13</sup> molecules cm<sup>-3</sup>. Chlorine atoms, on the other hand, are yielded by photolysis of Cl<sub>2</sub> according to the following reaction:



The recommended quantum yield of the Cl<sub>2</sub> photolysis is 1.00 according to the IUPAC Subcommittee for Gas Kinetic Data Evaluation<sup>38</sup> while the absorption cross section is 1.82 × 10<sup>-19</sup> cm<sup>2</sup> according to Maric et al. at 351 nm.<sup>39</sup> Based on these recommended values, the number density for Cl atoms is 2 × 10<sup>13</sup> cm<sup>-3</sup>. The reference photoionization spectra of putative products of the mesitylene oxidation including 3,5-dimethylbenzaldehyde (35DMBZ) (97%), 246TMP (97%), and 3,5-dimethylphenol (35DMP) (99%) were recorded on the same instrument for product identification and quantification.

Ion intensity (I), reaction time (t), photon energy (E), and mass-to-charge ratio (m/z) are recorded simultaneously during the experiment. Ion signal is background subtracted and normalized by the ALS photon current at each photon energy step. The ion intensity is plotted as a function of t, E, and m/z. Integration of the ion intensity over the whole photon energy spectrum at a particular m/z yields a plot of ion intensity versus time. This plot describes the concentration-vs-time profile of the species appearing at that specific m/z as shown in Figure 1a. The reaction starts when the photolysis laser is fired, corresponding to t = 0. Similarly, integration of the

ion signal of a specific  $m/z$  over the reaction time range yields a plot of the ion intensity as a function of photon energy, which is the photoionization spectrum (PIS). Comparison of literature, measured, or calculated photoionization spectra with the experimental data allows the identification of reaction species. This procedure is particularly useful to distinguish isomers. In fact, photoionization spectra of different species differ in threshold energy because of different ionization energies, and also differ in shape due to different geometries and vibrational modes, and therefore Franck-Condon (FC) factors.

When the absolute photoionization cross-sections of reactant and products are known, the concentrations of the products relative to the reactant can be determined, enabling the calculation of the branching fractions. In this investigation products are observed from primary and secondary chemistry, so the term branching yield is preferred, which include the yield of a product from several possible reactions with respect to the reactant. The absolute photoionization spectrum of the molecule of interest can be obtained by comparing the experimental data with the absolute photoionization spectrum of a known species, such as propene. The ion signal ( $S$ ) of a molecule is the product of the instrumentation constant ( $k$ ), the photoionization cross-section ( $\sigma$ ), the mass-dependent response ( $\delta$ ), which in our experiments is approximately equal to the mass ( $m$ ) to the power of 0.67, and the concentration ( $C$ ) of the molecule.

$$S = k \sigma \delta C \quad (4.1)$$

The branching yield is the quotient of the concentration of the product ( $P$ ) over the starting material ( $R$ ), and thus,

$$\frac{C_P}{C_R} = \frac{\frac{S_P}{\sigma_P \delta_P}}{\frac{S_R}{\sigma_R \delta_R}} = \frac{S_P \sigma_R \delta_R}{S_R \sigma_P \delta_P} = \frac{S_P \sigma_R}{S_R \sigma_P} \left(\frac{m_R}{m_P}\right)^{0.67} = \frac{S_P \sigma_R}{S_R \sigma_P} \text{MDF} \quad (4.2)$$

where MDF is the mass discrimination factor. The ion signal of the product and reactant is best compared at a photon energy where both photoionization spectra exhibit plateaus. Based on the uncertainties of the published photoionization cross-sections and the experimental uncertainty of our measurements, the calculated branching yields are expected to be reliable within 20 %.

To calculate the branching yields, the reference photoionization spectra of mesitylene, 246TMP, 35DMBZ, and 35DMP are recorded along with a gas calibration mixture that contains an exact known amount of ethene, propene, and 1-butene. Then, these spectra are compared at the same photon energy to the absolute photoionization spectrum of propene recorded by Person and Nicole.<sup>40</sup> During the comparison, the photoionization spectra are converted into absolute photoionization cross section plots through the method described above, where now the concentrations are known and the photoionization of the target molecule is unknown. The absolute photoionization cross section of mesitylene has been reported by Zhou et al.<sup>41</sup> and Kanno et al.<sup>42</sup> The cross section used in this work is about 15% higher than the published absolute photoionization cross section reported by Zhou and colleagues.<sup>41</sup> Experimental photoionization spectra of 1,2,4-trimethylcyclopenta-1,3-diene, 2,6-dimethyl-4-methylene-2,5-cyclohexadien-1-one, and 3,5-dimethylbenzyl alcohol could not be obtained, so simulated spectra are used in the analysis. The photoionization cross section is estimated to be 52, 73, and 69

Mb (1 Mb =  $1 \times 10^{-18}$  cm<sup>2</sup>), respectively, at 11.8 eV using the semi-empirical model provided by Bobeldijk et al.<sup>43</sup>

#### 4.4 Computational Methods

Electronic structure calculations are performed employing the CBS-QB3 composite method<sup>44-45</sup> using the Gaussian 03 program<sup>46</sup> to obtain optimized molecular structural parameters, such as bond lengths, bond angles, harmonic vibrational frequencies, force constants, and ionization energies. Adiabatic ionization energies (AIE) are calculated using the difference between the zero-point vibrational (ZPE) corrected electronic energies of the ground electronic states of the neutral and the cationic molecule. Table 1 lists all the relevant chemical species of this investigation, with their abbreviated names, and calculated AIE values. ZPE corrected total electronic energies are also used to calculate heat of reactions ( $\Delta_r H$ ) to show that proposed mechanisms are thermodynamically feasible. In addition, they are employed in connection with available literature enthalpies of formation ( $\Delta_f H$ ) of the elements in the gas phase to derive the enthalpy of formation at 0 or 298 K for the species of interest, according to the reaction  $C_x H_y O_z(g) \rightarrow xC(g) + yH(g) + zO(g)$ . The potential energy surface (PES) of the mesitylene + O (<sup>3</sup>P) reaction system is probed by relaxed PES scans at the B3LYP/CBSB7 level (the level for geometric optimization in CBS-QB3). Saddle points are identified from energy maxima in these scans, respectively, with the criteria of having one imaginary vibrational frequency. Saddle point geometries are then optimized with respect to the imaginary frequency with the CBS-QB3 method. Intrinsic reaction coordinate calculations (forward/reverse) are utilized to verify minima on either side of a saddle point geometry. When

determining the exothermicity of individual radical reactions, the enthalpy changes in  $\text{kJ mol}^{-1}$  are obtained from the difference with the  $\text{MT} + \text{Cl}$  or  $\text{MT} + \text{O} (^3\text{P})$  reactants used as zero (reference point) and the values are indicated in all schematics in square brackets. The heat of reaction ( $\text{kJ mol}^{-1}$ ) for individual reactions is also included in parentheses for comparison with other systems like benzene +  $\text{O} (^3\text{P})$ .<sup>47</sup>

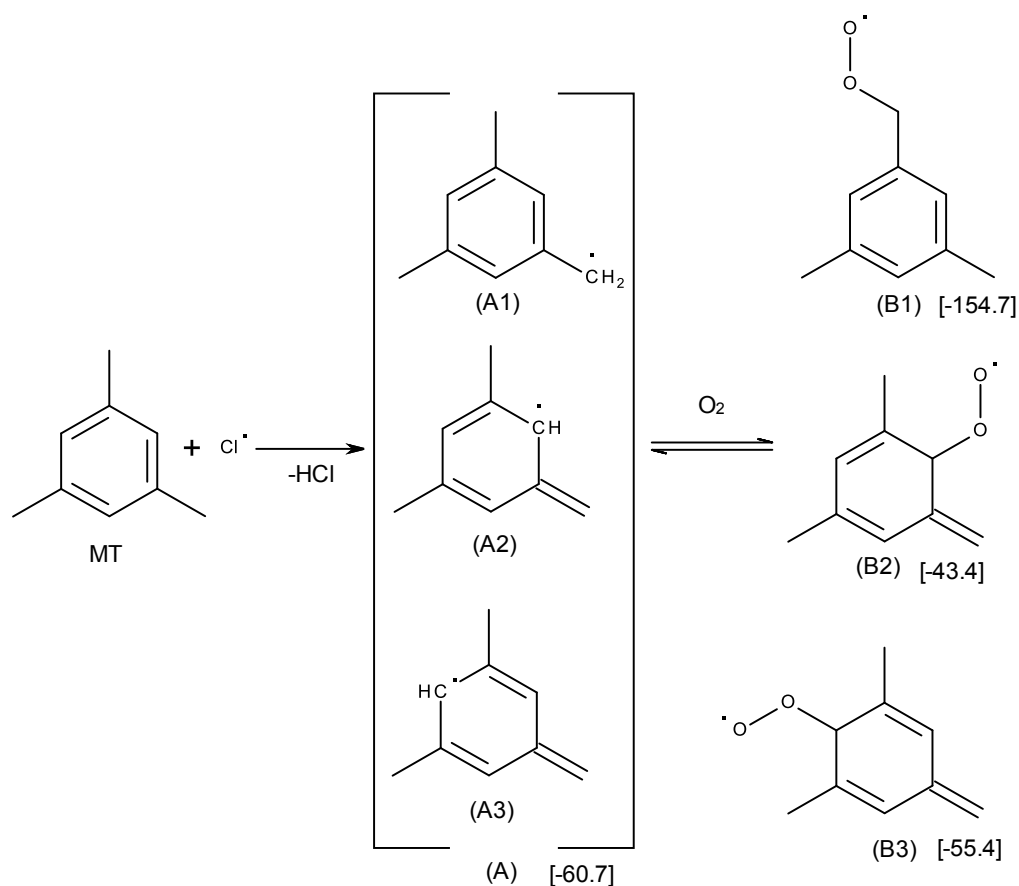
Whenever the photoionization spectrum of a reaction species is not available from literature or it cannot be measured experimentally, a Franck-Condon (FC) spectral simulation is obtained using the PESCAL program.<sup>48-49</sup> PESCAL generates a photoelectron spectrum by calculating FC factors for the transition between the ground vibronic states of the neutral and cation. The simulated photoelectron spectra are then integrated to yield simulated photoionization spectra. Calculations of all modes include independent harmonic oscillators with Duschinsky rotation,<sup>50</sup> using the Sharp-Rosenstock-Chen method.<sup>51-52</sup>

## **4.5 Result and Analysis**

### 4.5.1 Mesitylene + Cl + O<sub>2</sub> Reaction at Room Temperature

The oxidation of mesitylene is initiated by chlorine radicals in the presence of oxygen at room temperature. The reaction of mesitylene and Cl proceeds through two competing routes, namely, addition of chlorine atom to the aromatic ring structure and H atom abstraction by chlorine. The usage of Cl atoms instead of OH radicals in this investigation allows the addition channel (whose products will include Cl atoms) to be easily distinguished, a distinction that is more difficult for the OH addition reaction. The rate constant of  $\text{MT} + \text{Cl}$  reaction is  $2.26 - 2.66 \times 10^7$

$10^3 \text{ cm}^3 \text{ molecule}^{-1} \text{ s}^{-1}$  according to an earlier study.<sup>53</sup> At room temperature chlorine addition is expected to dominate the reaction. At atmospheric pressure, according to Wyche et al.<sup>5</sup> the reaction of MT + OH proceeds mainly (97%) to the addition channel, while H-abstraction contributes only 3% calculated from the Master Chemical Mechanism (MCMv3.1) scheme. However, in the low-pressure experiments described here abstraction is expected to be much more prominent, and the observed branching yields suggest that H-abstraction constitutes about half of the total reaction. The predominant H abstraction from mesitylene by Cl will form a resonance-stabilized mesitylenyl radical (A1) with its resonance structures A2 and A3 depicted in the following reaction schematic (the numbers in square brackets are relative to MT + Cl, which is the reference):

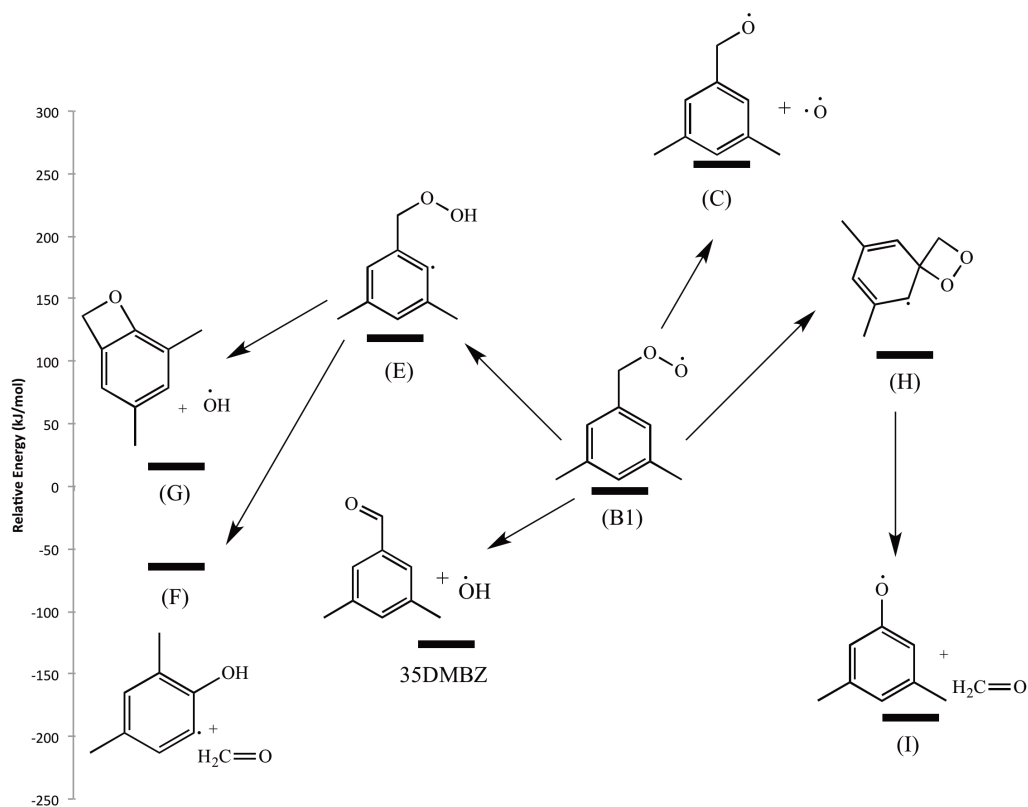


(Scheme 4-1a)

The heat of reaction for abstracting a hydrogen atom from the methyl group (about -61 kJ mol<sup>-1</sup> calculated at the CBS-QB3 level) is far more favorable than abstracting a hydrogen atom from the aromatic ring (+43 kJ mol<sup>-1</sup> calculated at the CBS-QB3 level). Three binding sites for oxygen are present, resulting in three distinct mesitylenylperoxy radicals (B1, B2, and B3).

The mesitylenylperoxy radical follows the general oxidation mechanism outlined for other similar systems,<sup>54-56</sup> as depicted in the following reaction schematic for the most stable configuration (B1):



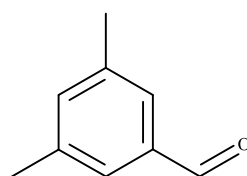


(Scheme 4-1b)

The fate of the mesitylenylperoxy is thought to be similar to that of benzyl peroxy, o-xilylperoxy, m-xilylperoxy, and p-xilylperoxy radicals proposed by Murakami et al.<sup>55-</sup>

<sup>56</sup> There are four channels shown in Scheme 4-1b for the unimolecular decomposition of mesitylenylperoxy. The barriers to unimolecular decomposition reactions are likely too high to allow these reactions to be significant in the troposphere. The first channel is the cleavage of the O—O bond and loss of an oxygen atom, forming mesitylenyloxy radical (C). The relative heat of reaction of this step is calculated to be  $+103 \text{ kJ mol}^{-1}$  and should be unimportant at 300 K. The second channel involves the terminal oxygen abstracting a hydrogen atom

intramolecularly from the closest methylene group, which is the  $\alpha$ -C. The OH group subsequently leaves the molecule, creating 35DMBZ. The calculated relative heat of this reaction is  $-277 \text{ kJ mol}^{-1}$ . The four-membered ring transition states for the initial internal abstraction in xylyl radicals<sup>56</sup> lie substantially ( $\sim 160 \text{ kJ mol}^{-1}$ ) above the  $\text{RO}_2$  well, and barriers can be expected to be similarly high in the mesitylenyl +  $\text{O}_2$  reaction.



3,5-dimethylbenzaldehyde

The third channel of mesitylenylperoxy decomposition proceeds via intramolecular abstraction of the H on the benzene ring, forming (E), a QOOH species. The abstraction of H that is bonded to an  $\text{sp}^2$  carbon is exothermic (CBS-QB3 value of  $-35 \text{ kJ mol}^{-1}$ ). Nevertheless, neither formaldehyde nor the bicyclic compound (G) (calculated AIE of 7.91 eV) are observed, suggesting a high energy barrier to formation of QOOH and/or final products. The potential energy surface of isobutenyl +  $\text{O}_2$ , which is analogous to the mesitylenyl system in that the radical center can be delocalized throughout the molecule, was investigated by Chen et al.<sup>57</sup> using a combination of different electronic structure methods and also by Zheng et al.<sup>58</sup> at the CBS-QB3 level. Both groups place the 2-methyl-2-propenylperoxy ( $\text{H}_2\text{C}=\text{C}(\text{CH}_3)\text{CH}_2\text{OO}\cdot$ ) higher in energy than 1-hydroperoxy-2-methyl-2-propenyl ( $\text{H}_2\text{C}=\text{C}(\text{CH}_3)\text{C}(\text{H})\cdot\text{OOH}$ ) formed through intramolecular abstraction of the hydrogen on the carbon bonded to the peroxy group. While Zheng<sup>58</sup> did not provide the

enthalpy of formation of  $\text{H}_2\text{C}=\text{C}(\text{CH}_3)\text{C}(\text{H})\cdot\text{OOH}$ , from the heat of formation of  $\text{H}_2\text{C}=\text{C}(\text{CH}_3)\text{CH}_2\text{OO}\cdot$  and  $\text{H}_2\text{C}=\text{C}(\text{CH}_3)\text{C}(\text{H})\cdot\text{OOH}$  provided by Chen and Bozzelli,<sup>57</sup> the exothermicity of the reaction is calculated to be about  $-8 \text{ kJ mol}^{-1}$ . In the present investigation, because the formation reactions of (A) and (B1) are very exothermic ( $-61$  and  $-94 \text{ kJ mol}^{-1}$ ) due to the extra stabilization from the delocalization of the radical center throughout the ring on (A) including the methylene group and the exothermic binding of molecular oxygen to the radical center, the endothermic ( $120 \text{ kJ mol}^{-1}$ ) reaction of (B1) to (E) becomes exothermic relative to  $\text{MT} + \text{O}_2 + \text{Cl}$ , the reference energy level. The fourth and final channel of mesitylenylperoxy degradation has a total exothermicity of  $-48 \text{ kJ mol}^{-1}$ . However, there is no evidence for this channel: we observe neither formaldehyde nor (I). Among all the possible products proposed in S1b, only 35DMBZ is observed.

When comparing the time traces of the reactant, mesitylene ( $m/z = 120$ ), and the  $m/z = 119$ , 134, and 136 species (Figure 1a), it is found that the time trace of  $m/z = 119$  exhibits a sharp rise followed by a fast decay, a kinetic pattern typical of a radical. In Figure 1b, the time profile of  $m/z = 119$  in the 8-10 eV photon energy range rises sharply and decays to zero, while in the 10-11.2 eV range it rises sharply but decays to a non-zero level. The first time trace indicates the formation of mesitylenyl species ( $m/z = 119$ ). On the other hand, the second time profile like the one in Figure 1a plateaus at about 10 ms at a non-zero level. This could be explained by the fact that once mesitylenyl radical is formed, molecular oxygen binds to the radical center forming mesitylenylperoxy ( $m/z = 151$ ). Mesitylenylperoxy radicals (B1, B2 and B3) are not stable, and they are quickly ionized and fragmented into  $m/z = 119$  daughter ion and oxygen. The calculated adiabatic ionization energy

of mesitylenyl is 7.03 eV, while the ionization of the neutral to the first triplet cation state is 8.56 eV. Mesitylenyl peroxy radical can fragment through dissociative photoionization to neutral molecular oxygen and mesitylenyl cation in either the singlet or triplet state. The calculated appearance energies of singlet mesitylenyl cation from the dissociative ionization of the three peroxy radicals, B1, B2, and B3 are 8.00, 6.85, and 6.98 eV, respectively, while thresholds for dissociative ionization to triplet mesitylenyl cation are 9.53, 8.37, and 8.50, respectively. The photoionization spectrum of  $m/z = 119$  shows a shallow threshold at around 8.4 eV (Figure 4-1c). The onset at 8.4 eV can be assigned to the transition from B2  $\rightarrow$  mesitylenyl radical cation (triplet) + O<sub>2</sub>, because the onset is in good agreement with the CBS-QB3 calculated AE of 8.37 eV for this transition. Also, it is likely that the transitions of B1  $\rightarrow$  mesitylenyl radical cation (triplet) + O<sub>2</sub> (AE = 9.53 eV) and B3  $\rightarrow$  mesitylenyl radical cation (triplet) + O<sub>2</sub> (AE = 8.51 eV) are present. While the photoionization spectrum of the  $m/z = 119$  product does not have a prominent feature at 8.5 eV, there is an inflection at around 9.5 eV. The sharp rise of the  $m/z = 119$  time trace is due to formation of mesitylenyl radicals (A1, A2, and A3), while the sharp fall represents the formation of mesitylenylperoxy radicals (B1, B2, and B3). The non-zero stable portion of the kinetic profile of  $m/z = 119$  is most likely due to the constant formation of cations A1, A2, and A3 by dissociative ionization of long-lived peroxy radicals. The comparison of the time profiles of the  $m/z = 119$ , 134, and 136 products depicted in Figure 4-1a shows that  $m/z = 119$  product is the first species formed (peaks at about 2 ms), followed by  $m/z = 134$  and 136 (peak at about 10 ms).

Formation of 35DMBZ in the present system is confirmed by the fact that the reference photoionization spectrum of 35DMBZ is very similar in shape to the

experimental photoionization spectrum from the reaction at  $m/z = 134$  (Figure 4-2). Its observed adiabatic ionization energy is  $8.85 \pm 0.05$  eV, while its calculated AIE is 8.95 eV. The kinetic profile of  $m/z = 134$  shows fast formation, consistent with the time trace of a primary product. The photoionization of 35DMBZ generates a dissociative ionization fragment at  $m/z = 133$ . The time behavior of the signal at  $m/z = 133$  agrees with that at  $m/z = 134$  to within the signal-to-noise ratio (Figure 4-3a). The shape of the experimental photoionization spectrum of  $m/z = 133$  product in the MT + Cl + O<sub>2</sub> reaction matches very well the reference photoionization spectrum of  $m/z = 133$  35DMBZ daughter ion confirming that there is only one species contributing to the mass signal at  $m/z = 133$  (Figure 4-3b). 246TMP and 3,5-dimethylbenzyl alcohol are found in the experimental signal at  $m/z = 136$ . The signal at  $m/z = 136$  is not zero at 8.10 eV, the lowest photon energy of this photoionization spectrum, and has a slowly rising onset up to 8.45 eV (Figure 4-4). It is very likely that the 246TMP contributes to the ion signal at  $m/z = 136$ , because, of all the plausible products at  $m/z = 136$ , only 246TMP (CBS-QB3 AIE = 7.88 eV) has an ionization energy lower than 8.10 eV. Another species that may contribute to the  $m/z = 136$  signal because of its increase at 8.45 eV is 3,5-dimethylphenylmethanol, or 3,5-dimethylbenzyl alcohol (35DMBA). The calculated CBS-QB3 AIE of 35DMBA is 8.46 eV, which is in very good agreement with the experimental observed spectral feature. 35DMBA can be formed from reaction of two ROO radicals via the Russell disproportionation mechanism.<sup>59-60</sup> The enthalpy of the reaction from two molecules of (B) to form 35DMBZ, 35DMBA, and O<sub>2</sub> is calculated to be  $-368$  kJ mol<sup>-1</sup>, showing that this step is thermodynamically possible. However, the observed predominance of 35DMBZ supports that disproportionation reaction is too slow to be solely

responsible for its production. On the other hand, 246TMP most likely evolves from secondary chemistry, e.g., from the OH that is a coproduct in the formation of 35DMBZ. The fact that the time profile of  $m/z = 136$  has a very similar rise with that of the  $m/z = 134$  product may suggest 246TMP is not a secondary product. However, the  $m/z = 136$  time profile may be dominated by the formation of 35DMBA, which is produced simultaneously with 35DMBZ, rather than that of 246TMP.

Products at  $m/z = 154$  and  $m/z = 155$  were also observed, likely corresponding to chlorine addition products. Chlorine atom ( $^{35}\text{Cl}$ ) adds to mesitylene to form a Cl radical adduct with mass 155. A radical may abstract a hydrogen atom from  $m/z = 155$  to form  $m/z = 154$  product.  $m/z = 155$  is the carbon-13 isotopologue of the  $m/z = 154$  product. The  $^{37}\text{Cl}$  isotopologue that would confirm the assignment falls outside the present time-of-flight window.

In summary, the Cl-initiated oxidation of mesitylene at 4 Torr and 298 K proceeds mainly by H abstraction to form mesitylenyl radicals that subsequently yield mesitylenyl peroxy radicals by reaction with  $\text{O}_2$ . The mesitylenyl peroxy radicals react to form predominantly 35DMBZ. This is in agreement with the study by Wyche et al.<sup>4b</sup>

For the mesitylene + Cl +  $\text{O}_2$  reaction at room temperature the branching yield is calculated to be 21% for 35DMBZ. 246TMP, which is assumed to be a secondary product based on the proposed formation reaction, has a branching yield of 2%. The branching yield of 3,5-dimethylbenzyl alcohol, a proposed product of the disproportionation, is estimated to be 1%. As mentioned above, more products are observed, but they are assigned to chlorinated species, which are not considered

here. Therefore, the rest of the products (~76%) are likely related to the chlorine addition channel. The result is consistent with Holes's aerosol chamber study using FTIR,<sup>25</sup> in that a carbonyl carrier is observed (35DMBZ) as well as a hydroxyl group (246TMP). However, the ratio of the carbonyl group to hydroxyl group is far greater than 3:1 in this work, a difference likely attributable to the use of Cl-initiation rather than the OH-initiation used in Holes' work, and possibly to the difference in reaction times. This investigation also differs from the findings of Smith and co-workers<sup>26</sup> in their GC-MS study and the results of the two CIR-TOF MS studies.<sup>5, 29</sup> In all these investigations, more products were observed, including ring-opening species. Again, this difference is likely explained by the much shorter reaction time in this work (70 ms compared to an "extended period" in the GC-MS study, and 500 to over 600 minutes in the CIR-TOF MS experiments).

The most abundant product in the MT + O<sub>2</sub> + Cl reaction is 35DMBZ, a methylated benzaldehyde, in agreement with studies of benzyl radical oxidation by Clothier et al.<sup>61</sup> and Murakami et al.<sup>55</sup> in which benzaldehyde is the main product of the benzyl radical oxidation reaction. In the study of Wyche et al.,<sup>5</sup> the MCMv3.1 scheme predicted that the branching fraction of 246TMP formed from OH initiation is 0.04; in this investigation using Cl radicals, 246TMP has a branching yield of 0.02. Wyche et al.<sup>5</sup> have also determined the branching fraction of 35DMBZ to be 0.03. In contrast, the branching yield of 35DMBZ observed here is 0.16. In the same study and in Richard and coworkers' work,<sup>29</sup> it was observed that 35DMBZ and 246TMP appear the earliest amongst the ring retaining products, which is in agreement with this work. Because NO<sub>2</sub> is present in their studies,<sup>5, 29</sup> and because their reaction time is longer than the current investigation, it is expected that fewer products are

observed here. Also, oxygen-bridged peroxide bicyclic products are not observed in this work as compared to the CIR-TOF-MS studies.

#### 4.5.2 Mesitylene + O (<sup>3</sup>P) at Room Temperature and 823 K

In the mesitylene + O (<sup>3</sup>P) experiment carried out at room temperature, only one product is observed, at  $m/z = 136$ , and it is tentatively assigned as 246TMP. The main photon energy range for this experiment is 7.5 - 9.86 eV, but in single-energy measurements at 11 eV no other product was observed. The  $m/z = 136$  signal appears beginning at 7.8 eV, which is in good agreement with the calculated CBS-QB3 AIE of 246TMP (7.88 eV). The calculated AIE is also in good agreement with the ionization energy of 8.00 eV reported by Cetinkaya and coworkers.<sup>62</sup> Because of the low signal-to-noise ratio this assignment is tentative. No contribution was observed from abstraction channels due to high activation barrier ( $> + 15 \text{ kcal mol}^{-1}$ ) at room temperature for the reaction of O (<sup>3</sup>P) abstracting H atom from olefins.<sup>63-65</sup>

When the temperature is increased to 823 K, more species are detected including abstraction products. 35DMBZ whose formation through H-abstraction has already been discussed for the MT + Cl + O<sub>2</sub> reaction, is also observed at  $m/z = 134$ . Because O<sub>2</sub> is present in the 1% NO<sub>2</sub> gas mixture, used to produce O (<sup>3</sup>P), O<sub>2</sub> will be considered in the proposed reaction mechanisms. The reference photoionization spectrum of 35DMBZ matches very well with the experimental data (Figure 4-5). The formation pathway of 35DMBZ in the O (<sup>3</sup>P) initiated mesitylene oxidation is very similar to the one described in Schemes 4-1a and 4-1b, except that O (<sup>3</sup>P) is abstracting the H atom. The CBS-QB3 calculated energy for the reaction MT (C<sub>9</sub>H<sub>12</sub>) + O(<sup>3</sup>P) → C<sub>9</sub>H<sub>11</sub> + OH is  $-54 \text{ kJ mol}^{-1}$ . With the slight difference in the initiation step,



the overall CBS-QB3 calculated total exothermicity of reaction  $\text{MT} + \text{O} + \text{O}_2 \rightarrow 35\text{DMBZ} + 2\text{OH}$  is  $-270 \text{ kJ mol}^{-1}$ .

As seen in Figure 4-6, the measured photoionization spectrum of pure 246TMP is again in good agreement with the experimental data at  $m/z = 136$ . The photon energy range for this experiment is 8.02-9.85 eV. The presence of only one isomer at this mass is comparable to observations in the similar reaction of benzene with  $\text{O} (^3\text{P})$ .<sup>47</sup> In that reaction at room temperature, only one mass was found at  $m/z = 94$ , which is identified as phenol. Although the production of seven other isomers is energetically possible, only phenol was observed.

246TMP is a product of the addition channel, which is elucidated in Figure 4-7. In the benzene + O system, oxygen atom adds to the benzene ring forming a chemically activated triplet diradical.<sup>47, 66-67</sup> Because mesitylene is a methyl-substituted benzene, it is postulated that the  $\text{MT} + \text{O}$  would also lead to chemically activated triplet diradicals. Oxygen atoms add to the benzene ring of mesitylene at one of three methylated or non-methylated carbons, leading to two possible triplet adducts, (W) or (R).

When an  $\text{O} (^3\text{P})$  atom adds to a non-methylated carbon on the benzene ring, a triplet diradical (R) is formed with a calculated reaction enthalpy of  $-79 \text{ kJ mol}^{-1}$  and an energy barrier of  $3 \text{ kJ mol}^{-1}$ . One radical site is on the oxygen, while the other one is on the methylated carbon adjacent to the newly oxygenated carbon on the benzene ring. The diradical (R) can then form a 2,4,6-trimethylphenoxy radical (S) through H-elimination, with the calculated total heat of reaction of  $-93 \text{ kJ mol}^{-1}$ . The energy barrier of this step is  $35 \text{ kJ mol}^{-1}$ . After correcting for the contribution of the

$^{13}\text{C}$  isotopologue of 35DMBZ, the photoionization spectrum of  $m/z = 135$  product has too small a signal/noise to be definitively identified, but could be consistent with 2,4,6-trimethylphenoxy radical. After correction by the contribution of the  $^{13}\text{C}$  isotopologue of  $m/z = 134$ , the time trace of  $m/z = 135$  shows a typical radical kinetic pattern, a rapid formation followed by a rapid depletion (Figure 4-8). The calculated CBS-QB3 AIE of the neutral to singlet cationic state of 2,4,6-trimethylphenoxy radical is 7.75 eV, while that of the neutral to triplet cationic state is 9.07 eV. Another possibility is that  $m/z = 135$  is a dissociative ionization product of a radical with higher mass. The triplet diradical (R) could alternatively enter the singlet surface through intersystem crossing (ISC) to form mesitylenyloxide (T), similarly to the mechanism depicted in the benzene + O potential energy surface by Taatjes et al.<sup>47</sup> The calculated enthalpy of this step is  $-179 \text{ kJ mol}^{-1}$ . Mesitylenyloxide (T) can then isomerize to yield 2,4,6-trimethylcyclohex-2,4-dien-1-one (U). The CBS-QB3 total enthalpy of producing (U) through this step is  $-92 \text{ kJ mol}^{-1}$ , with a  $161 \text{ kJ mol}^{-1}$  activation barrier. There are three fates for (U), namely, the formation of 1,3,5-trimethylbicyclo[3.1.0]hex-3-en-6-one (Y), 2,4-dimethylhepta-1,3,5-trien-1-one (Z) and 246TMP. The relative energies of these three possible products (with respect to the  $\text{MT} + \text{O} (^3\text{P})$  reaction) are  $-218$ ,  $-216$ , and  $-430 \text{ kJ mol}^{-1}$ , respectively, while the energy barriers of producing them from (U) are 176, 318, and  $230 \text{ kJ mol}^{-1}$ . Since 246TMP forms through (T), a product of an intersystem crossing process, 246TMP is an ISC product. (Y) can then decompose to 2,4,6-trimethylcyclohex-2,4-dien-1-one (V) and carbon monoxide (CO) with an enthalpy of  $-98 \text{ kJ mol}^{-1}$ . The energy barrier of (V) and CO formation is  $155 \text{ kJ mol}^{-1}$ . The calculated adiabatic ionization energies of other possible 246TMP isomers (including (T), (U), (Y) and (Z)), listed in Table 2

do not match the experimental data. In fact, one onset is found, and the shape of the photoionization spectrum and the ionization energy of the experimental data correspond only to the substituted phenol.

Similarly, if an O atom adds to a methylated carbon of the benzene ring, an analogous triplet diradical (W) forms. The calculated enthalpy of this alternative step is  $-74 \text{ kJ mol}^{-1}$ , and the energy barrier of (W) formation is  $6 \text{ kJ mol}^{-1}$ . C-C bond cleavage occurs instead of a C-H scission so that a methyl group is removed from the benzene ring. Because the photon energy of the reaction is recorded only up to 9.85 eV, the methyl radical ( $9.843 \pm 0.002 \text{ eV}$ ),<sup>68</sup> is not observed. This C-C cleavage gives rise to a doublet 3,5-dimethylphenoxy radical (X), which can abstract a hydrogen atom from some source to yield 35DMP ( $m/z = 122$ ). The CBS-QB3 relative enthalpy and energy barrier of forming (X) are  $-35$  and  $27 \text{ kJ mol}^{-1}$ , respectively. Indeed, a small signal that may be attributable to 3,5-dimethylphenoxy is observed at  $m/z = 121$  (Figure 4S-4 in the supplemental material in Chapter 5S). The triplet diradical (W) can also cross to the singlet surface to form mesitylenyloxide (T). The oxygen of the mesitylenyloxide moves closer to C1, cleaving a methyl group from the mesitylenyloxide. The result is the formation of (X). However, this step, preceded by an intersystem crossing process, is endothermic, so the formation of 35DMP most likely occurs through a spin-allowed pathway.

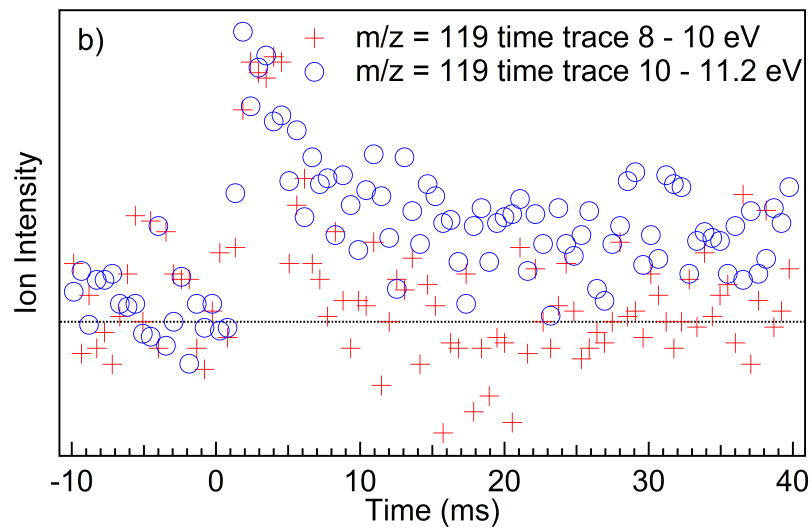
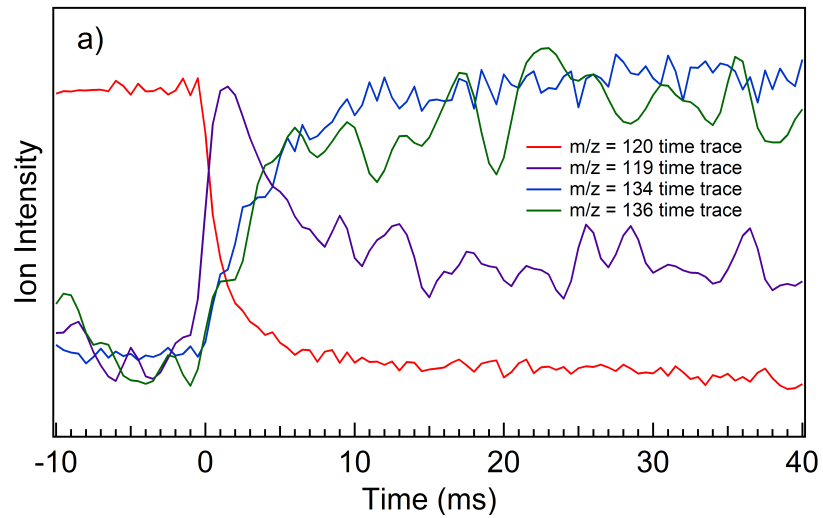
The only product identified in the mesitylene + O ( $^3\text{P}$ ) reaction at room temperature, 246TMP, has a branching yield of only 15 %. The low product recovery may indicate the formation of higher-mass or non-volatile products and, possibly, the formation of products presenting poor Franck-Condon factors upon photoionization.

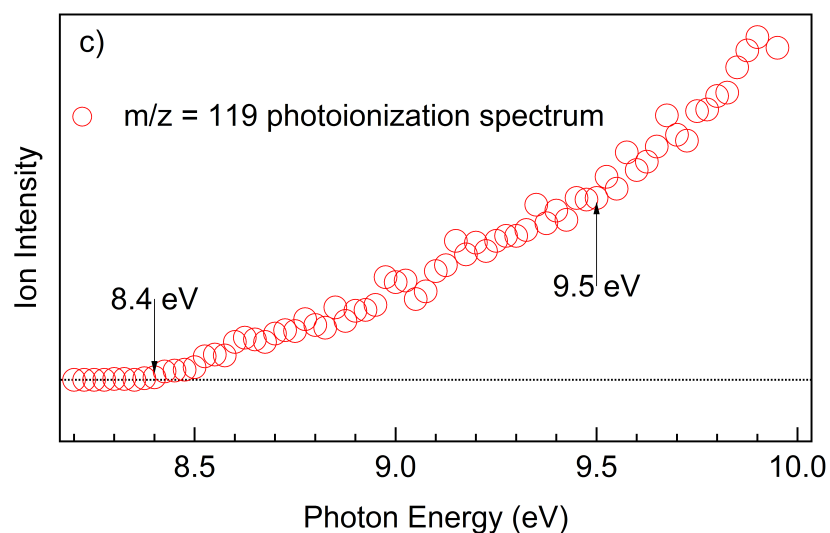
In the mesitylene + O ( $^3P$ ) at 823 K, the branching yield of 246TMP, 35DMBZ, and 35DMP are calculated to be 15, 46, and 16 %, respectively. Within the present 20 % uncertainty these results suggest a prominent role for H-abstraction at 823 K. In contrast to the benzene + O reaction where phenol is the dominant product, 246TMP, the analogue of phenol, contributes only about 15% of the depletion of mesitylene. When comparing the molecular structure of benzene and mesitylene, benzene has no hydrogen atom that can be abstracted easily, whereas mesitylene has nine benzylic hydrogen atoms. As a result, 246TMP, the addition product formed through intersystem crossing, is not the dominant species in the MT + O reaction. The result in this work confirms Sloane's claim<sup>30</sup> that 35DMBZ and 246TMP are products of the MT + O reaction and that a  $m/z = 108$  dissociative ionization fragment of other products is present. The ketene containing compound, 2,4,6-trimethyl-1,3,5-hexatrien-1-one, implied from Parker and Davis's work,<sup>31</sup> is not observed here. In contrast to the benzene + O experiment recorded by Taatjes et al.,<sup>47</sup> where all products are results of isomerization or decomposition of a product formed mainly through intersystem crossing of the adduct into singlet surface, only two products, namely 1,2,4-trimethylcyclopenta-1,3-diene and 246TMP (contributing only 16 % to the total branching ratio) are produced through an intersystem crossing in the MT + O system. The mass balance in the 823 K experiments is ~ 80%, still below unity, but approaching the estimated accuracy of the derived photoionization cross sections. Products measured by other researchers,<sup>30-31</sup> like 2,4,6-trimethyl-1,3,5-hexatrien-1-one and 3,5-dimethylanisole are not detected in this work.

## 4.6 Conclusions

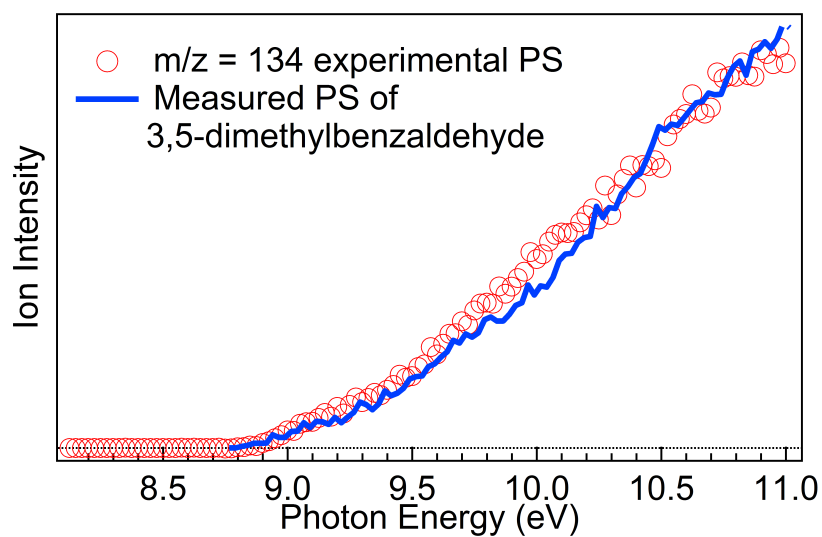
The oxidation of mesitylene is studied at the Advanced Light Source employing a multiplexed time- and energy- resolved mass spectrometer. The mesitylene + O ( $^3\text{P}$ ) reaction is used to study the O ( $^3\text{P}$ ) addition, whereas the mesitylene + Cl + O<sub>2</sub> reaction is used to investigate the H-abstraction channel. Primary reaction products are identified based on time profiles, mass-to-charge ratios, ionization energies, and photoionization efficiency spectra. In the mesitylene + O ( $^3\text{P}$ ) reaction at room temperature, only one mass is formed, identified as 2,4,6-trimethylphenol with branching yield of 16%. At 823 K, more products are observed. The main product is 3,5-dimethylbenzaldehyde, an H-abstraction species, which accounts for 46 % of the observed products. The remaining 31 % consists of addition products, 2,4,6-trimethylphenol and 3,5-dimethylphenol. The formation of 1,2,4-trimethylcyclopenta-1,3-diene and 2,4,6-trimethylphenol involve an intersystem crossing step while that of 3,5-dimethylphenol does not. In the mesitylene + Cl + O<sub>2</sub> reaction at room temperature, 3,5-dimethylbenzaldehyde with a branching yield of 21 % is the most abundant oxygenated product, while disproportionation reaction of ROO $\cdot$  is observed through the presence of 3,5-dimethylbenzyl alcohol, with an estimated branching ratio of 1 %. Figure 4-9 summarizes the proposed pathways of the oxidation of mesitylene initiated by Cl atom and O ( $^3\text{P}$ ). All primary products retain ring structures. Products with ketene group are not observed in the primary chemistry pathway.

## 4.7 Figures and Tables



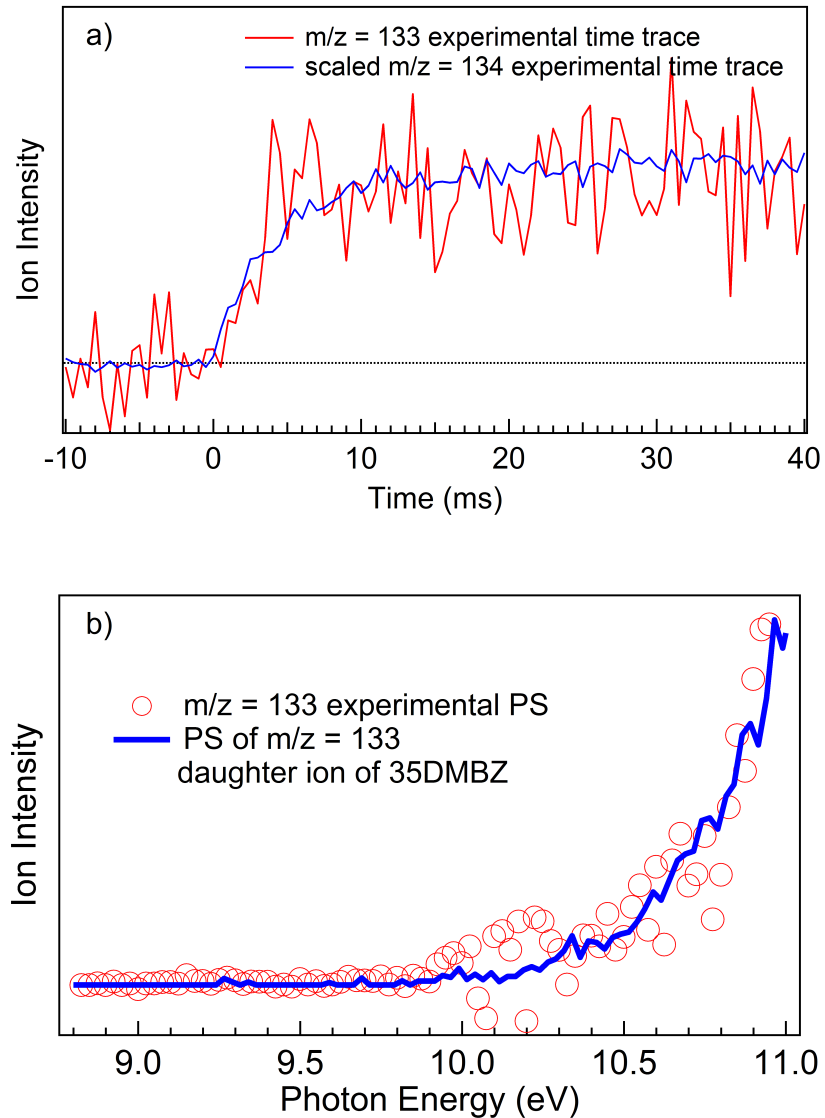


**Figure 4-1.** a) Comparison of the unscaled time trace of mesitylene ( $m/z = 120$ ) and the scaled time traces of  $m/z = 119$  (corresponding to (A1), (A2) and (A3), 134 (35DMBZ), and 136 (246TMP and (35DMPA) products of the MT + Cl + O<sub>2</sub> reaction at room temperature. b) Comparison of the scaled and unscaled time profile of  $m/z = 119$  product, which corresponds to (A1), (A2) and (A3) at photon energy 8-10 eV and at 10-11.2 eV, respectively, in the MT + Cl + O<sub>2</sub> reaction at room temperature. c) Photoionization spectrum of  $m/z = 119$  of the MT + Cl + O<sub>2</sub> reaction at room temperature.

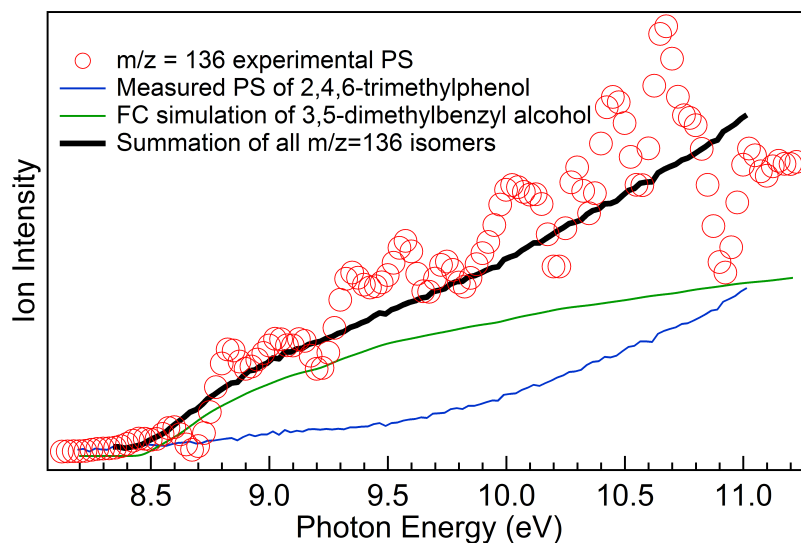


**Figure 4-2.** The measured photoionization spectrum of 3,5-dimethylbenzaldehyde (blue line) is in good agreement (with a correlation coefficient of 0.9915) with the  $m/z = 134$  experimental product spectrum (red open circles) of the  $\text{MT} + \text{Cl} + \text{O}_2$  reaction at room temperature.

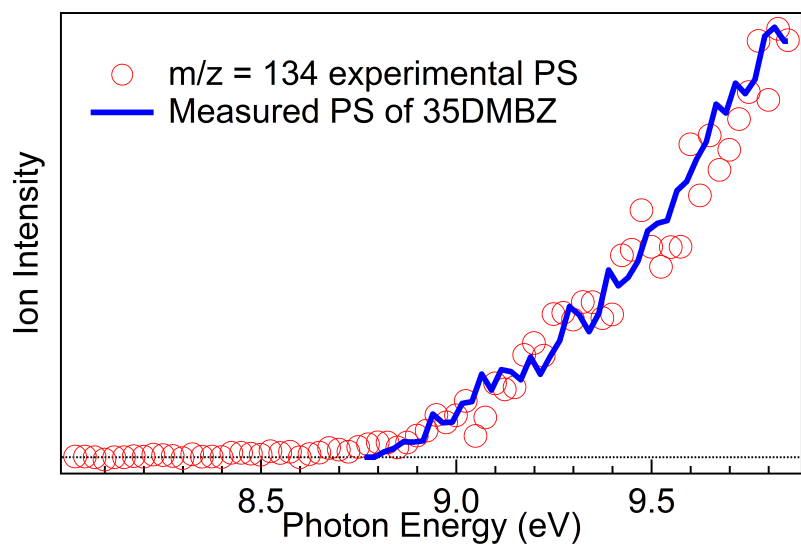




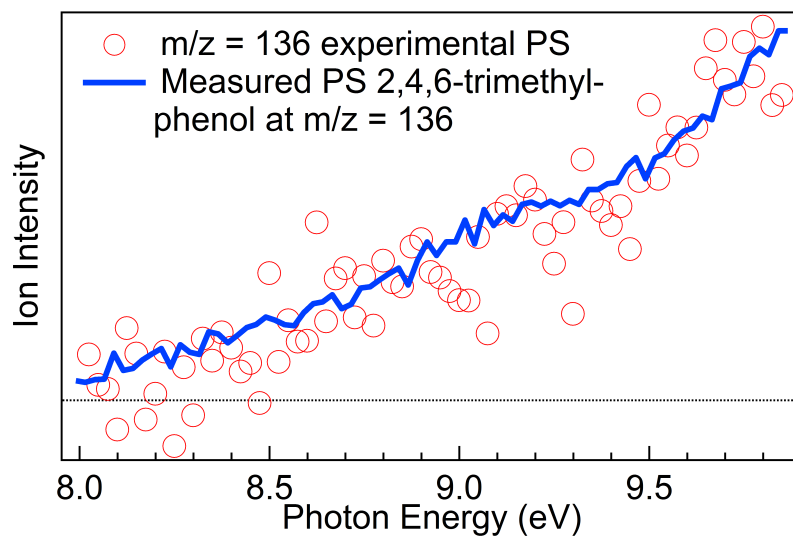
**Figure 4-3.** a) The time profile of  $m/z = 133$  (red line) compared with the time profile of  $m/z = 134$  product (blue line) from the MT + Cl + O<sub>2</sub> reaction at room temperature. b) The measured photoionization spectrum of 3,5-dimethylbenzaldehyde  $m/z = 133$  daughter ion (blue line) superimposed onto the experimental photoionization spectrum of  $m/z = 133$  product (open red circles) from the MT + Cl + O<sub>2</sub> at room temperature.



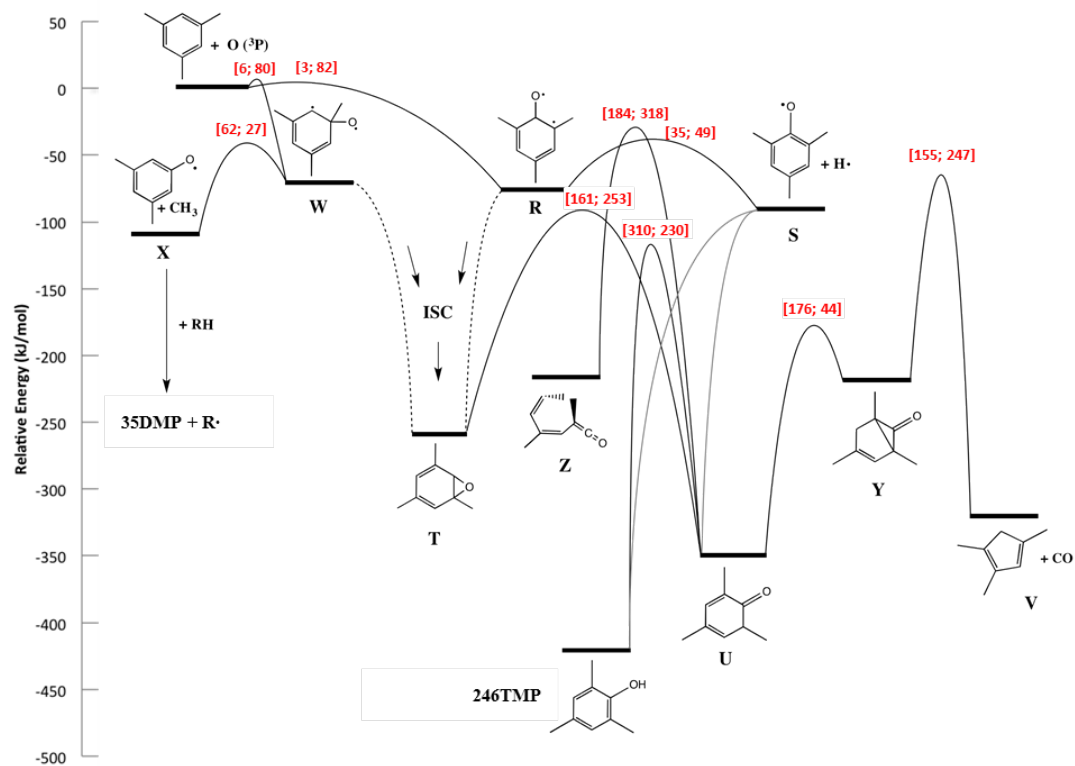
**Figure 4-4.** Experimental photoionization spectrum of  $m/z = 136$  product (red open circles) of the MT + Cl + O<sub>2</sub> at room temperature compared to the summation (black line) of the simulated photoionization spectra of 3,5-dimethylbenzyl alcohol (35DMBA) (green line) and experimentally recorded spectrum of 2,4,6-trimethylphenol (246TMP).



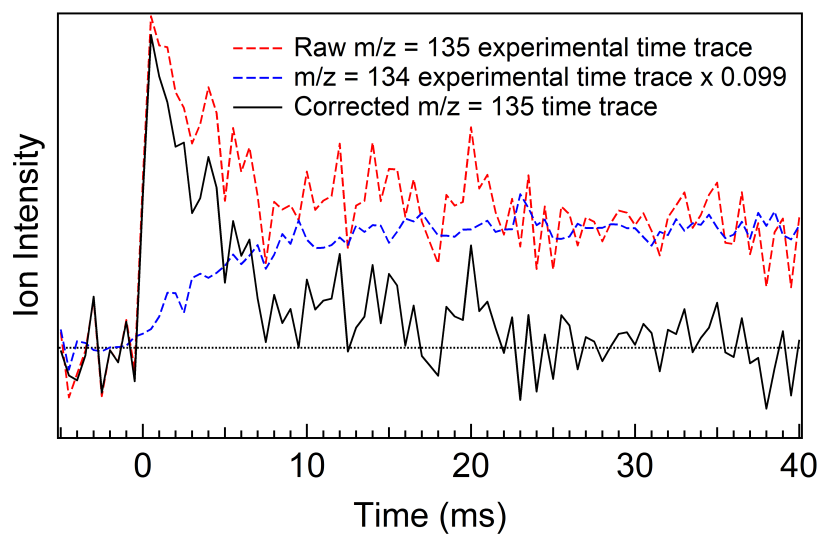
**Figure 4-5.** The measured photoionization spectrum of 3,5-dimethylbenzaldehyde (blue line) superimposed onto the experimental photoionization spectra of  $m/z = 134$  (open red circles) for the mesitylene + O (<sup>3</sup>P) reaction conducted at 823 K.



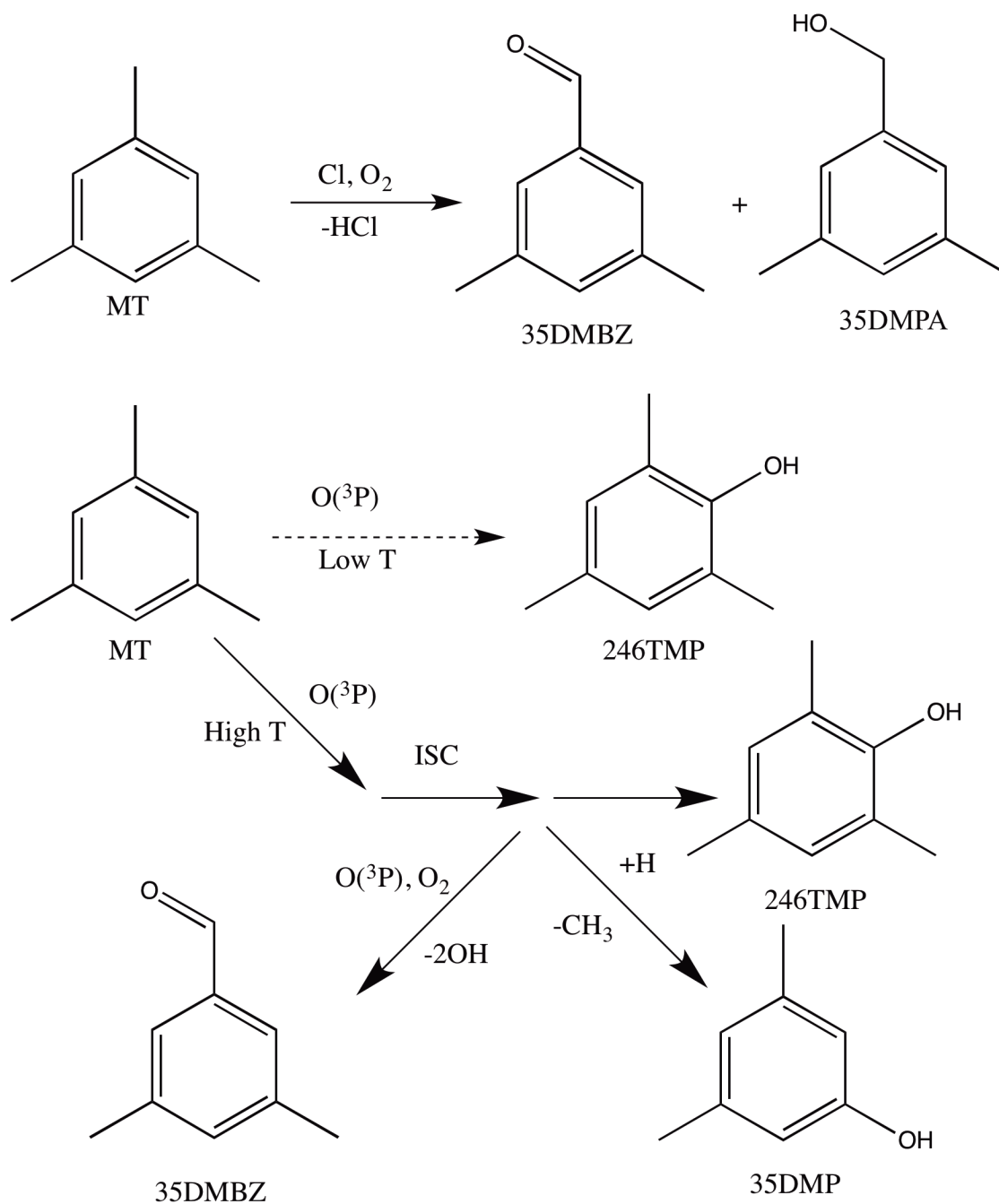
**Figure 4-6.** Measured photoionization spectrum of 246TMP (blue solid line) superimposed onto the  $m/z = 136$  experimental product spectrum (open red circles) from MT + O ( $^3P$ ) at 823 K.



**Figure 4-7.** Potential energy surface for the MT + O ( $^3\text{P}$ ) reaction calculated using the CBS-QB3 composite method. The numbers in square brackets represent the barrier heights with the left value corresponding to the left-to-the right reaction step and the right value corresponding to the opposite reaction.

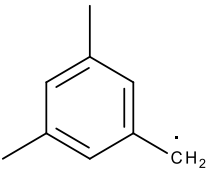
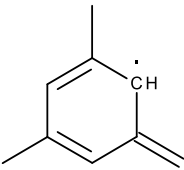
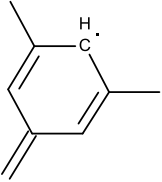
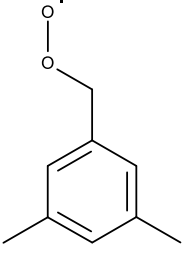
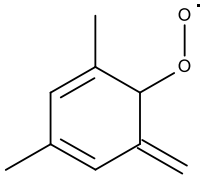


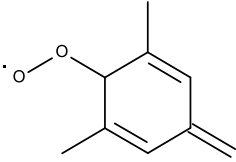
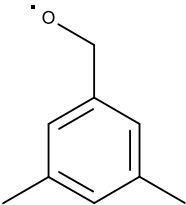
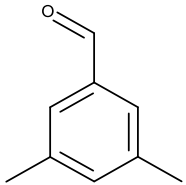
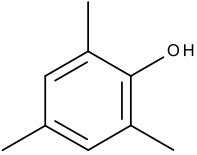
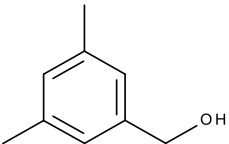
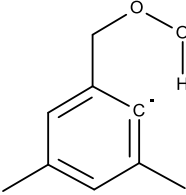
**Figure 4-8.** The experimental time trace of  $m/z = 135$  product of the  $\text{MT} + \text{O}$  reaction at 823 K (dotted red line) is corrected by the contribution of the  $^{13}\text{C}$  isotopologue of the  $m/z = 134$  product (blue line). The corrected time trace of the  $m/z = 135$  is shown as a black line.



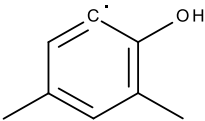
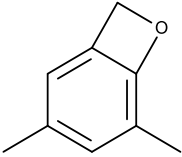
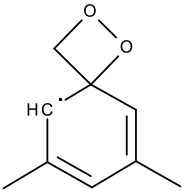
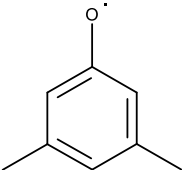
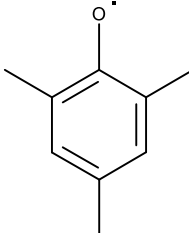
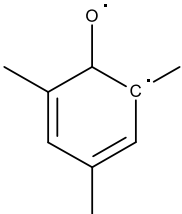
**Figure 4-9.** Simplified reaction schematic of the oxidation of mesitylene initiated by Cl atoms at room temperature and initiated by  $\text{O}(^3\text{P})$  at room temperature and 823 K.

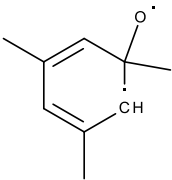
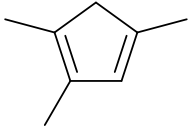
**Table 4-1.** List of relevant chemical species with their abbreviated names, calculated, and observed AIE values in eV.

Name	Structure	m/z	CBS-QB3 AIE (eV)	Observed AIE (eV)
(A1)		119	7.03	-
(A2)		119	7.60	-
(A3)		119	7.03	-
(B1)		151	-	-
(B2)		151	-	-

(B3)		151	-	-
mesitylenyloxy radical (C)		135	5.98	-
3,5-dimethylbenzaldehyde (35DMBZ)		134	8.95	8.85 ± 0.05
2,4,6-trimethylphenol (246TMP)		136	7.88	7.8 ± 0.1 <sup>a</sup>
3,5-dimethylbenzyl alcohol (35DMBA)		136	8.46	8.45 ± 0.05
(E)		151	6.95	-

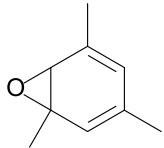
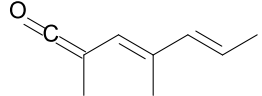
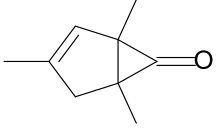


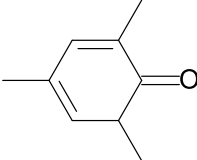
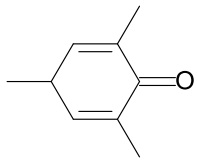
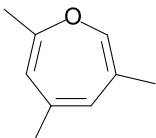
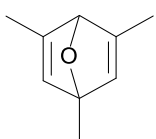
(F)		121	8.07	-
3,5-dimethyl-7-oxabicyclo[4.2.0]octa-1,3,5-triene (G)		134	7.91	-
(H)		151	7.52	-
3,5-dimethylbenzoxyl radical (I)		121	8.36	8.4 ± 0.1
2,4,6-trimethylbenzoxyl radical (S)		135	7.75	-
(R)		136	6.72	-

(W)		136	6.29	-
1,2,4-trimethylcyclopenta-1,3-diene (V)		108	7.58	-

<sup>a</sup>Measured from the MT + O (<sup>3</sup>P) reaction at room temperature.

**Table 4-2.** Other isomers of 2,4,6-trimethylphenol that are not observed as products of the MT + O reactions. The adiabatic ionization energies are calculated at the CBS-QB3 level.

Name	Structure	AIE (eV)
1,2-epoxy-1,3,5-trimethyl-3,5-cyclohexadiene (T)		8.20
2,4-dimethylhepta-1,3,5-trien-1-one (Z)		7.30
1,3,5-trimethylbicyclo[3.1.0]hex-2-en-6-one (Y)		7.23

2,4,6-trimethyl-2,4-cyclohexadien-1-one (U)		8.37
2,4,6-trimethyl-2,5-cyclohexadien-1-one		8.99
2,4,6-trimethyloxepine		8.02
2,5-epoxy-1,3,5-trimethyl-3,5-cyclohexadiene		8.46

**Table 4-3.** Branching yields of the reaction products in the mesitylene + Cl + O<sub>2</sub> reaction at room temperature and the mesitylene + O (<sup>3</sup>P) reaction at room temperature and 823 K.

Species	m/z	Types of product	BY (%) of MT + Cl + O <sub>2</sub> at 298 K	BY (%) of MT + O at 298 K	BY (%) of MT + O at 823 K
3,5-dimethylphenol	122.07	addition	-	-	16
3,5-dimethylbenzaldehyde	134.07	abstraction	24	-	46
2,4,6-trimethylphenol	136.09	addition	2	16	15
3,5-dimethylbenzyl alcohol	136.09	disproportionatation	1	-	-

#### 4.8 References

1. Adachi, K.; Freney, E. J.; Buseck, P. R., Shapes of Internally Mixed Hygroscopic Aerosol Particles after Deliquescence, and Their Effect on Light Scattering. *Geophys. Res. Lett.* **2011**, 38, L13804.
2. Houghton, J. T.; Ding, Y.; Griggs, D. J.; Noguera, M.; Linden, P. J. v. d.; Dai, X.; Maskell, K.; Johnson, C. A., *Climate Change 2001: The Scientific Basis*. Cambridge University Press: Cambridge, 2001.
3. Jacob, D. J., *Introduction to Atmospheric Chemistry*. Princeton University Press: Princeton, 1999.
4. Finlayson-Pitts, B. J.; James N. Pitts, J., *Chemistry of the Upper and Lower Atmosphere : Theory, Experiments, and Applications* Academic Press: San Diego, 2000.
5. Wyche, K. P., et al., Gas Phase Precursors to Anthropogenic Secondary Organic Aerosol: Detailed Observations of 1,3,5-Trimethylbenzene Photooxidation. *Atmos. Chem. Phys.* **2009**, 9, 635-665.
6. Stern, J. E.; Flagan, R. C.; Grosjean, D.; Seinfeld, J. H., Aerosol Formation and Growth in Atmospheric Aromatic Hydrocarbon Photooxidation. *Environ. Sci. Technol.* **1987**, 21, 1224-1231.
7. Odum, J. R.; Hoffmann, T.; Bowman, F.; Collins, D.; Flagan, R. C.; Seinfeld, J. H., Gas/Particle Partitioning and Secondary Organic Aerosol Yields. *Environ. Sci. Technol.* **1996**, 30, 2580-2585.
8. Kramp, F.; Paulson, S. E., On the Uncertainties in the Rate Coefficients for OH Reactions with Hydrocarbons, and the Rate Coefficients of the 1,3,5-Trimethylbenzene and m-Xylene Reactions with OH Radicals in the Gas Phase. *J. Phys. Chem. A* **1998**, 102, 2685-2690.
9. Calvert, J. G.; Atkinson, R.; Becker, K. H.; Kamens, R. M.; Seinfeld, J. H.; Wallington, T. J.; Yarwood, G., *The Mechanisms of Atmospheric Oxidation of Aromatic Hydrocarbons*; Oxford University Press: New York, 2002.
10. Fraser, M. P.; Cass, G. R.; Simoneit, B. R. T., Gas-Phase and Particle-Phase Organic Compounds Emitted from Motor Vehicle Traffic in a Los Angeles Roadway Tunnel. *Environ. Sci. Technol.* **1998**, 32, 2051-2060.
11. Nowak, L.; Guibert, P.; Cavadias, S.; Dupre, S.; Momié, J., Methodology Development of a Time-Resolved in-Cylinder Fuel Oxidation Analysis: Homogeneous Charge Compression Ignition Combustion Study Application. *Combust. Flame* **2008**, 154, 462-472.

12. Roubaud, A.; Minetti, R.; Sochet, L. R., Oxidation and Combustion of Low Alkylbenzenes at High Pressure: Comparative Reactivity and Auto-Ignition. *Combust. Flame* **2000**, 121, 535-541.
13. Moss, J. B.; Aksit, I. M., Modelling Soot Formation in a Laminar Diffusion Flame Burning a Surrogate Kerosene Fuel. *P Combust. Inst.* **2007**, 31, 3139-3146.
14. Mensch, A.; Santoro, R. J.; Litzinger, T. A.; Lee, S. Y., Sooting Characteristics of Surrogates for Jet Fuels. *Combust. Flame* **2010**, 157, 1097-1105.
15. Silva, G. d.; Bozzelli, J. W., On the Reactivity of Methylbenzenes. *Combust. Flame* **2010**, 157, 2175-2183.
16. Atkinson, R.; Arey, J., Atmospheric Degradation of Volatile Organic Compounds. *Chem. Rev.* **2003**, 103, 4605-4638.
17. Griffiths, J. F.; Hughes, K. J.; Porter, R., The Role and Rate of Hydrogen Peroxide Decomposition During Hydrocarbon Two-Stage Autoignition. *P. Combust. Inst.* **2005**, 30, 1083-1091.
18. He, X.; Zigler, B. T.; Walton, S. M.; Wooldridge, M. S.; Atreya, A., A Rapid Compression Facility Study of Oh Time Histories During Iso-Octane Ignition. *Combust. Flame* **2006**, 145, 552-570.
19. Du, H.; Hessler, J. P., Rate Coefficient for the Reaction  $H+O_2 \rightarrow OH+O$ : Results at High Temperatures, 2000 to 5300 K; *AIP*: 1992; Vol. 96, p 1077-1092.
20. Pack, R. T.; Butcher, E. A.; Parker, G. A., Accurate Quantum Probabilities and Threshold Behavior of the  $H + O_2$ . *J. Chem. Phys.* **1993**, 99, 9310-9313.
21. Aschmann, S. M.; Long, W. D.; Atkinson, R., Temperature-Dependent Rate Constants for the Gas-Phase Reactions of OH Radicals with 1,3,5-Trimethylbenzene, Triethyl Phosphate, and a Series of Alkylphosphonates. *J. Phys. Chem. A* **2006**, 110, 7393-7400.
22. Cvetanović, R. J., Evaluated Chemical Kinetic Data for the Reactions of Atomic Oxygen  $O(^3P)$  with Unsaturated Hydrocarbons. *Journal of Physical and Chemical Reference Data* **1987**, 16, 261-326.
23. Atkinson, R.; Pitts, J. N., Absolute Rate Constants for the Reaction of  $O(^3P)$  Atoms with Selected Alkanes, Alkenes, and Aromatics as Determined by a Modulation Technique. *The Journal of Physical Chemistry* **1974**, 78, 1780-1784.
24. Atkinson, R.; Pitts, J. N., Temperature Dependence of the Absolute Rate Constants for the Reaction of Oxygen( $^3P$ ) Atoms with a Series of Aromatic Hydrocarbons over the Range 299-392.Deg.K. *The Journal of Physical Chemistry* **1975**, 79, 295-297.

25. Holes, A.; Eusebi, A.; Grosjean, D.; Allen, D. T., Ftir Analysis of Aerosol Formed in the Photooxidation of 1,3,5-Trimethylbenzene. *Aerosol Sci. Tech.* **1997**, *26*, 516-526.
26. Smith, D. F.; Kleindienst, T. E.; McIver, C. D., Primary Product Distributions from the Reaction of Oh with M-, P-Xylene, 1,2,4- and 1,3,5-Trimethylbenzene. *J. Atmos. Chem.* **1999**, *34*, 339-364.
27. Bloss, C.; Wagner, V.; Bonzanini, A.; Jenkin, M. E.; Wirtz, K.; Martin-Reviejo, M.; Pilling, M. J., Evaluation of Detailed Aromatic Mechanisms (MCMv3 and MCMv3.1) against Environmental Chamber Data. *Atmos. Chem. Phys.* **2005**, *5*, 623-639.
28. Bloss, C., et al., Development of a Detailed Chemical Mechanism (MCMv3.1) for the Atmospheric Oxidation of Aromatic Hydrocarbons.Pdf. *Atmos. Chem. Phys.* **2005**, *5*, 641-664.
29. Rickard, A. R.; Wyche, K. P.; Metzger, A.; Monks, P. S.; Ellis, A. M.; Dommen, J.; Baltensperger, U.; Jenkin, M. E.; Pilling, M. J., Gas Phase Precursors to Anthropogenic Secondary Organic Aerosol: Using the Master Chemical Mechanism to Probe Detailed Observations of 1,3,5-Trimethylbenzene Photo-Oxidation. *Atmos. Environ.* **2010**, *44*, 5423-5433.
30. Sloane, T. M., Reaction Product Identification from O(<sup>3</sup>P) + Benzene, Toluene, and 1,3,5-Trimethylbenzene Collisions in Crossed Molecular Beams. *J. Chem. Phys.* **1977**, *67*, 2267-2274
31. Parker, J. K.; Davis, S. R., Photochemical Reactions of Oxygen Atoms with Toluene, M-Xylene, P-Xylene, and Mesitylene: An Infrared Matrix Isolation Investigation. *J. Phys. Chem. A* **2000**, *104*, 4108-4114.
32. Osborn, D. L., et al., The Multiplexed Chemical Kinetic Photoionization Mass Spectrometer: A New Approach to Isomer-Resolved Chemical Kinetics. *Rev. Sci. Instrum.* **2008**, *79*, 104103.
33. Taatjes, C. A.; Hansen, N.; Osborn, D. L.; Kohse-Hoinghaus, K.; Cool, T. A.; Westmoreland, P. R., "Imaging" Combustion Chemistry Via Multiplexed Synchrotron-Photoionization Mass Spectrometry. *Phys. Chem. Chem. Phys* **2008**, *10*, 20-34.
34. Taatjes, C. A.; Osborn, D. L.; Selby, T. M.; Meloni, G.; Fan, H.; Pratt, S. T., Absolute Photoionization Cross-Section of the Methyl Radical. *J. Phys. Chem. A* **2008**, *112*, 9336-9343.
35. Meloni, G.; Selby, T. M.; Osborn, D. L.; Taatjes, C. A., Enol Formation and Ring-Opening in OH-Initiated Oxidation of Cycloalkenes. *J. Phys. Chem. A* **2008**, *112*, 13444-13451.

36. Troe, J., Are Primary Quantum Yields of NO<sub>2</sub> Photolysis at  $\lambda \leq 398$  nm Smaller Than Unity? *Z. Phys. Chem.* **2000**, 214, 573-581.
37. Vandaele, A. C.; Hermans, C.; Simon, P. C.; Carleer, M.; Colin, R.; Fally, S.; Mérienne, M. F.; Jenouvrier, A.; Coquart, B., Measurements of the NO<sub>2</sub> Absorption Cross-Section from 42000 cm<sup>-1</sup> to 10000 cm<sup>-1</sup> (238-1000 nm) at 220 K and 294 K. *J. Quant. Spectrosc. Ra.* **1998**, 59, 171-184.
38. Iupac Subcommittee on Gas Kinetic Data Evaluation – Data Sheet Pcl11. <http://iupac.pole-ether.fr/>.
39. Maric, D.; Burrows, J. P.; Meller, R.; Moortgat, G. K., A Study of the UV-Visible Absorption Spectrum of Molecular Chlorine. *J. Photoch. Photobio. A* **1993**, 70, 205-214.
40. Person, J. C.; Nicole, P. P., Isotope Effects in the Photoionization Yields and the Absorption Cross Sections for Acetylene, Propyne, and Propene. *J. Chem. Phys.* **1970**, 53, 1767-1774.
41. Zhou, Z.; Xie, M.; Wang, Z.; Qi, F., Determination of Absolute Photoionization Cross-Sections of Aromatics and Aromatic Derivatives. *Rapid Commu. Mass Sp.* **2009**, 23, 3994-4002.
42. Kanno, N.; Tonokura, K., Vacuum Ultraviolet Photoionization Mass Spectra and Crosssections for Volatile Organic Compounds at 10.5 Ev. *Appl. Spectrosc.* **2007**, 61, 896-902.
43. Bobeldijk, M.; Zande, W. J. v. d.; Kistemaker, P. G., Simple Models for the Calculation of Photoionization and Electron Impact Ionization Cross Sectionso F Polyatomic Molecules. *Chem. Phys.* **1994**, 179, 125-130.
44. Montgomery, J. A., Jr.; Frisch, M. J.; Ochterski, J. W.; Petersson, G. A., A Complete Basis Set Model Chemistry. VI. Use of Density Functional Geometries and Frequencies. *J. Chem. Phys.* **1999**, 110, 2822-2827.
45. Montgomery, J. A., Jr.; Frisch, M. J.; Ochterski, J. W.; Petersson, G. A., A Complete Basis Set Model Chemistry. VII. Use of the Minimum Population Localization Method. *J. Chem. Phys.* **2000**, 112, 6532-6542.
46. Frisch, M. J. e. a. Gaussian 09, Revision A.1; Wallingford, 2009.
47. Taatjes, C. A., et al., Products of the Benzene + O(<sup>3</sup>P) Reaction. *J. Phys. Chem. A* **2010**, 114, 3355-3370.
48. Ervin, K. M., *Pascal, Fortran Program*; 2010.
49. Ervin, K. M.; Ho, J.; Lineberger, W. C., Ultraviolet Photoelectron Spectrum of Nitrite Anion. *J. Phys. Chem-US* **1988**, 92, 5405-5412.

50. Duschinsky, F., *Physicochim. URSS* **1937**, 7, 551.
51. Sharp, T. E.; Rosenstock, H. M., Franck—Condon Factors for Polyatomic Molecules. *J. Chem. Phys.* **1964**, 41, 3453.
52. Ervin, K. M.; Ramond, T. M.; Davico, G. E.; Schwartz, R. L.; Casey, S. M.; Lineberger, W. C., Naphthyl Radical: Negative Ion Photoelectron Spectroscopy, Franck–Condon Simulation, and Thermochemistry. *J. Phys. Chem. A* **2001**, 105, 10822-10831.
53. Wang, L.; Arey, J.; Atkinson, R., Reactions of Chlorine Atoms with a Series of Aromatic Hydrocarbons. *Environmental Science & Technology* **2005**, 39, 5302-5310.
54. Zádor, J.; Taatjes, C. A.; Fernandes, R. X., Kinetics of Elementary Reactions in Low-Temperature Autoignition Chemistry. *Prog. Energ. Combust.* **2011**, 37, 371-421.
55. Murakami, Y.; Oguchi, T.; Hashimoto, K.; Nosaka, Y., Theoretical Study of the Benzyl + O<sub>2</sub> Reaction: Kinetics, Mechanism, and Product Branching Ratios. *J. Phys. Chem. A* **2007**, 111, 13200-13208.
56. Murakami, Y.; Oguchi, T.; Hashimoto, K.; Nosaka, Y., Density Functional Study of the High-Temperature Oxidation of O-, M- and P-Xylyl Radicals. *J. Phys. Chem. A* **2009**, 113, 10652-10666.
57. Chen, C.-J.; Bozzelli, J. W., Thermochemical Property, Pathway and Kinetic Analysis on the Reactions of Allylic Isobutenyl Radical with O<sub>2</sub>: An Elementary Reaction Mechanism for Isobutene Oxidation. *The Journal of Physical Chemistry A* **2000**, 104, 9715-9732.
58. Zheng, X. L.; Sun, H. Y.; Law, C. K., Thermochemical and Kinetic Analyses on Oxidation of Isobutenyl Radical and 2-Hydroperoxymethyl-2-Propenyl Radical. *J. Phys. Chem. A* **2005**, 109, 9044-9053.
59. Dibble, T. S., Failures and Limitations of Quantum Chemistry for Two Key Problems in the Atmospheric Chemistry of Peroxy Radicals. *Atmos. Environ.* **2008**, 42, 5837-5848.
60. Ghigo, G.; Maranzana, A.; Tonachini, G., Combustion and Atmospheric Oxidation of Hydrocarbons: Theoretical Study of the Methyl Peroxyl Self-Reaction. *J. Chem. Phys.* **2003**, 118, 10575.
61. Clothier, P. Q. E.; Shen, D.; Pritchard, H. O., Stimulation of Diesel-Fuel Ignition by Benzyl Radicals. *Combustion and Flame* **1995**, 101, 383-386.
62. Cetinkaya, B.; Lappert, M. F.; Suffolk, R. J., Photoelectron Spectra of Some Sterically Hindered Phenols and Related Compounds. *J. Chem. Res. Synop* **1983**, 316.



63. Zhang, W.; Du, B.; Feng, C., An Ab Initio Dynamics Study on the Reaction of  $O(^3P)$  with  $CH_3CHCH_2$  (1a'). *J. Mol. Struct-Theochem* **2007**, 806, 121-129.
64. Tsang, W., Chemical Kinetic Data Base for Combustion Chemistry Part V. Propene. *J. Phys. Chem. Ref. Data* **1991**, 20, 221-273.
65. Min, Z.; Wong, T.-H.; Su, H.; Bersohn, R., Reaction of  $O(^3P)$  with Alkenes: Side Chain Vs Double Bond Attack. *J. Phys. Chem. A* **2000**, 104, 9941-9943.
66. Nguyen, T. L.; Peeters, J.; Vereecken, L., Theoretical Reinvestigation of the  $O(^3P) + C_6H_6$  Reaction: Quantum Chemical and Statistical Rate Calculations. *J. Phys. Chem. A* **2007**, 111, 3836.
67. Barckholtz, T. A.; Joshi, A.; Wang, H., In In 4<sup>th</sup> Joint Meeting of the U.S. Sections of the Combustion Institute, Drexel University: Philadelphia, PA, 2005.
68. Berkowitz, J.; Ellison, G. B.; Gutman, D., Three Methods to Measure RH Bond Energies. *J. Phys. Chem.* **1994**, 98, 2744-2765.

## Chapter 4S - Supporting Information for Chapter 4

### 4S.1 Supporting Material

#### 4S.1.1 Photoionization of 3,5-Dimethylbenzaldehyde

The measured AE of  $m/z = 133$  daughter ion is  $10.12 \pm 0.05$  eV. This value is related to the neutral aldehydic C-H bond energy in 35DMBZ and the AIE of the 35DMBZ radical via the expression

$$\text{AE}(35\text{DMBZ}^{\cdot+}, 35\text{DMBZ-H}) = D_0^{\circ}(35\text{DMBZ-H}) + \text{AIE}(35\text{DMBZ}^{\cdot}) \quad (4\text{S.1})$$

The CBS-QB3 calculated  $\text{AIE}(35\text{DMBZ}^{\cdot})$  is 5.98 eV, which yields an energy of 399 kJ mol<sup>-1</sup> (4.14 eV) for the aldehydic C-H bond at 0 K. This value can be converted to 298 K using the heat content functions ( $H_{298}^{\circ} - H_0^{\circ}$ ) of 35DMBZ<sup>·</sup>, H, and 35DMBZ.  $D_{298}^{\circ}(35\text{DMBZ-H})$  is then calculated to be  $409 \pm 10$  kJ mol<sup>-1</sup>, which is higher than the literature value of  $371.1 \pm 10.9$  kJ mol<sup>-1</sup> (Ref. <sup>1</sup>) for the unsubstituted benzaldehyde. The CBS-QB3 calculation for the neutral aldehydic C-H bond energy of 409 kJ mol<sup>-1</sup> matches the experimental result. From the  $\text{AE}(35\text{DMBZ}^{\cdot+}, 35\text{DMBZ-H})$  and AIE of 35DMBZ values it is also possible to derive the aldehydic C-H bond energy in 35DMBZ<sup>+</sup> by simply subtracting  $\text{AIE}(35\text{DMBZ}^{\cdot})$  to  $\text{AE}(35\text{DMBZ}^{\cdot+}, 35\text{DMBZ-H})$ . The  $D_0^{\circ}(35\text{DMBZ-H}^{\cdot+})$  is thus 122.5 kJ mol<sup>-1</sup> ( $127 \pm 10$  kJ mol<sup>-1</sup> at 298 K), in good agreement with the CBS-QB3 value of 120 kJ mol<sup>-1</sup>.

#### 4S.1.2 Identification of Secondary Products

When analyzing the experimental photoionization spectrum of  $m/z = 108$ , there are two possible products contributing to this spectrum, one of which is 1,2,4-trimethylcyclopenta-1,3-diene (V). However, its calculated CBS-QB3 AIE is 7.59 eV, well below the lowest photon energy (8.02 eV) measured in the present investigation. Even so, the intensity of the experimental  $m/z = 108$  photoionization spectrum, after correcting for the contribution of  $m/z = 108$  dissociative ionization fragment of 35DMP, is non-zero at 8.02 eV. The lower energy part of  $m/z = 108$  experimental spectrum from 8.02 to 8.5 eV is matched to the simulated photoionization spectrum of 1,2,4-trimethylcyclopenta-1,3-diene (Figure 4S-1). The rest of the corrected experimental photoionization spectrum can be fit by m-cresol or 3-methylphenol. The CBS-QB3 AIE of m-cresol is 8.37 eV, which is in good agreement with literature values recorded by Kobayashi (8.52 eV)<sup>2</sup> and Palmer (8.41 eV)<sup>3</sup> using photoelectron spectroscopy techniques. However, the onsets of the integrated photoelectron spectra measured by Kobayashi<sup>2</sup> and Palmer<sup>3</sup> are at 8.20 and 8.25 eV, respectively. There is a sizable discrepancy between the onsets of the integrated PE spectra and the reported ionization energies, whereas the calculated CBS-QB3 AIE is more in agreement with the reported IEs; therefore, the simulated spectrum of m-cresol is used in the analysis of the  $m/z = 108$  experimental photoionization spectrum. The summation of the simulated spectra of 1,2,4-trimethylcyclopenta-1,3-diene and m-cresol is in very good agreement with  $m/z = 108$  product data corrected by the contribution of  $m/z = 108$  dissociative ionization fragment of 35DMP (Figure 4S-1). When the time traces of  $m/z = 108$  and 122 products are compared (Figure 4S-2), it is possible to observe that the production of  $m/z = 108$  is slower than that of  $m/z =$

122. Because the intensity of the experimental photoionization spectrum is mainly due to m-cresol contribution, it is concluded that m-cresol is a secondary product formed from reactions of 3,5-dimethylphenol.

Another minor product is detected at  $m/z = 106$ , assigned as m-xylene. As shown in Figure 4S-3, the literature photoionization spectrum of m-xylene recorded by Zhou et al.<sup>4</sup> matches very well the experimental spectrum of  $m/z = 106$  product. The observed onset of the  $m/z = 106$  is 8.50 eV, which is in good agreement with the literature ionization energy of  $8.55 \pm 0.03$  eV.<sup>4</sup> The branching yields of both m-cresol and m-xylene are small.

#### 4S.2 Supplemental Figures

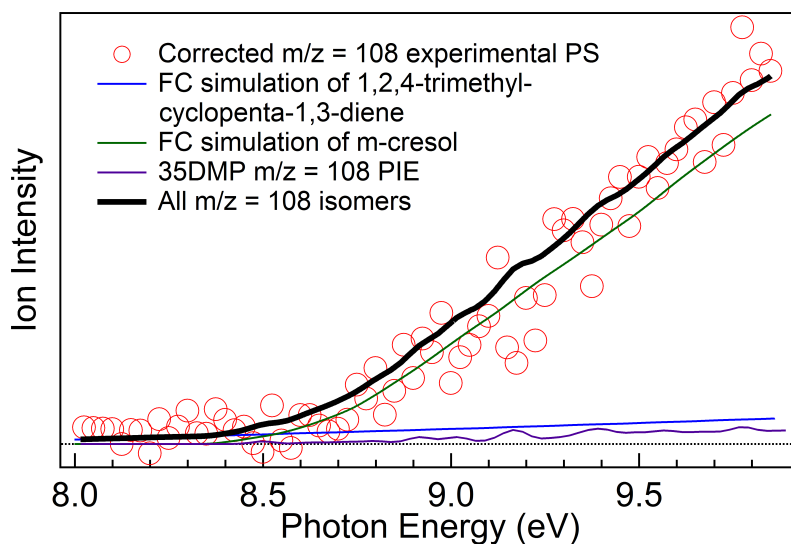


**Figure 4S-1.** The simulated photoionization spectra of 1,2,4-trimethylcyclopenta-1,3-diene (blue line), m-cresol (green line) and the authentic PIE of  $m/z = 108$  of 35DMP (purple line) are superimposed onto the experimental photoionization spectrum (red open circles) of  $m/z = 108$  product.

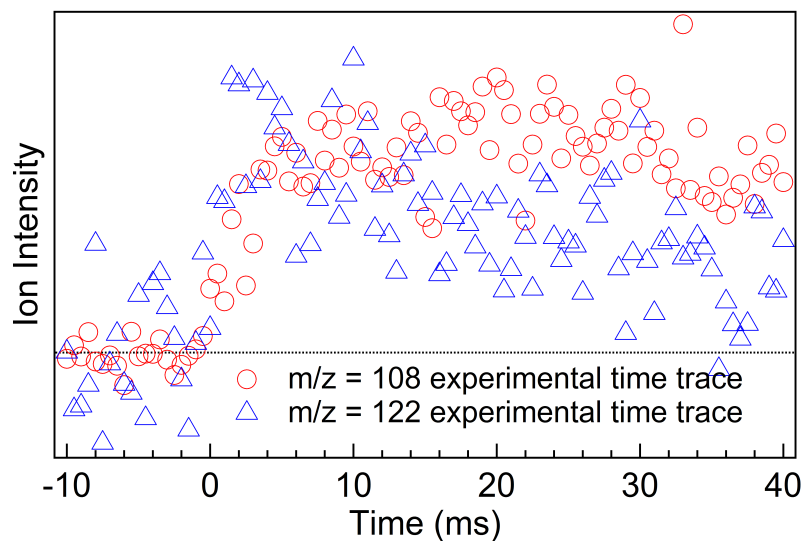


**Figure 4S-2.** The comparison of the time traces of  $m/z = 108$  (red line) and  $122$  (blue line) products.

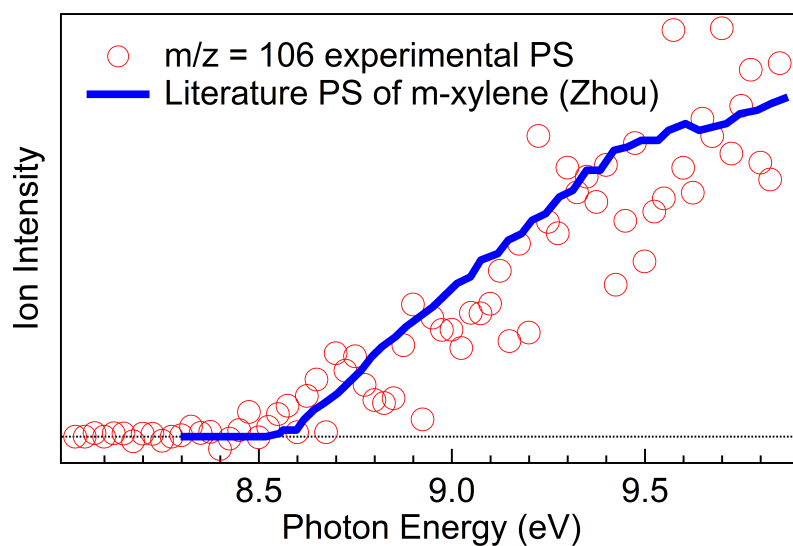


**Figure 4S-3.** The literature photoionization spectrum of *m*-xylene (blue line) by Zhou and co-workers<sup>4</sup> and the experimental spectrum of  $m/z = 106$  (open red circles) in the MT + O reaction at 823 K.

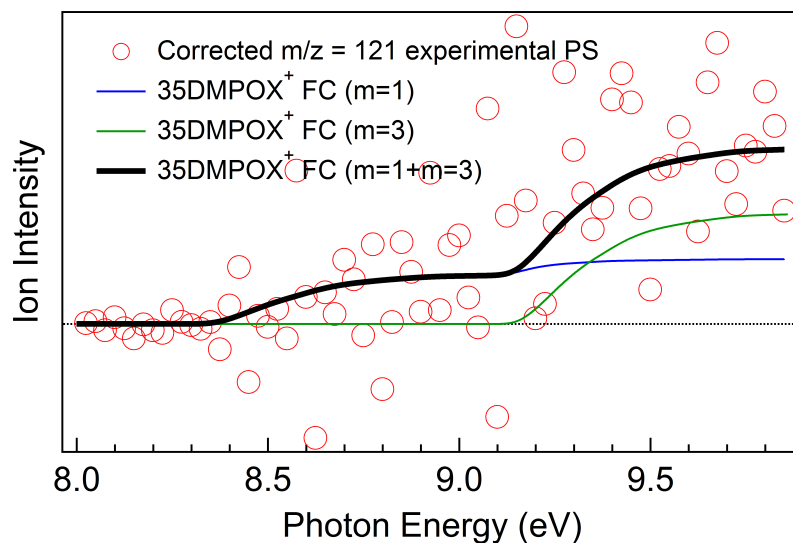


**Figure 4S-4.** The Franck-Condon simulation of 3,5-dimethylphenoxy (35DMPOX) radical (black line) is in agreement with the  $^{13}\text{C}$  isotopologue-corrected experimental photoionization spectrum (open red circles) of  $m/z = 121$  in the MT + O reaction at 823 K.

#### 4S.3 References

1. Luo, Y. R., Comprehensive Handbook of Chemical Bond Energies. CRC Press: Boca Raton, FL, 2007.
2. Kobayashi, T.; Nagakura, S., Photoelectron Spectra of Substituted Benzenes. Bull. Chem. Soc. Jpn. **1974**, 47, 2563-2572.
3. Palmer, M. H.; Moyes, W.; Speirs, M.; Ridyard, J. N. A., The Electronic Structure of Substituted Benzenes; Ab Initio Calculations and Photoelectron Spectra for Phenol, the Methyl- and Fluoro-Derivatives, and the Dihydroxybenzenes. J. Mol. Struct. **1979**, 52, 293-307.
4. Zhou, Z.; Xie, M.; Wang, Z.; Qi, F., Determination of Absolute Photoionization Cross-Sections of Aromatics and Aromatic Derivatives. Rapid Comm. Mass Spectrom. **2009**, 23, 3994-4002.

## **Chapter 5 - The Study of Tert-Amyl Methyl Ether Low Temperature Oxidation Using Synchrotron Photoionization Mass Spectrometry**

(This chapter was co-authored with Brittany M. Bryan, Jordan Nelson and Giovanni Meloni, and it was submitted to the Journal of Physical Chemistry A for peer-review.)

### **5.1 Abstract**

This paper examines the oxidation reaction of tert-amyl methyl ether (TAME), an oxygenated fuel additive, with chlorine radical initiators in the presence of oxygen. Data is collected at 293, 550, and 700 K. Reaction intermediates and products are probed by a multiplexed chemical kinetics synchrotron photoionization mass spectrometer (SPIMS), and characterized based on mass-to-charge ratio, ionization energy, and photoionization spectra. Reaction schematics are proposed to validate detected primary products.

### **5.2 Introduction**

The purpose of blending fuel additives into gasoline is not only to enhance fuel efficiency, but most importantly to lessen toxic combustion exhaust like particular matter (PM).<sup>1</sup> Reduction of toxic emissions is imperative. PM, which includes aromatic compounds, may cause serious health problems in humans attributed to their carcinogenicity.<sup>2-3</sup> Oxygenated hydrocarbons increase oxygen content of fuels while decreasing toxic emission.<sup>1</sup> Since oxygenated additives have favorable combustion properties, the Clean Air Act (CAA) amendments of 1990 require that oxygenated gasoline be used in areas where air pollution levels are highest.<sup>4</sup> From the time of implementation of the CAA amendments in 1992 until 2004, the most

popular ether oxygenated fuel additive had been methyl tert-butyl ether (MTBE).<sup>5</sup> Unfortunately, MTBE has a high water solubility<sup>6</sup> and is detected in drinking water, which is usually drawn from an underground source.<sup>5-8</sup> California and New York along with 17 other states in the United States have either prohibited or limited the addition of MTBE in gasoline.<sup>9</sup> Tert-amyl methyl ether (TAME) is currently being utilized as an alternative to MTBE.

TAME is produced from methanol and 2-methyl-1-butene (2M1B) or 2-methyl-2-butene (2M2B).<sup>10</sup> Goldaniga *et al.*<sup>11</sup> have studied the combustion of TAME using high-pressure jet-stirred reactor (at 800–1150 K and 10 atm) and concluded that the major product is isoamylene (or 2-methyl-2-butene). Isoprene, isobutene, methylacrolein, propene, acetone, and formaldehyde are also identified as secondary or even tertiary products. In comparison to MTBE, TAME has a similar octane number and a lower Reid vapor pressure,<sup>10, 12</sup> indicating that TAME escapes to the environment less readily in the gas phase. Nevertheless, there is concern about the extent of TAME evaporating into the atmosphere. In order to assess this risk, the atmospheric reaction of OH with TAME has been investigated. Wallington *et al.*<sup>13</sup> reported the rate constant of the TAME + OH reaction as  $(6.32 \pm 0.72) \times 10^{-12} \exp[(-40 \pm 70)/T] \text{ cm}^3 \text{ molecule}^{-1} \text{ s}^{-1}$  in the 240–400 K temperature range using flash photolysis resonance fluorescence and Teflon bag-GC FID techniques. In a similar study, Smith and co-workers<sup>14</sup> concluded that the rate constant of the atmospheric degradation of TAME by OH was  $5.48 \times 10^{-12} \text{ cm}^3 \text{ molecule}^{-1} \text{ s}^{-1}$  at  $298 \text{ K} \pm 2 \text{ K}$  using GC/FTIR/MS methods. Tert-amyl formate, methyl acetate, acetaldehyde, formaldehyde, acetone, 3-methoxy-3-methylbutyraldehyde, t-amyl alcohol have been identified as products. The TAME + OH rate constant was also reported by Teton<sup>15</sup>



as  $k = (4.7 \pm 0.7) \times 10^{-12} \exp[(82 \pm 85)/T]$  in the 230–372 K temperature range using a pulsed laser photolysis-laser induced fluorescence (PLP-LIF) technique.

Although each study was conducted below combustion temperatures, valuable information about the reactivity of TAME was collected. This work will focus on the characterization of products for the Cl-initiated oxidation reactions of TAME in the presence of O<sub>2</sub> at 298, 550, and 700 K.

### 5.3 Experiment

In order to study the TAME + Cl + O<sub>2</sub> reactions, a synchrotron multiplexed time- and energy-resolved photoionization mass spectrometer (SPIMS) is used to probe oxidation intermediates and products. Experiments are carried out at the Advanced Light Source (ALS) located at the Lawrence Berkeley National Laboratory. The experimental apparatus is described elsewhere.<sup>16-19</sup> The reactions are initiated in a 62-cm long slow-flow quartz reaction tube with an inner diameter of 1.05 cm. TAME (97.0 %, Sigma Aldrich) is prepared in a gas cylinder at about a 1.1 % concentration in an excess of helium. All gaseous reactants, TAME, Cl<sub>2</sub>, and O<sub>2</sub> are directed into the reaction tube and regulated by calibrated mass flow controllers. A 18 μm thick nichrome heating tape wraps around the reactor so that temperature can be adjusted. The pressure inside the reaction tube is maintained at 4 Torr at 298 K and 7.51 Torr at 550 and 700 K by a Roots pump through a feed-back controlled throttle valve. The gas mixture is photolyzed by a 4 Hz-pulsed unfocused 351 nm (XeF) excimer laser. The number density ranges for TAME, Cl<sub>2</sub>, and O<sub>2</sub> are  $4 \times 10^{13}$ – $1 \times 10^{14}$ ,  $7 \times 10^{14}$ – $1 \times 10^{15}$ , and  $1$ – $2 \times 10^{16}$  molecules cm<sup>-3</sup>, respectively.

The photolysis of Cl<sub>2</sub> yields two chlorine atoms according to the following reaction:



IUPAC Subcommittee for Gas Kinetic Data Evaluation recommended 1.00 as the quantum yield of the Cl<sub>2</sub> photolysis,<sup>20</sup> while the absorption cross section at 351 nm is 1.82 x 10<sup>-19</sup> cm<sup>2</sup> according to Maric *et al.*<sup>21</sup> Based on these two values, the number density for Cl atoms during current experiments is 6–8 x 10<sup>12</sup> molecules cm<sup>-3</sup>, which gives a concentration of TAME about 7–13 times the concentration of chlorine radicals. 2-Methyl-1-butene (Fluka, ≥ 99.5 %), 2-methyl-2-butene (Sigma-Aldrich, ≥ 99 %), and 2-methoxypropene (Santa Cruz Biotechnology, ≥ 95 %) are possible reaction products, so their absolute photoionization spectra are recorded for data analysis. Absolute photoionization spectra are obtained by comparing the signals of a known concentration of the gaseous compound of interest with the calibration gas mixture containing ethene, propene, and 1-butene without photolysis at a chosen temperature.

The reaction mixture effuses continuously through a 650 μm-wide orifice on the side of the reactor. It is then skimmed into the differentially vacuumed ionization region where the quasi-continuous tunable vacuum ultraviolet synchrotron radiation photoionizes the gaseous species. Ions are accelerated towards and detected by an orthogonal time-of-flight (TOF) mass spectrometer pulsed at 50 kHz. The mass resolution is approximately 1600 with the current settings.

Mass spectra plots of ion intensity ( $I$ ) versus mass-to-charge ratio ( $m/z$ ) are recorded in steps of 20  $\mu\text{s}$  starting 20 ms before photolysis for a total of 150 ms. The time-resolved mass spectra are scanned across the photon energy ( $E$ ) 8–11.2 eV range at increments of 25 meV. At each photon energy step, the pre-photolysis signal is background subtracted from the ion signal and then the ion signal is normalized by the ALS photon current. Ion intensity can be integrated over a selected photon energy range to produce a kinetic plot of a selected  $m/z$ . Time equal to 0 ms represents when the excimer laser is fired and, therefore, corresponds to  $t_0$  of the reaction. By the same method, the ion signal of a specific  $m/z$  can be integrated over a selected time interval to yield a photoionization spectrum. Comparison of experimental photoionization spectra to literature, measured, or calculated spectra, can identify reaction species. The adiabatic ionization energy of a species is determined by a linear extrapolation of the initial onset of the photoionization spectrum as detailed elsewhere.<sup>22</sup> Each photoionization spectrum is specific due to the ionization threshold, geometries, and vibrational modes (which translate into the Franck-Condon (FC) factors) of each species involved. Based on the photon energy step size, the possible presence of hot bands, and energy resolution, the uncertainty for reported adiabatic ionization energies is estimated to be 0.05 eV.

Photoionization spectra not only assist in product identification, but also provide information relating to the relative concentrations of products of interest. Photoionization spectra intensity at a specific photon energy ( $S_E$ ) relates to the concentration ( $C$ ) of a species via the following relationship:

$$S_E = k\sigma_E\delta C \quad (5.1)$$

where  $k$  represents the instrument constant,  $\sigma_E$  and  $S_E$  are the photoionization cross-section and ion signal at a specific photon energy, respectively.  $\delta$  is the mass-discrimination factor, which is approximately equal to the mass  $m$  of the observed species to the power of 0.67.<sup>23</sup> This factor takes into account the different sampling efficiency of the detector for different masses. When the photon energy is plotted against photoionization cross-section, the photoionization spectrum is referred to as the absolute photoionization spectrum or absolute PI curve. If the absolute PI plot of a species of interest is unknown, its authentic spectrum recorded from the pure chemical, is compared to an absolute photoionization spectrum of a reference species, such as ethene. The photoionization cross-section of TAME used in this work was measured during current experiments.

Once the absolute photoionization cross-section of a species of interest and the reactant are gathered using the method mentioned above, the branching fractions of products can simply be computed from the ratio of product concentration ( $C_P$ ) over reactant concentration ( $C_R$ ).

$$\frac{C_P}{C_R} = \frac{\frac{S_P}{\sigma_P\delta_P}}{\frac{S_R}{\sigma_R\delta_R}} = \frac{S_P\sigma_R\delta_R}{S_R\sigma_P\delta_P} = \frac{S_P\sigma_R}{S_R\sigma_P} \left(\frac{m_R}{m_P}\right)^{0.67} = \frac{S_P\sigma_R}{S_R\sigma_P} MDF \quad (5.2)$$

$MDF$  represents the mass discrimination factors ratio. Because both ion signal and photoionization cross-section are functions of photon energy, photoionization spectra are compared at the same photon energy, at which usually the spectra exhibit plateaus. The uncertainty of the branching fractions reported in this work is 20%.

## 5.4 Computational Methods

Optimized bond lengths, bond angles, harmonic vibrational frequencies, and force constants of the investigated species are calculated using the CBS-QB3 composite model<sup>24-25</sup> within the Gaussian 09 program.<sup>26</sup> The adiabatic ionization energies are calculated from the difference between zero-point vibrational (ZPE) corrected total electronic energies ( $E_0$ ) of the ground electronic states of the neutral and the cationic molecules. The appearance energy of a daughter ion from dissociative photoionization is calculated as follows:

$$AE(M^+, M-X) = D_0^0(M-X) + AIE(M) \quad (5.3)$$

This equation is used assuming the absence of a dissociation barrier for the parent ion. Enthalpies of reaction ( $\Delta_r H_0^0$ ) are calculated using ZPE corrected total electronic energies to demonstrate that proposed mechanisms are thermodynamically feasible or exothermic. In addition, ZPE corrected total electronic energies are employed in connection with available literature enthalpies of formation ( $\Delta_f H_0^0$  and  $\Delta_f H_{298}^0$ ) of the elements in the gas phase to derive the enthalpy of formation at 0 or 298 K of the reaction species, according to the atomization reaction  $C_x H_y O_z(g) \rightarrow xC(g) + yH(g) + zO(g)$ , where  $\Delta_{at} H_0^0 = xE_0(C) + yE_0(H) + zE_0(O) - E_0(C_x H_y O_z) = x\Delta_f H_0^0(C, g) + y\Delta_f H_0^0(H, g) + z\Delta_f H_0^0(O, g) - \Delta_f H_0^0(C_x H_y O_z, g)$ . Relaxed potential energy surface (PES) scans are carried out at the B3LYP/CBSB7 level. Saddle points (first-order transition states) and minima are then re-optimized using the CBS-QB3 composite model. Potential energy surface minima and saddle points are verified through intrinsic reaction coordinate calculations (forward/reverse). For the initiation reactions, i.e., TAME + Cl and the subsequent reactions between alkyloxyalkyl radicals and O<sub>2</sub>

(Scheme 5-1), the actual reaction enthalpy of each individual step is given in  $\text{kJ mol}^{-1}$ , whereas reaction enthalpies of the decomposition of the alkyloxyalkylperoxy radicals (Schemes 5-2 - 5-5) use alkyloxyalkylperoxy radicals as the zero (reference point).

To calculate a photoionization spectrum of a reaction species, Franck-Condon<sup>27-30</sup> and Franck-Condon-Herzberg-Teller methods<sup>27</sup> are used within the Gaussian 09 program. These methods generate a photoelectron (PE) spectrum through approximating Franck-Condon (FC) factors for the transition from the neutral to the cationic state of the molecule. The Duschinsky effect<sup>31</sup> is included in the calculation. The FC overlap integrals are computed using a set of recursive formulae developed by Ruhoff,<sup>32</sup> which are based on the Sharp-Rosenstock<sup>33</sup> and Lermé methods.<sup>34</sup> Integration of the calculated photoelectron spectrum yields a simulated photoionization spectrum.

## 5.5 Discussion and Analysis

Chlorine radicals initiate the oxidation of TAME through hydrogen abstraction. TAME is a saturated ether, making the addition of chlorine atoms to the molecule unlikely. Chlorinated species are formed during secondary reactions, such as addition to an unsaturated primary product. Chlorinated compounds are identified based on isotopic distribution for  $^{35}\text{Cl}$ - and  $^{37}\text{Cl}$ -containing species observed in identical photoionization spectra and time profiles. However, the fraction of chlorinated species is insignificant in the experiments performed at 550 and 700 K.

The following analysis is divided into three sections based on the experimental temperature of reaction. Identification and comparison of products at 298, 550, and 700 K is presented. The enthalpies of reaction for possible products

are calculated at the CBS-QB3 level at 0 K and reported to support characterization assignments. Branching fractions, the ratio between the concentration of a product and the initial concentration of the reactant, are calculated and reported to help identify major products and primary reaction mechanisms.

The reactant TAME has an unbound cation resulting in the absence of signal at  $m/z = 102$  (parent ion). Rather, the major dissociative fragment at  $m/z = 73$  is detected. This is in agreement with the study reported by Morton *et al.*<sup>35</sup> in which they only observed a major  $m/z = 73$  and a minor  $m/z = 87$  peak, but not  $m/z = 102$ , using ultraviolet photoionization time-of-flight mass spectrometry by radiating samples at  $\sim 10.5$  eV. It is assumed that TAME dissociatively ionizes completely such that the concentration of  $m/z = 73$  replaces the concentration of TAME. All values corresponding to the starting material are those from the  $m/z = 73$  signal.

#### 5.5.1 Product Identification of TAME + Cl + O<sub>2</sub> at 298 K

In the room temperature Cl initiated oxidation of TAME the following  $m/z$  are observed and characterized: 30, 42, 44, 56, 58, 72, and 86.

The experimental photoionization spectrum at  $m/z = 30$  matches very well with the literature photoionization spectrum of formaldehyde (Figure 5-1).<sup>36</sup> The onset of  $m/z = 42$  at about 10.45 eV as seen in Figure 5-2 is assigned to the daughter ion from the dissociative photoionization of 2,2-dimethyloxirane<sup>23</sup> ( $m/z = 72$ , C<sub>4</sub>H<sub>8</sub>O), whose identity will be discussed shortly. The  $m/z = 44$  product is assigned to acetaldehyde via comparison with the literature photoionization spectrum taken by Cool *et al.*,<sup>37</sup> as seen in Figure 5-3. The reported adiabatic ionization energy for acetaldehyde is 10.23 eV,<sup>37</sup> which matches the experimental onset of 10.20 eV. The

contributing product at  $m/z = 56$  is identified as 1-butene ( $C_4H_8$ ) with an onset at about 9.6 eV. The absolute cross section of 1-butene reported by Wang<sup>38</sup> fits the shape of the experimental PI plot despite the poor signal-to-noise ratio, as seen in Figure 5-4. The  $m/z = 30, 56, 58,$  and  $72$  products are formed at a comparable rate as it can be seen from the comparison of their time traces with that of the dissociative fragment of TAME at  $m/z = 73$  (Figure 5). The rate constants of forming the products just mentioned are  $379 \pm 85, 845 \pm 223, 298 \pm 36$  and  $415 \pm 163 \text{ s}^{-1}$ , respectively. The rate of decay of TAME is  $809 \pm 102 \text{ s}^{-1}$ . While the formation of  $m/z = 30$  is monophasic at room temperature, it is more complicated at 550 and 700K, which will be explained later.

Acetone and propanal (both with the formula  $C_3H_6O$ ) are assigned to the  $m/z = 58$  signal, as shown in Figure 5-6 from the good agreement. The first onset of the experimental spectrum is at 9.65 eV, while the literature ionization energy of acetone is  $9.703 \pm 0.006 \text{ eV}$ .<sup>39-41</sup> The calculated CBS-QB3 AIE of acetone is 9.74 eV. The second photon energy onset for  $m/z = 58$  is in good agreement with the authentic photoelectron spectrum of propanal<sup>38</sup> with an AIE of 9.96 eV. The initial experimental onset for  $m/z = 72$  at 8.56 eV matches satisfactorily with the authentic photoionization spectrum of 2-methoxy-1-propene ( $C_4H_8O$ ) taken during these current experiments. As shown in Figure 5-7, the curve fits the data well between 8.2 and 9.3 eV. The CBS-QB3 calculated AIE for 2-methoxy-1-propene is 8.58 eV, which is in agreement with the experimental data. The higher energy portion of the spectrum is matched by the photoionization curve of pure 2,2-dimethyloxirane, the presence of which is supported by the appearance of its daughter ion at  $m/z = 42$  from dissociative photoionization. The CBS-QB3 calculated AIE for 2,2-



dimethyloxirane is 9.56 eV, which is in good agreement with the experimental data. Summation of the 2-methoxy-1-propene and 2,2-dimethyloxirane absolute photoionization spectra fits the experimental data reasonably well.

Four compounds, 2-methoxy-2-butene, 2-methoxy-1-butene, 2,2-dimethyloxetane, and  $\gamma$ -butyrolactone (GBL) have been identified in contributing to the signal at  $m/z = 86$ . Three inflection points are observed at 8.6, 10, and 10.5 eV (Figure 5-8). The calculated values of AIE for 2-methoxy-2-butene, 2-methoxy-1-butene, 2,2-dimethyloxetane, and  $\gamma$ -butyrolactone are 7.91, 8.49, 9.3, and 10.13 eV, respectively. The photoionization spectra for 2-methoxy-2-butene, 2-methoxy-1-butene, and 2,2-dimethyloxetane are computed within the Franck-Condon approximation as described in the computational methods section, while the absolute photoionization energy curve of  $\gamma$ -butyrolactone is experimentally measured.<sup>42</sup> The summation of the four curves fits well the  $m/z = 86$  experimental spectrum.

### 5.5.2 Product Identification of TAME + Cl + O<sub>2</sub> at 550 K

Several species identified as the products of the reaction of TAME H-abstraction radical and oxygen at 550 K are the same as those characterized for the same reaction at room temperature. A few products seen at room temperature are not present at the higher temperature and new products have been identified as well. The differences in products are indication that the reaction pathway is temperature-dependent.

The literature photoionization spectrum of formaldehyde matches the experimental data at  $m/z = 30$  very well similarly to the results at room temperature.<sup>36</sup>

As seen at room temperature, the signal of  $m/z = 42$  is assigned to the daughter ion of the dissociative photoionization of 2,2-dimethyloxirane<sup>23</sup> ( $m/z = 72$ ,  $C_4H_8O$ ). At higher temperature the signal at  $m/z = 44$  is not present. The signal at  $m/z = 58$  is assigned to three species. The first onset at 9.68 eV is identified as acetone ( $C_3H_6O$ ). This is in good agreement with its AIE literature value of  $9.703 \pm 0.006$  eV.<sup>39-41</sup> The second inflection point at 9.93 eV is from propanal ( $C_3H_6O$ ) and matches well with the literature value of 9.96 eV reported by Wang *et al.*<sup>38</sup> The integrated photoelectron spectrum of glyoxal<sup>43</sup> with an AIE of 10.14 eV fits the remaining experimental data at higher photon energy. Figure 5-9 shows that the summation of the authentic photoionization spectra for all three products matches the experimental data satisfactorily.

Three species contribute to the signal at  $m/z = 70$ . The first onset at 8.65 eV is assigned to 2-methyl-2-butene ( $C_5H_{10}$ ). Its absolute photoionization energy curve<sup>44</sup> matches the experimental data well. The AIE of 2-methyl-2-butene as reported by Yang<sup>44</sup> is  $8.69 \pm 0.04$  eV, which is in agreement with the observed onset. The second species contributing to the  $m/z = 70$  signal is identified as 2-methyl-1-butene ( $C_5H_{10}$ ) because of the good agreement with its absolute photoionization spectrum and AIE of  $9.12 \pm 0.04$  eV.<sup>44</sup> The higher photon energy portion of the spectrum is assigned to 2-butenal ( $C_4H_6O$ ) with the literature AIE of  $9.75 \pm 0.04$  eV reported by Yang.<sup>44</sup> Figure 5-10 shows that the summation of all three products identified at  $m/z = 70$  fits reasonably the experimental photoionization spectrum. There is no presence of products at  $m/z = 70$  in the room temperature data.

The  $m/z = 72$  signal at 550 K comprises the contribution of three products. Two of the three differ from those seen at room temperature. The first onset at 9.20 eV is characterized as 2-buten-1-ol ( $C_4H_8O$ ),<sup>23</sup> the absolute photoionization spectrum of which fits well with the onset of the current experimental data. The second species is identified as cyclobutanol ( $C_4H_8O$ ) using the spectrum from Bouchoux *et al.*<sup>45</sup> The last product adding to the  $m/z = 72$  signal, is 2,2-dimethyloxirane.<sup>23</sup> The presence of the  $m/z = 42$  daughter ion confirms the identification of 2,2-dimethyloxirane. The summation of the photoionization curves superimposed to the current experimental photoionization spectrum shows a good agreement (Figure 5-11). Three products are identified to contribute to the signal at  $m/z = 86$ . The same species, 2-methoxy-1-butene, 2,2-dimethyloxetane, and  $\gamma$ -butyrolactone (GBL), characterized at room temperature are also present at 550 K. Two small mass peaks corresponding to  $m/z = 100$  and 116 are detected, and their characterization will be discussed below in the 700 K section.

### 5.5.3 Product Identification of TAME + Cl + O<sub>2</sub> at 700 K

Like the data collected at room temperature and 550 K, the experimental photoionization energy curve of  $m/z = 30$  matches well the literature photoionization spectrum of formaldehyde. The experimental onset of 10.83 eV is slightly lower than the literature reported value of 10.88 eV<sup>36</sup> and the CBS-QB3 calculated AIE value of 10.93 eV because of the possible presence of hot bands. The  $m/z = 42$  signal is identified as the daughter ion of 2,2-dimethyloxirane.<sup>23</sup> The signal at  $m/z = 56$  is matched by isobutene and 1-butene ( $C_4H_8$ ). The first experimental onset of approximately 9.2 eV is in good agreement with the literature reported AIE value of

9.22 eV for isobutene.<sup>44</sup> The second onset at about 9.5 eV matches the literature AIE value of 9.55 eV for 1-butene.<sup>37</sup> The last onset is the contribution of the <sup>13</sup>C isotopologue of  $m/z = 55$  ( $C_4H_7^+$ ) dissociative ionization fragment of 2-methyl-1-butene and 2-methyl-2-butene (Figure 5-13a). The summation of the two literature photoionization curves matches well the experimental spectrum as seen in Figure 5-13b.

The  $m/z = 68$  signal is assigned to furan ( $C_4H_4O$ ). The literature photoionization energy curve reported by Yang<sup>44</sup> agrees satisfactorily with the experimental data from the onset at 8.83 eV up to approximately 9.83 eV as seen in Figure 5-14. Three species contribute to the signal at  $m/z = 70$ . The literature reported adiabatic ionization energy for 2-methyl-2-butene is 8.69 eV.<sup>44</sup> The photoionization spectrum fits well with the experimental onset. The second species is identified as 2-methyl-1-butene matching the spectrum reported by Yang.<sup>44</sup> The third species signal begins at 9.85 eV and agrees with the ionization energy of 2-butenal ( $C_4H_6O$ ). The summation of the three authentic photoionization energy curves matches reasonably with the experimental photoionization spectrum shown in Figure 5-15. Finally, a signal is observed at  $m/z = 72$  and 86, but because of their poor signal-to-noise ratio it is difficult to characterize any possible products. In addition, kinetic traces for these two  $m/z$ , which show a  $t_0$  at much later time, suggest that these species are formed via higher-order chemistry. A comparison between primary product formaldehyde ( $m/z = 30$ ) and  $m/z = 72$  is presented in Figure 5-16a. At 500 K the formation of formaldehyde exhibits a fast phase followed by a slow phase. At 700 K on the other hand, the production of formaldehyde follows a three-stage process: a fast phase followed by a slow face up to about 10 ms, and then a simple

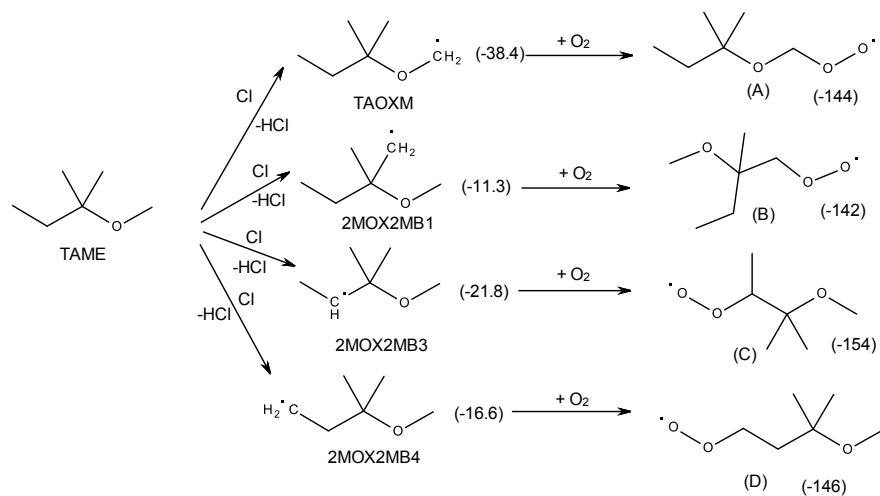
exponential formation from about 10 to 40 ms. Due to the formation patterns just mentioned, the formation of formaldehyde at 550 K is biphasic (Figure 5-16b). The rate constants for 550 K are  $531 \pm 136$  and  $45 \pm 27 \text{ s}^{-1}$ . This shows that the higher the temperature, the higher order of chemistry forms formaldehyde. The  $m/z = 70$  products, on the other hand, is fitted with a biphasic exponential function at 550 K. The estimated kinetic constants at 550 K are  $663 \pm 158$  and  $29 \pm 4 \text{ s}^{-1}$  at 500 K. Again,  $m/z = 72$  is a primary product at 550 K but a secondary product at 700 K. The rate of formation for  $m/z = 72$  at 550 K is  $353 \pm 31 \text{ s}^{-1}$ . The decay of TAME has a rate of  $781 \pm 84 \text{ s}^{-1}$  at 550 K.

An insignificant amount is detected at  $m/z = 100$  at all temperatures. The formation rate of  $m/z = 100$  is comparable to the depletion of  $m/z = 73$ , the dissociative photoionization fragment ion of TAME. The experimental time traces obtained at 298 K are shown as an example (Figure 5-17). The  $m/z = 100$  photoionization spectrum is in agreement of the Frank-Condon simulation of 3-methoxy-3-methyl-1-butene (Figure 5-18). A small peak at  $m/z = 116$ , which corresponds to the mass of the dioxanes, is observed at all temperatures. The rate of formation is comparable to the rate of depletion of the reactant (Figure 5-17). Figure 5-19a shows an example of the photoionization spectrum of  $m/z = 116$  at 700 K. It is in agreement with the summation of the simulated spectra of all possible  $m/z = 116$  isomers derived from the TAME + Cl + O<sub>2</sub> reaction. A signal is also observed at  $m/z = 115$  with a time trace comparable to that of  $m/z = 116$  (Figure 5-17) and an appearance energy higher than  $m/z = 116$  (about 9.7 eV for  $m/z = 115$  versus about 9.2 eV for  $m/z = 116$ ). It is possible that  $m/z = 115$  comes from  $m/z = 116$  by a cleavage of a hydrogen atom (M-H).

## 5.6 Proposed mechanism of TAME + Cl + O<sub>2</sub>

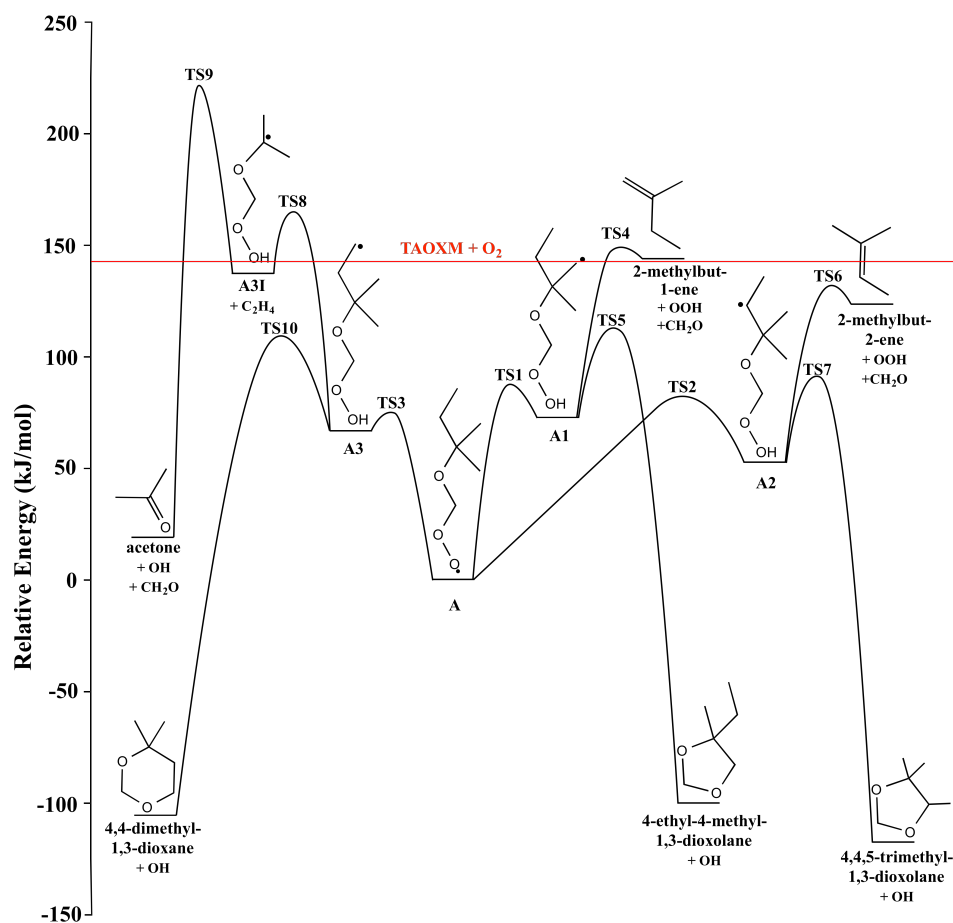
For clarity of discussion, TAME ( $m/z = 102$ ) is divided into two parts by the ethereal oxygen. One part will be designated as the tert-amyl (2-methyl-2-butyl) side, the other as the methoxy side. Chlorine can potentially abstract an H atom from four sites forming four different 2-methoxy-2-methylbutyl radicals ( $m/z = 101$ ) according to Scheme 5-1, i.e., tert-amoxymethyl (TAOXM), 2-methoxy-2-methylbut-1-yl (2MOX2MB1), 2-methoxy-2-methylbut-3-yl (2MOX2MB3), and 2-methoxy-2-methylbut-4-yl (2MOX2MB4). The reaction enthalpies for their formation are calculated as -38, -11, -22, and -17 kJ mol<sup>-1</sup>, respectively.

Molecular oxygen present in excess in the reaction mixture then bonds with the four mentioned alkoxyalkyl radicals to form the respective peroxy species, tert-amoxymethylperoxy (A), 1-methoxy-1-methylbutyl-1-peroxy (B), 1-methoxy-1-methylbutyl-3-peroxy (C), and 1-methoxy-1-methylbutyl-4-peroxy (D) (Scheme 5-1). The calculated enthalpies of reaction (0 K) for the formation of (A), (B), (C), and (D) are -144, -142, -154, and -146 kJ mol<sup>-1</sup>, respectively. The four alkoxyalkyl radicals + O<sub>2</sub> reactions will be used as the reference point for the energetic calculations of the products resulting from these radicals. Red lines, which correspond to the H-abstraction TAME radical + O<sub>2</sub>, are drawn according to this reference and the production of any molecular species positioned above these red lines is energetically unfavorable.



(Scheme 5-1)

All these alkoxyalkylperoxy ( $ROROO^*$ ) species undergo intramolecular hydrogen abstraction to become hydroperoxyalkoxyalkyl ( $ROQOOH$  and  $QOROOH$ ) radicals. Then, possible reaction mechanisms include: (a)  $\alpha$ - $\beta$  cleavage, producing smaller molecules; (b) OH cleavage followed by one of the oxygens from the hydroperoxy group bonding to the radical center, which yields cyclic ethers with two oxygen atoms in the ring; (c) loss of  $HOO$ , forming a double bond or a cyclic structure. Included in the proposed mechanisms are some radicals that are not directly detected, but whose presence is derived from the measurement of stable products, which are yielded in the same steps or formed by decomposition of these undetected radicals.



(Scheme 5-2)

When a hydrogen on the methoxy group of TAME is abstracted in the presence of oxygen, the ROROO\* radical denoted as (A) ( $m/z = 133$ ) is formed. There are three routes for (A) to yield (QOROOH) radicals depicted in Scheme 5-2. 2-(hydroperoxymethoxy)-2-methyl-1-butyl (A1), 2-(hydroperoxymethoxy)-2-methyl-3-butyl (A2), and 2-(hydroperoxymethoxy)-2-methyl-4-butyl (A3) are formed when (A) undergoes intramolecular hydrogen abstraction from C1, C3, and C4, respectively, on the tert-amyl side of (A). The enthalpies of rearrangement from (A) to (A1), (A2), and (A3) are 74, 55, and 68  $\text{kJ mol}^{-1}$ , respectively, where the energy of (A) is used as



the zero energy level. The corresponding activation enthalpy of the reactions from (A) to (A1), (A2) and (A3) are 89, 87, and 77 kJ mol<sup>-1</sup>, all below the initial abstraction radical (TAOXM) + O<sub>2</sub> channel (red line in all the schemes).

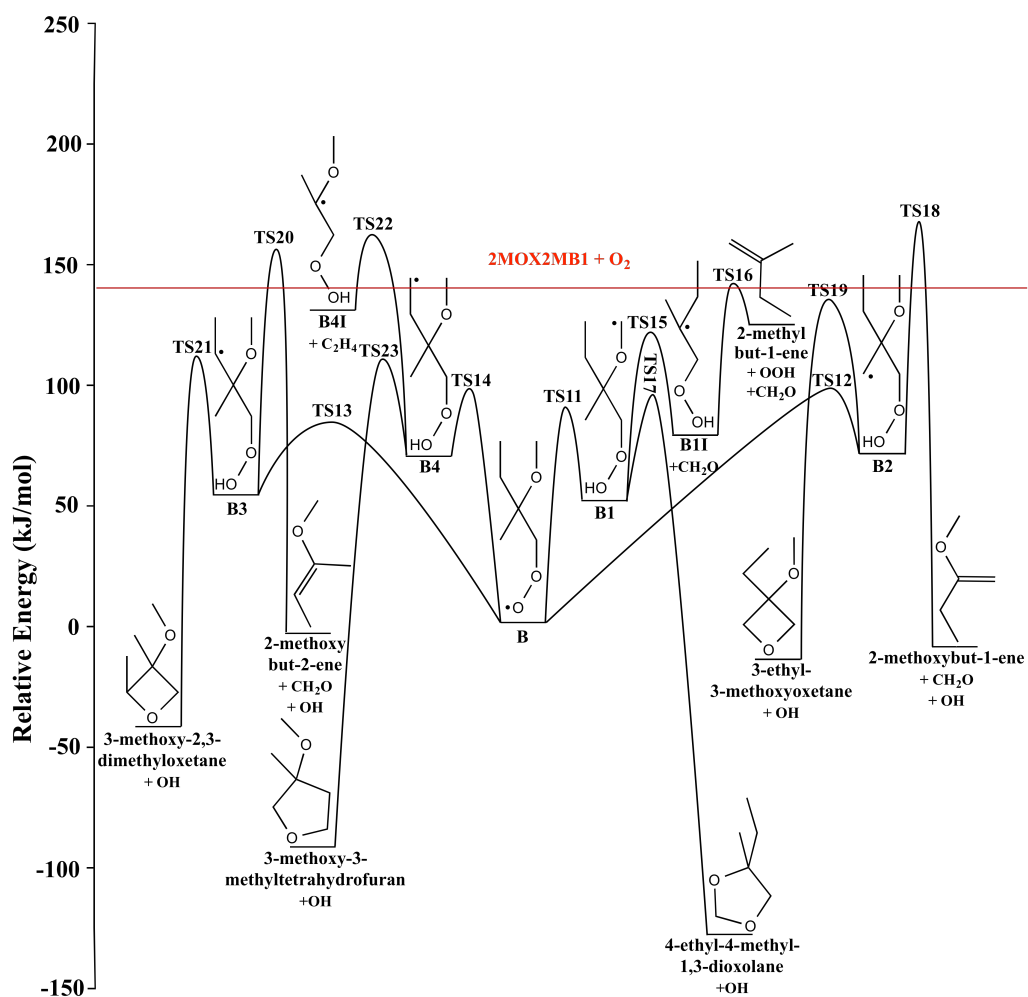
(A1) can be cleaved in two ways as shown in Scheme 5-2. The first route for the (A1) decomposition is to cleave it into formaldehyde, OOH, and 2-methyl-1-butene (*m/z* = 70) by breaking the bonds between C2 and the ethereal oxygen and between the methylene carbon and the peroxy oxygen. The calculated enthalpy of this decomposition is 72 kJ mol<sup>-1</sup>, while the enthalpy of activation is calculated to be 76 kJ mol<sup>-1</sup> (approximately 5 kJ mol<sup>-1</sup> higher than the TAOXM + O<sub>2</sub> channel). The second possible (A1) decomposition is via the formation of the C1-O bond, yielding 4-ethyl-4-methyl-1,3-dioxolane and OH, the formation of which is exothermic (-171 kJ mol<sup>-1</sup>), with an activation enthalpy of 41 kJ mol<sup>-1</sup>.

The second decomposition of (A) is through (A2), which is broken down into OOH, formaldehyde, and 2-methyl-2-butene. This step is endothermic from (A) with an enthalpy of 72 kJ mol<sup>-1</sup> and an enthalpy of activation of 79 kJ mol<sup>-1</sup>. When hydroxyl radical is cleaved from (A2), a cyclic ether, 4,4,5-trimethyl-1,3-dioxolane is formed. The calculated reaction enthalpy of 4,4,5-trimethyl-1,3-dioxolane is -170 kJ mol<sup>-1</sup>, while the enthalpy of activation is 40 kJ mol<sup>-1</sup>.

(A3) decomposes to ethene and 2-hydroperoxymethoxy-2-propyl radical (A3I), which then can break down to OH, formaldehyde, and acetone. The enthalpy of these consecutive reactions is 74 and -120 kJ mol<sup>-1</sup>, respectively, while the enthalpies of activation are 97 and 81 kJ mol<sup>-1</sup>, respectively. Both these barriers are above the initial H-abstraction radical + O<sub>2</sub> channel. Alternatively, (A3) turns into a

cyclic ether, 4,4-dimethyl-1,3-dioxane by cleaving off hydroxyl radical, with an exothermicity of  $-178 \text{ kJ mol}^{-1}$ . The activation enthalpy of this step is  $42 \text{ kJ mol}^{-1}$ .

At room temperature, the absence of  $m/z = 70$  indicates that initial oxidation of TAME does not take place at the methoxy carbon. Therefore, the formation of the resulting products from (A) does not occur at this temperature. Experimental conditions at the higher temperatures of 550 and 700 K seem to be more favorable for the pathways through (A). Characterization of the species at  $m/z = 70$  reveals the presence of 2-methyl-1-butene and 2-methyl-2-butene, products formed from the (A1) and (A2) radicals, respectively. In addition, formaldehyde, is identified at  $m/z = 30$ . These products support the proposed mechanisms of the (A1) and (A2) routes described above at 550 and 700 K. As far as mechanism in the (A3) route, the presence of formaldehyde and acetone at 550 K suggests that the pathway through the (A3) radicals may occur, but the absence of ethene proves otherwise. It can be concluded that the schemes above are unfavorable at room temperature, and only the mechanisms shown in (A1) and (A2) routes contribute to TAME oxidation at 550 and 700 K, due to the fact that all transition states in the (A1) and (A2) routes are below or near the red line while TS 8 in the (A3) route is above it. The cyclic dioxanes and dioxolane in all routes have favorable transition state energies.



(Scheme 5-3)

When a hydrogen atom from one of the tert-amyl methyl groups is abstracted, with subsequent oxygen addition on the radical center, (B) is formed that through intramolecular hydrogen abstraction yields hydroperoxyalkoxyalkyl radicals as shown in Scheme 5-3. The red line represents the energy level of 2MOXMB1 + O<sub>2</sub>. Any species with energy level higher than this red line is energetically unfavorable to be produced. If the intramolecular hydrogen abstraction takes place on the methoxy group, (B1) is formed. On the other hand, if the abstraction occurs on the methyl

group not attached to the oxygen, (B2) and/or (B4) are produced. Finally, (B) can rearrange to yield (B3) by intramolecular abstraction of the hydrogen atoms on C3. The calculated reaction enthalpies from the intramolecular hydrogen abstraction yielding (B1), (B2), (B3), and (B4) are 54, 68, 57, and 64  $\text{kJ mol}^{-1}$ , respectively, where (B) is used as the reference zero energy level for Scheme 5-3. The activation enthalpies of these reactions are 89, 100, 83, and 98  $\text{kJ mol}^{-1}$ , respectively.

After (B) rearranges to (B1), there are two pathways along which (B1) can decompose. The bond between the ethereal oxygen and the tertiary carbon on the tert-amyl side of (B1) can be broken, producing formaldehyde and (B11). The enthalpy of this step is 26  $\text{kJ mol}^{-1}$ , while the enthalpy of activation is 67  $\text{kJ mol}^{-1}$ . An  $\alpha$ - $\beta$  cleavage then breaks (B11) into 2-methyl-1-butene ( $m/z = 70$ ) and hydroperoxy radical. The calculated enthalpy of forming 2-methyl-1-butene and hydroperoxy radical is 46  $\text{kJ mol}^{-1}$ , and the activation enthalpy is 61  $\text{kJ mol}^{-1}$ . The alternative decomposition of (B1) yields 4-ethyl-4-methyl-1,3-dioxolane and OH. The enthalpy of this step is -182  $\text{kJ mol}^{-1}$ . The enthalpy of the activation of this reaction is calculated to be 43  $\text{kJ mol}^{-1}$ .

OH is cleaved from (B2) yielding 3-ethyl-3-methoxyoxetane. The calculated enthalpy is -85  $\text{kJ mol}^{-1}$ , with an enthalpy of activation of 68  $\text{kJ mol}^{-1}$ . Another decomposition pathway from (B2) is cleavage into 2-methoxy-2-methyl-1-butene, formaldehyde and OH. The calculated enthalpy of this step and its activation enthalpy are -80 and 96  $\text{kJ mol}^{-1}$ , respectively.

Like most of the hydroperoxyalkoxyalkyl radicals mentioned above, (B3) has two degradation pathways, as shown in Scheme 5-3. The first is via breaking the

bond between the tertiary carbon and carbon to which the hydroperoxy group is bound. The resulting products are 2-methoxy-2-butene, OH, and formaldehyde. This process is exothermic ( $-60 \text{ kJ mol}^{-1}$ ), with an enthalpy of activation calculated to be  $98 \text{ kJ mol}^{-1}$ . In addition to the formation of 2-methoxy-2-butene, (B3) can also decompose to form 3-methoxy-2,3-dimethyloxetane and hydroxyl radical. The calculated enthalpy for this step is  $-95 \text{ kJ mol}^{-1}$ . The enthalpy of activation is  $56 \text{ kJ mol}^{-1}$ .

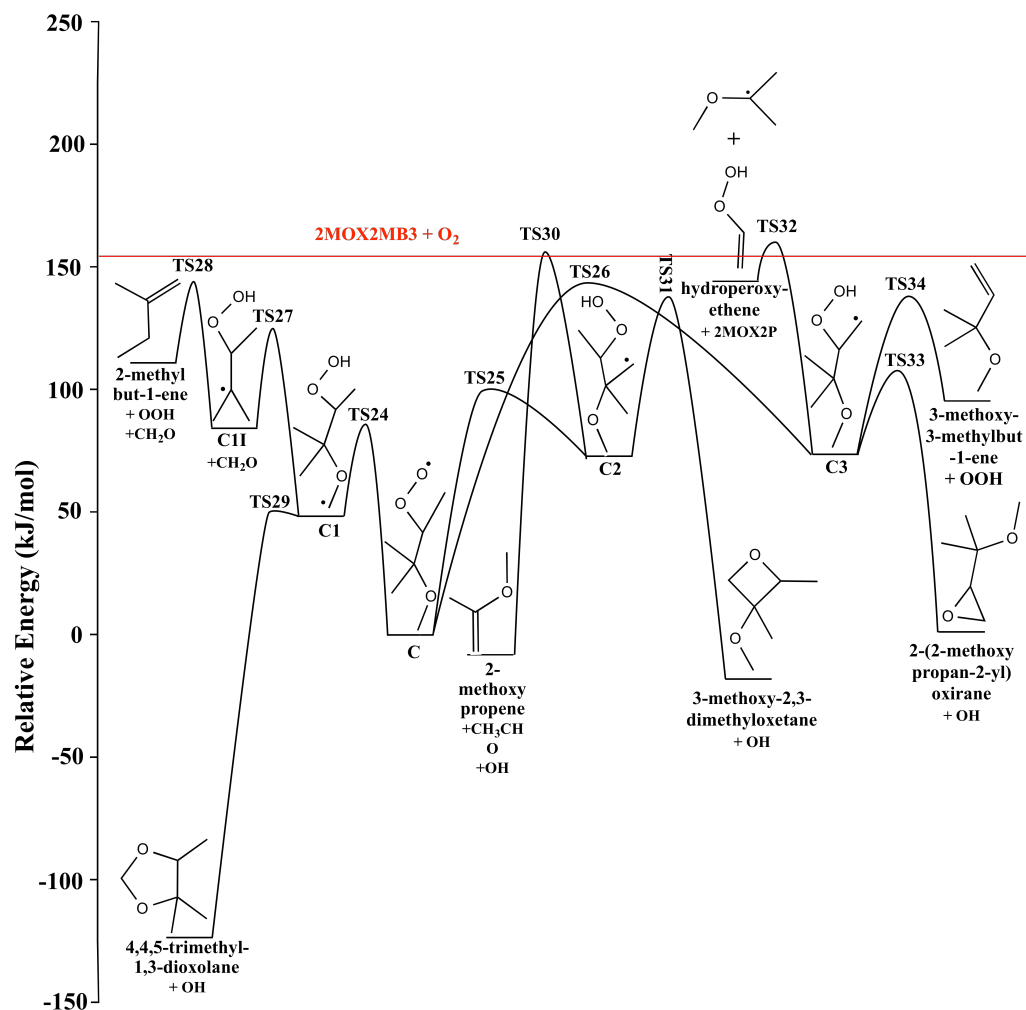
The final possible intramolecular hydrogen abstraction of (B) is represented by (B4). Ethene and (B4I) are the products formed when (B4) undergoes unimolecular decomposition. The calculated enthalpy of this process is  $68 \text{ kJ mol}^{-1}$ , while the activation enthalpy is  $94 \text{ kJ mol}^{-1}$ . (B4I) can also be cleaved into 2-methoxypropene and hydroperoxy radical with an enthalpy of  $36 \text{ kJ mol}^{-1}$ . However, the products of this reaction is  $13 \text{ kJ mol}^{-1}$  higher than the red line. Due to the endothermicity for the formation of 2-methoxypropene through this channel, it is not included in Scheme 5-3. Alternatively, (B4) can break apart into 3-methoxy-3-methyltetrahydrofuran and hydroxyl radical exothermically ( $-154 \text{ kJ mol}^{-1}$ ), with an enthalpy of reaction of  $46 \text{ kJ mol}^{-1}$ .

Identification of 2-methyl-1-butene ( $m/z = 70$ ) at 700 K indicates that the formation pathway through the (B1) hydroperoxyalkoxyalkyl radical is favorable. The likeliness of this route at higher temperature conditions is further supported by the presence of formaldehyde. This appears to be the only pathway through (B) to transpire at 700 K. Only (B1) route has transition states (slightly above the red line) that lead to linear non-dioxane products. All other channels leading to linear non-

dioxane have transition states higher than the red line. The characterization of 2-methyl-1-butene and formaldehyde at 550 K suggests that the pathway through (B1) is also present at this temperature. The absence of 2-methyl-1-butene at 298 K eliminates the (B1) route as a possible reaction mechanism at this temperature. (B1) is formed via Cl initiated H abstraction from the methoxy carbon.

The presence of 2-methoxy-1-butene ( $m/z = 86$ ) and formaldehyde at both room temperature and 550 K suggests product formation may occur via hydroperoxyalkoxyalkyl radical (B2). The 2-methoxy-2-butene isomer ( $m/z = 86$ ) is also observed at room temperature and 550 K. The species is an indication that formation through (B3) is another favorable pathway under these temperature conditions. The lack of signal at  $m/z = 28$  can be explained by the fact that TS 22 is above the red line.

The product of the reaction between oxygen and 2-methoxy-2-methyl-3-butyl is (C). Like (A) and (B), (C) will undergo intramolecular hydrogen abstraction, forming hydroperoxyalkoxyalkyl radicals. There are three possible rearrangements of (C). If the hydrogen on the methyl side of (C) is abstracted, (C1) is formed. Likewise, if the hydrogen on C1 position of the tert-amyl side is abstracted, (C2) is produced instead. Also, (C3) can be generated when hydrogen is abstracted from C4 of the tert-amyl side. These three reactions are depicted in Scheme 5-4 with a red line indicating the threshold for exothermicity. The calculated enthalpies yielding (C1), (C2), and (C3) are 48, 75, and 74  $\text{kJ mol}^{-1}$ , respectively, with (C) set as the zero energy level. The activation enthalpies for formation of these hydroperoxyalkoxyalkyl radicals are 85, 98, and 143  $\text{kJ mol}^{-1}$ , respectively.



(Scheme 5-4)

The first possible hydroperoxyalkoxyalkyl radical that (C) rearranges to is (C1). When the bond between the ethereal oxygen and the tertiary carbon on the amyl side is broken, formaldehyde and (C1) are produced. The calculated enthalpy of this step is 32 kJ mol<sup>-1</sup>. The activation enthalpy of this reaction is 81 kJ mol<sup>-1</sup>. (C1) can break apart further into 2-methyl-1-butene and hydroperoxy radical. The enthalpy of formation for 2-methyl-1-butene via (C1) is 36 kJ mol<sup>-1</sup>, and its activation enthalpy is 64 kJ mol<sup>-1</sup>. (C1) can also decompose into 4,4,5-trimethyl-1,3-dioxolane

and hydroxyl radical exothermically ( $-174 \text{ kJ mol}^{-1}$ ). The calculated activation enthalpy of this step is only  $2 \text{ kJ mol}^{-1}$ .

Another possibility of (C) rearrangement is (C2). There are two possible routes for (C2) to decompose. The first one is the conversion to 3-methoxy-2,3-dimethyloxetane and hydroxyl radical as shown in Scheme 5-4. The calculated enthalpy of this reaction is  $-93 \text{ kJ mol}^{-1}$ , with an activation enthalpy of  $61 \text{ kJ mol}^{-1}$ . The second pathway is the production of 2-methoxypropene, acetaldehyde and OH. The enthalpy of this reaction is  $-82 \text{ kJ mol}^{-1}$ , while the enthalpy of activation is  $191 \text{ kJ mol}^{-1}$ .

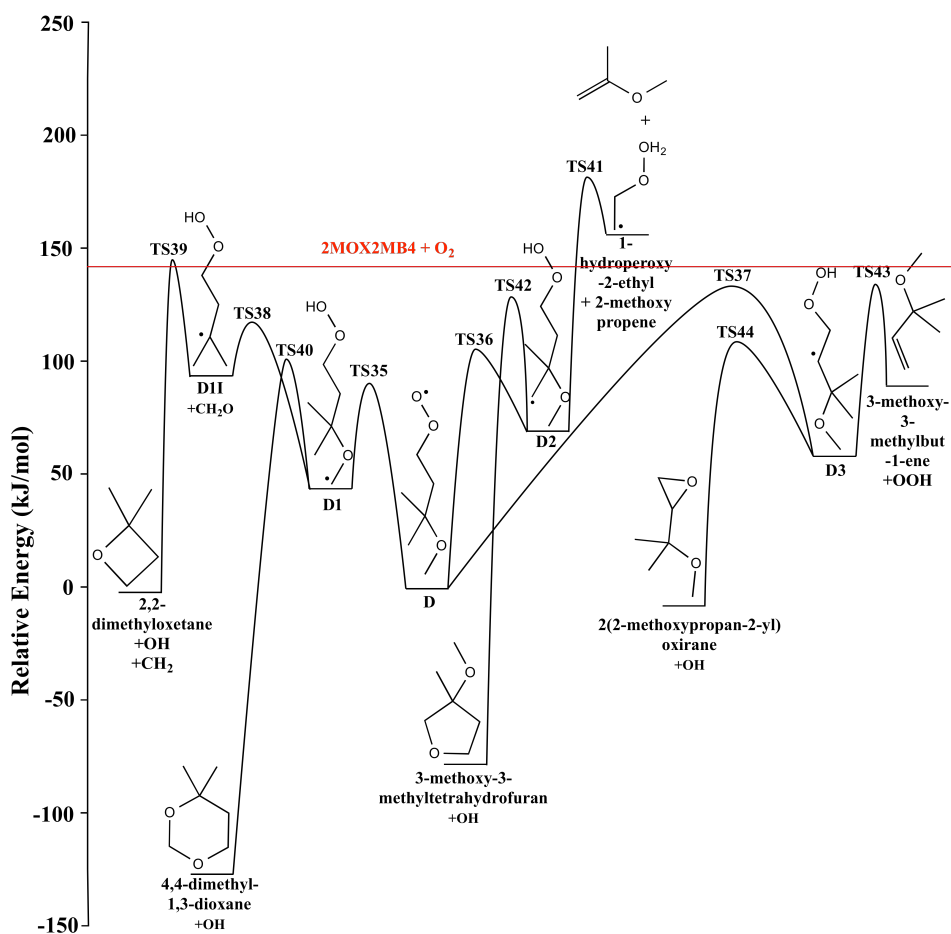
The final possible (C) isomerization is via (C3). Unlike the other hydroperoxyalkoxyalkyl radical isomers of (C), (C3) has three decomposition pathways. The first is by breaking the bond between C2 and C3 of the tert-amyl side to generate hydroperoxyethene and 2-methoxy-2-propyl radical (2MOX2P). The calculated heat of this step is  $73 \text{ kJ mol}^{-1}$ , while the activation enthalpy is  $87 \text{ kJ mol}^{-1}$ . The second possibility for (C3) is through cleaving the bond between the oxygen bonded to C3 of the tert-amyl side and C3 itself. The result is the product 3-methoxy-3-methyl-1-butene with an enthalpy of reaction and enthalpy of activation calculated to be  $18$  and  $64 \text{ kJ mol}^{-1}$ , respectively. The final possible (C3) pathway is the formation of 2-(1-methoxy-1-methylethyl)oxirane and hydroxyl radical with a calculated enthalpy of  $-73 \text{ kJ mol}^{-1}$  and an activation of  $41 \text{ kJ mol}^{-1}$ .

The observation of 2-methyl-1-butene and formaldehyde suggests that the (C1) pathway is favorable, which is consistent with the fact that the enthalpy of activation for producing (C1) is lower than that of (C2) and (C3). Formaldehyde is



present at all temperatures, whereas 2-methyl-1-butene is only detected at 550 and 700 K. This suggests that possibly more thermal energy is needed to overcome TS 28. 2-methoxypropene is detected at room temperature. The calculated enthalpy of activation is only 1 kJ mol<sup>-1</sup> above the red line. The error of the energetic calculation by CBS-QB3 is 1–1.5 kcal mol<sup>-1</sup> (or 4–6 kJ mol<sup>-1</sup>) according to Sirjean *et al.*<sup>46</sup> Therefore, it is possible that the true energy level of TS 30 is slightly below the red line and 2-methoxypropene is likely to be produced through (C2).

According to Scheme 5-1, the final possible alkoxyalkylperoxy radical produced by the TAME + Cl + O<sub>2</sub> reaction is (D), which can isomerize to (D1), (D2), and (D3), according to Scheme 5-5. (D) is used as the reference point for the calculation of enthalpy of reaction in Scheme 5-5 and the red line is the threshold of exothermicity. If a hydrogen from the methoxy side is abstracted, (D1) is formed. Similarly, when a hydrogen is removed from C1 or C3 of the tert-amyl side, (D2) and (D3) are generated, respectively. The structures of the isomers of (D) are shown in Scheme 5-5. The calculated enthalpies of formation for (D1), (D2) and (D3) are 46, 71, and 59 kJ mol<sup>-1</sup>, respectively. The enthalpies of activation for reactions from (D) to (D1), (D2) and (D3) are 84, 112, 134 kJ mol<sup>-1</sup>.



(Scheme 5-5)

(D1) has two possible decomposition pathways presented in Scheme 5-5. When the bond between the tertiary carbon on the tert-amyl side and the ethereal oxygen is cleaved, formaldehyde and (D1I) are produced with a calculated enthalpy of  $43 \text{ kJ mol}^{-1}$ . The transition state from D1 to D1I and formaldehyde is calculated to be  $75 \text{ kJ mol}^{-1}$  above (D). (D1I) is then broken down into 2,2-dimethyloxetane and hydroxyl radical exothermically ( $-90 \text{ kJ mol}^{-1}$ ), with a barrier of  $58 \text{ kJ mol}^{-1}$ . Alternatively, (D1) can form 4,4-dimethyl-1,3-dioxane. The enthalpy of this reaction is  $-178 \text{ kJ mol}^{-1}$ , with an enthalpy of activation of  $54 \text{ kJ mol}^{-1}$ .

The second hydroperoxyalkoxyalkyl isomer of (D) is (D2). When the C2-C3 bond on the tert-amyl side is broken, 2-methoxypropene and 1-hydroperoxy-2-ethyl are generated. The calculated enthalpy of this step is  $91 \text{ kJ mol}^{-1}$  with a barrier of  $109 \text{ kJ mol}^{-1}$ . (D2) yields a 5-member cyclic ether, 3-methoxy-3-methyltetrahydrofuran, together with an hydroxyl radical with a CBS-QB3 enthalpy of  $-152 \text{ kJ mol}^{-1}$  and a transition state of  $58 \text{ kJ mol}^{-1}$  that is  $129 \text{ kJ mol}^{-1}$  above (D).

Scheme 5-5 shows the reaction of (D3). When the hydroperoxy group is cleaved from C4 on the tert-amyl side, 3-methoxy-3-methyl-1-butene and  $\text{HO}_2$  are yielded. The calculated enthalpy of this step is  $22 \text{ kJ mol}^{-1}$ , while the enthalpy of activation is  $74 \text{ kJ mol}^{-1}$ . Alternatively, when the hydroxyl group is cleaved from (D3), 2-(1-methoxy-1-methylethyl)oxirane is produced exothermically with a calculated enthalpy of  $-69 \text{ kJ mol}^{-1}$  and a barrier of  $51 \text{ kJ mol}^{-1}$  that is  $110 \text{ kJ mol}^{-1}$  above (D).

Formaldehyde, 2,2-dimethyloxetane, and 2-methoxypropane are observed. Formaldehyde again is present at all temperatures, while the concentration of 2,2-dimethyloxetane is too low to contribute to the overall reaction. Therefore, it can be concluded that the (D1) route is favorable at all temperature up to TS 39 (too high for the reaction to proceed). 2-methoxypropene is only present at room temperature. It is produced from the (D2) route. However, TS 41, the transition state for producing 2-methoxypropene is the highest in Scheme 5-5, so the substituted propene may be formed from the (C2) pathway instead of the (D2) route.

## 5.7 Branching Fractions

Total branching fractions for each experimental temperature are presented in Table 5-1. The branching fraction of formaldehyde ( $m/z = 30$ ) is 10% at room

temperature, then increases to 13% and 14 % at 550 K and 700 K, respectively. Acetaldehyde ( $m/z = 44$ ) is only present at room temperature. However, it cannot be explained based on the schematics (A-D) described in the previous section. Therefore, it is considered a secondary product. The signal at  $m/z = 56$  has been identified at all three temperatures as 1-butene. Isobutene on the other hand is only present at 700 K in the  $m/z = 56$  signal. Like acetaldehyde, the production of 1-butene and isobutene cannot be accounted by Schemes A-D; hence, they are also characterized as secondary products.

Multiple products have been identified at  $m/z = 58$ . Among them, propanal and glyoxal are not in the Schemes A-D above, and thus, are considered secondary products. Propanal cannot be yielded directly from TAME because a saturated linear three-carbon-long-chain with an oxygenated carbon at the first or third position is absent in TAME. The production of glyoxal with two aldehydic groups requires two oxidation steps. Acetone, which can be explained from the proposed TAME oxidation mechanism, has a branching fraction of 3, 3, and 2% at 298, 550 and 700 K, respectively.

Furan ( $m/z = 68$ ) is observed only at 700 K. There is another species adding to the signal at  $m/z = 68$ , but it is not characterized at this time. The formation of  $m/z = 68$  cannot be predicted from the oxidation of TAME, so furan and a possible isomer are likely to be secondary products. To illustrate, furan is a cyclic compound that has two double bonds, which requires at least two oxidation steps to be produced from TAME. Signal at  $m/z = 70$  is present only at 550 and 700 K. Contributing products are 2-methyl-1-butene, 2-methyl-2-butene ( $C_5H_{10}$ ), and 2-butenal ( $C_4H_6O$ ). It is

predicted that 2-butenal is a secondary product because its formation requires multiple oxidation steps. In fact, the ethereal oxygen of TAME is on the second carbon, whereas the aldehydic group of 2-butenal is on the terminal carbon. Therefore, to produce 2-butenal from TAME, multiple steps are required for making the double bond and shifting the secondary ethereal oxygen to the terminal aldehyde. Calculated branching fractions for 2-methyl-1-butene and 2-methyl-2-butene at 550 K are 44% and 15%, respectively. The branching fractions decrease at 700 K to 39% for 2-methyl-1-butene and to 10% for 2-methyl-2-butene.

The parent ion 2,2-dimethyloxirane ( $m/z = 72$ ) is present at room temperature and 550 K, but it is very likely a secondary product because it is not found in the Schemes A-D. The species 2-butenol and cyclobutanol are identified at  $m/z = 72$  at 550 K, but neither can be produced from the initial oxidation steps and are therefore suspected to be secondary products. The signal at 700 K for  $m/z = 72$  has poor signal-to-noise ratio and the experimental time trace, shown in Figure 5-16, suggests these products to be formed via secondary chemistry. Also contributing to the  $m/z = 72$  is 2-methoxy-1-propene ( $C_4H_8O$ ) with a branching fraction of 8%, 8%, and 1% at 298, 550, and 700 K.

Four products are characterized for the signal at  $m/z = 86$ . They are  $\gamma$ -butyrolactone, 2-methoxy-1-butene, 2-methoxy-2-butene, and 2,2-dimethyloxetane. The formation of  $\gamma$ -butyrolactone requires multiple oxidation steps and therefore is not considered a primary product. At room temperature 2-methoxy-1-butene, 2-methoxy-2-butene, and 2,2-dimethyloxetane have signals too low to contribute to TAME oxidation. The branching fraction of 2-methoxy-1-butene is 2%, while the

other species are negligible at 550 K. The branching fraction of 2,2-dimethyloxetane is 1%, while the other species are negligible at 700 K.

3-Methoxy-3-methyl-1-butene ( $m/z = 100$ ) and 3-methoxy-3-methyltetrahydrofuran ( $m/z = 116$ ), 3-methoxy-2,3-dimethyloxetane ( $m/z = 116$ ), 2-(1-methoxy-1-methylethyl)oxirane ( $m/z = 116$ ), 4,4,5-trimethyl-1,3-dioxolane ( $m/z = 116$ ), 4,4-dimethyl-1,3-dioxane ( $m/z = 116$ ), 4-ethyl-3-methyl-1,3-dioxolane ( $m/z = 116$ ) and 3-ethyl-3-methoxyoxetane ( $m/z = 116$ ) are possibly detected and their branching fraction are calculated using photoionization cross-sections estimated by the Bobeldijk method.<sup>47</sup> First the estimated cross-sections are estimated at 11.8 eV. Then, the simulated photoionization spectra are scaled to match such values to create plots of photon energy versus photoionization cross-section. The cross-sections at 11.0 eV are plugged into equation (2) and are listed in Table 5-2. The branching fractions are as follows: 0.1 % for 3-methoxy-3-methyl-1-butene at all temperatures, and 0.2%, 0.4%, and 0.1% for all  $m/z = 116$  isomers at 298, 550 and 700 K. The individual branching fractions are listed in Table 5-3. Because they are less than 1% and do not contribute much to the total branching fraction, their branching fractions are reported as insignificant in Table 5-1. However, it is likely that these molecules are not very volatile, resulting in apparent low concentrations. Another reason is that they are possibly fragmented during photoionization making their signal lower than expected, thereby underestimating their branching fractions. The possible photoionization dissociation fragment is at  $m/z = 115$  (Figure 5-17 and Figure 5-19b).

The total branching fraction at room temperature is only 22%. The presence of several secondary products, including identified species in this report and confirmed chlorinated species at higher masses, result in branching fractions that are lower than expected. It is difficult to account for all secondary reactions because it is possible for secondary products to react away within the same time scale of primary reactions. If a primary product reacts immediately with chlorine after formation, its ion intensity is less than it would be if no further reaction occurs. On the other hand, the total branching fractions for both 550 and 700 K are 85% and 67%, respectively, which within our estimated 20% uncertainty are close to the full mass balance. In addition, as described above, the  $m/z = 100$  and 116 species may not be volatile leading to the underestimation of their branching fractions. Hence, based on the calculated potential energy surfaces it is very likely that they contribute to the remaining 78, 15, and 33 % of the total branching fraction at the 298, 550, and 700 K.

## 5.8 Conclusions

The oxidation of TAME, an oxygenated fuel additive, is investigated via its reaction with Cl and O<sub>2</sub> at 298, 550, and 700 K. All experiments were carried out at the Advanced Light Source (ALS) located in the Lawrence Berkeley National Laboratory. Oxidation products and intermediates are detected by a multiplex time- and energy- resolved mass spectrometer. The synchrotron radiation generated at the ALS was utilized as the ionization source of the mass spectrometer. Primary reaction products are identified based on kinetic profiles, mass-to-charge ratios, ionization energies, and photoionization spectra. In addition, the potential energy surface for the reaction of the initial H-abstraction radical of TAME and O<sub>2</sub> have been carried out

using the CBS-QB3 composite method to substantiate the observed products. Branching fractions of all primary products are calculated. The total branching fractions are 22%, 85% and 67% at 298, 550, and 700 K, respectively. At room temperature, the most significantly contributing products are formaldehyde (10%) and 2-methoxy-1-propene (8%). At 550 K, formaldehyde (13%), 2-methyl-1-butene (44%) and 2-methyl-2-butene (15%) have the highest branching fractions. Similarly at 700 K, the same set of species dominates the contribution of the total branching fraction. At this temperature the branching fractions are 14%, 39% and 10% for formaldehyde, 2-methyl-1-butene, and 2-methyl-2-butene, respectively.



## 5.9 References

1. Westphal, G. A.; Krahl, J.; Brüning, T.; Hallier, E.; Bünger, J., Ether Oxygenate Additives in Gasoline Reduce Toxicity of Exhausts. *Toxicology* **2010**, *268*, 198-203.
2. Seagrave, J.; McDonald, J. D.; Gigliotti, A. P.; Nikula, K. J.; Seilkop, S. K.; Gurevich, M.; Mauderly, J. L., Mutagenicity and *In Vivo* Toxicity of Combined Particulate and Semivolatile Organic Fractions of Gasoline and Diesel Engine Emissions. *Toxicol. Sci.* **2002**, *70*, 212-226.
3. Seagrave, J.; Mauderly, J. L.; Seilkop, S. K., *In Vitro* Relative Toxicity Screening of Combined Particulate and Semivolatile Organic Fractions of Gasoline and Diesel Engine Emissions. *J. Toxicol. Env. Heal. A* **2003**, *66*, 1113-1132.
4. *Public Health and Welfare. US Code. 7401-7671, Title 42, 1977.*
5. Sutherland, J.; Adams, C., Determination of Hydroxyl Radical Rate Constants for Fuel Oxygenates. *Environ. Eng. Sci.* **2007**, *24*, 998-1005.
6. Squillance, P. J.; Pankow, J. F.; Korte, N. E.; Zogorski, J. S. *Environmental Behavior and Fate of Methyl Tert-Butyl Ether (MTBE)*; FS-203-96; US Department of Interior - US Geological Survey: 1998.
7. Deeb, R. A.; Scow, K. M.; Alvarez-Cohen, L., Aerobic MTBE Biodegradation: an Examination of Past Studies, Current Challenges and Future Research Directions. *Biodegradation* **2000**, *11*, 171-185.
8. Stocking, A. J.; Deeb, R. A.; Flores, A. E.; Stringfellow, W.; Talley, J.; Brownell, R.; Kavanaugh, M. C., Bioremediation of MTBE: a Review from a Practical Perspective. *Biodegradation* **2000**, *11*, 187-201.
9. State Actions Banning MTBE; EPA420-B-07-013; United State Environmental Protection Agency: 2007.
10. Mao, W.; Wang, X.; Wang, H.; Chang, H.; Zhang, X.; Han, J., Thermodynamic and Kinetic Study of Tert-Amyl Methyl Ether (TAME) Synthesis. *Chem. Eng. Process.* **2008**, *47*, 761-769.
11. Goldaniga, A.; Faravelli, T.; Ranzi, E.; Dagaut, P.; Cathonnet, M., Oxidation of Oxygenated Octane Improvers: MTBE, ETBE, DIPE, and TAME. *Symp. (Int.) Combust.* **1998**, *27*, 353-360.
12. Ancillotti, F.; Fattore, V., Oxygenate Fuels: Market Expansion and Catalytic Aspect of Synthesis. *Fuel. Process. Technol.* **1998**, *57*, 163-194.

13. Wallington, T. J.; Potts, A. R.; Andino, J. M.; Siegl, W. O.; Zhang, Z.; Kurylo, M. J.; Huie, R. E., Kinetics of the Reaction of OH Radicals with T-Amyl Methyl Ether Revisited. *Int. J. Chem. Kinet.* **1993**, *25*, 265-272.
14. Smith, D. F.; McIver, C. D.; Kleindienst, T. E., Kinetics and Mechanism of the Atmospheric Oxidation of Tertiary Amyl Methyl Ether. *Int. J. Chem. Kinet.* **1995**, *27*, 453-472.
15. Teton, S.; Mellouki, A.; Le Bras, G.; Sidebottom, H., Rate Constants for Reactions of OH Radicals with a Series of Asymmetrical ethers and Tert-Butyl Alcohol. *Int. J. Chem. Kinet.* **1996**, *28*, 291-297.
16. Osborn, D. L.; Zou, P.; Johnsen, H.; Hayden, C. C.; Taatjes, C. A.; Knyazev, V. D.; North, S. W.; Peterka, D. S.; Ahmed, M.; Leone, S. R., The Multiplexed Chemical Kinetic Photoionization Mass Spectrometer: A New Approach to Isomer-Resolved Chemical Kinetics. *Rev. Sci. Instrum.* **2008**, *79*, 104103-104101-104013-104110.
17. Taatjes, C. A.; Hansen, N.; Osborn, D. L.; Kohse-Hoinghaus, K.; Cool, T. A.; Westmoreland, P. R., "Imaging" Combustion Chemistry via Multiplexed Synchrotron-Photoionization Mass Spectrometry. *Phys. Chem. Chem. Phys.* **2008**, *10*, 20-34.
18. Ray, A. W.; Taatjes, C. A.; Welz, O.; Osborn, D. L.; Meloni, G., Synchrotron Photoionization Measurements of OH-Initiated Cyclohexene Oxidation: Ring-Preserving Products in OH + Cyclohexene and Hydroxycyclohexyl + O<sub>2</sub> Reactions. *The Journal of Physical Chemistry A* **2012**, *116*, 6720-6730.
19. Ng, M. Y.; Nelson, J.; Taatjes, C. A.; Osborn, D. L.; Meloni, G., Synchrotron Photoionization Study of Mesitylene Oxidation Initiated by Reaction with Cl(<sup>2</sup>P) or O(<sup>3</sup>P) Radicals. *The Journal of Physical Chemistry A* **2014**, *118*, 3735-3748.
20. IUPAC Subcommittee on Gas Kinetic Data Evaluation – Data Sheet PCI11. <http://iupac.pole-ether.fr/>.
21. Maric, D.; Burrows, J. P.; Meller, R.; Moortgat, G. K., A Study of the UV--Visible Absorption Spectrum of Molecular Chlorine. *J. Photochem. Photobiol., A* **1993**, *70*, 205-214.
22. Chupka, W. A.; Berkowitz, J., Photoionization of Ethane, Propane, and n-Butane with Mass Analysis. *J. Chem. Phys.* **1967**, *47*, 2921-2933.
23. Welz, O., *et al.*, Low-Temperature Combustion Chemistry of Biofuels: Pathways in the Initial Low-Temperature (550 K-750 K) Oxidation Chemistry of Isopentanol. *Phys. Chem. Chem. Phys.* **2012**, *14*, 3112–3127.
24. Montgomery, J. A., Jr.; Frisch, M. J.; Ochterski, J. W.; Petersson, G. A., A Complete Basis Set Model Chemistry. VI. Use of Density Functional Geometries and Frequencies. *J. Chem. Phys.* **1999**, *110*, 2822-2827.

25. Montgomery, J. A., Jr.; Frisch, M. J.; Ochterski, J. W.; Petersson, G. A., A Complete Basis Set Model Chemistry. VII. Use of The Minimum Population Localization Method. *J. Chem. Phys.* **2000**, *112*, 6532-6542.
26. Barckholtz, T. A.; Joshi, A.; Wang, H., In *In 4th Joint Meeting of the U.S. Sections of the Combustion Institute*, Drexel University: Philadelphia, PA, 2005.
27. Baulch, D. L., *et al.*, Evaluated Kinetic Data for Combustion Modeling: Supplement II. *J. Phys. Chem. Ref. Data* **2005**, *34*, 757-1397.
28. Cool, T. A.; McIlroy, A.; Qi, F.; Westmoreland, P. R.; Poisson, L.; Peterka, D. S.; Ahmed, M., Photoionization Mass Spectrometer for Studies of Flame Chemistry with a Synchrotron Light Source. *Rev. Sci. Instrum.* **2005**, *76*, 094102-094101-094102-094107.
29. Oehlschlaeger, M. A.; Davidson, D. F.; Hanson, R. K., Experimental Investigation of Toluene + H → Benzyl + H<sub>2</sub> at High Temperatures. *J. Phys. Chem. A* **2006**, *110*, 9867-9873.
30. Santoro, F.; Improta, R.; Lami, A.; Bloino, J.; Barone, V., Effective Method to Compute Franck-Condon Integrals for Optical Spectra of Large Molecules in Solution. *J. Chem. Phys.* **2007**, *126*, 084509-084501-084509-084513.
31. Duschinsky, F., *Physicochim. URSS* **1937**, *7*, 551-566.
32. Ruhoff, P. T., Recursion Relations for Multi-Dimensional Franck-Condon Overlap Integrals. *Chem. Phys.* **1994**, *186*, 355-374.
33. Sharp, T. E.; Rosenstock, H. M., Franck—Condon Factors for Polyatomic Molecules. *J. Chem. Phys.* **1964**, *41*, 3453-3463.
34. Lermé, J., Iterative Methods to Compute One- and Two-Dimensional Franck-Condon Factors. Tests of Accuracy and Application to Study Indirect Molecular Transitions. *Chem. Phys.* **1990**, *145*, 67-88.
35. Morton, T. H.; Weber, K. H.; Zhang, J., Thermal Decomposition of T-Amyl Methyl Ether (TAME) Studied by Flash Pyrolysis/Supersonic Expansion/Vacuum Ultraviolet Photoionization Time-of-Flight Mass Spectrometry. *Int. J. Mass Spectrom.* **2011**, *306*, 210-218.
36. Cooper, G.; Anderson, J. E.; Brion, C. E., Absolute Photoabsorption and Photoionization of Formaldehyde in the VUV and Soft X-Ray Regions (3–200 eV). *Chem. Phys.* **1996**, *209*, 61-77.
37. Cool, T. A.; Nakajima, K.; Mostefaoui, T. A.; Qi, F.; McIlroy, A.; Westmoreland, P. R.; Law, M. E.; Poisson, L.; Peterka, D. S.; Ahmed, M., Selective Detection of Isomers with Photoionization Mass Spectrometry for Studies of Hydrocarbon Flame Chemistry. *J. Chem. Phys.* **2003**, *119*, 8356-8365.

38. Wang, J.; Yang, B.; Cool, T. A.; Hansen, N.; Kasper, T., Near-Threshold Absolute Photoionization Cross-Sections of Some Reaction Intermediates in Combustion. *Int. J. Mass Spectrom.* **2008**, *269*, 210-220.
39. Staley, R. H.; Wieting, R. D.; Beauchamp, J. L., Carbenium Ion Stabilities in the Gas Phase and Solution. An Ion Cyclotron Resonance Study of Bromide Transfer Reactions Involving Alkali Ions, Alkyl Carbenium Ions, Acyl Cations and Cyclic Halonium Ions. *J. Am. Chem. Soc.* **1977**, *99*, 5964–5972.
40. Traeger, J. C.; McLoughlin, R. G.; Nicholson, A. J. C., Heat of Formation for Acetyl Cation in the Gas Phase. *J. Am. Chem. Soc.* **1982**, *104*, 5318–5322.
41. Trott, W. M.; Blais, N. C.; Walters, E. A., Molecular Beam Photoionization Study of Acetone and Acetone-d<sub>6</sub>. *J. Chem. Phys.* **1978**, *69*, 3150-3158.
42. Czekner, J.; Taatjes, C. A.; Osborn, D. L.; Meloni, G., Absolute Photoionization Cross-Sections of Selected Furanic and Lactonic Potential Biofuels. *Int. J. Mass Spectrom.* **2013**, *348*, 39-46.
43. von Niessen, W.; Bieri, G.; Åsbirnk, L., 30.4-mn He(H) Photoelectron Spectra of Organic Melcules Part III. Oxo-compounds (C, H, O)\*. *J. Electron Spectrosc. Relat. Phenom.* **1980**, *21*, 175-191.
44. Yang, B.; Wang, J.; Cool, T. A.; Hansen, N.; Skeen, S.; Osborn, D. L., Absolute Photoionization Cross-Sections of Some Combustion Intermediates. *Int. J. Mass Spectrom.* **2012**, *309*, 118-128.
45. Bouchoux, G.; Alcaraz, C.; Dutuit, O.; Nguyen, M. T., A Photoionization and Molecular Orbital Study of Cyclobutanol and Cyclobutylamine Radical Cations. *Int. J. Mass Spectrom. Ion Processes* **1994**, *137*, 93–106.
46. Sirjean, B.; Fournet, R.; Glaude, P.-A.; Ruiz-López, M. F., Extension of the Composite CBS-QB3 Method to Singlet Diradical Calculations. *Chem. Phys. Lett.* **2007**, *435*, 152-156.
47. Bobeldijk, M.; Zande, W. J. v. d.; Kistemaker, P. G., Simple Models for the Calculation of Photoionization and Electron Impact Ionization Cross Sections of Polyatomic Molecules. *Chem. Phys.* **1994**, *179*, 125-130.
48. Koizumi, H.; Schatz, G. C.; Gordon, M. S., An Analytical Representation of the Lowest Potential Energy Surface for the Reaction O(<sup>3</sup>P)+HCl ( $X^1\Sigma^+$ )→OH( $X^2\Pi$ )+Cl(<sup>2</sup>P). *J Chem. Phys.* **1991**, *95*, 6421-6428.

## 5.10 Figures and Tables

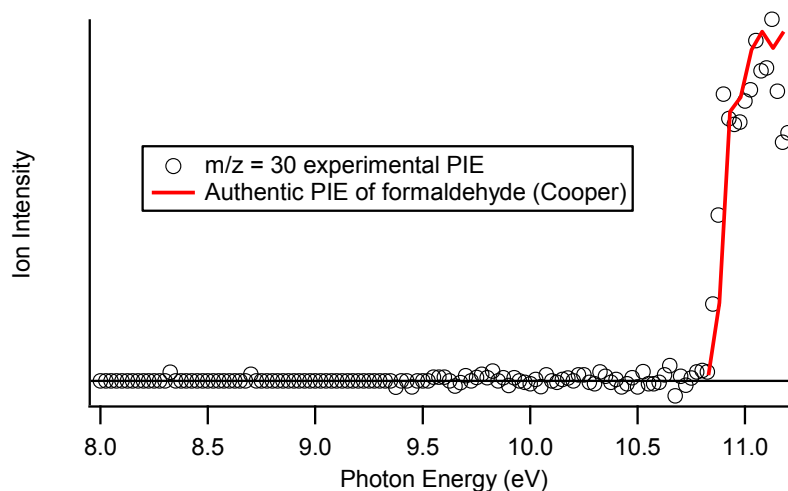


**Figure 5-1.** The literature photoionization spectrum of formaldehyde (red line) recorded by Cooper<sup>36</sup> superimposed onto the experimental photoionization spectrum of the  $m/z = 30$  (black open circles) product at 298 K.

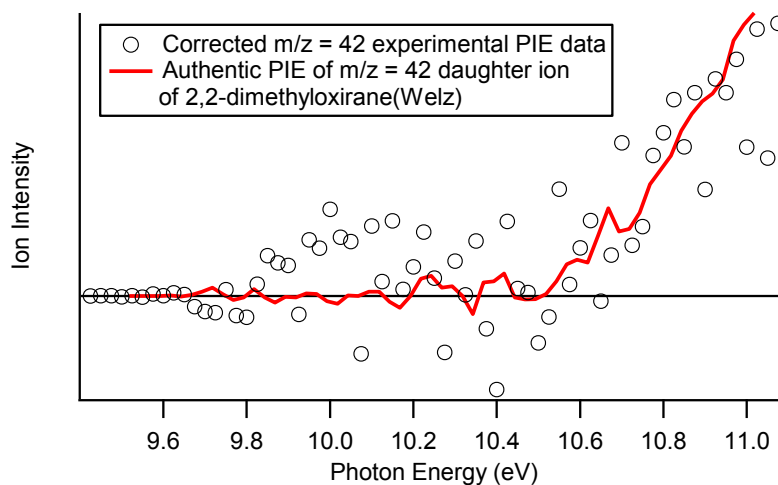


**Figure 5-2.** The authentic photoionization spectrum of  $m/z = 42$  daughter ion of 2,2-dimethyloxirane (red line) recorded by Welz<sup>23</sup> and the experimental photoionization spectrum of  $m/z = 42$  product (black open circles) at 298 K.

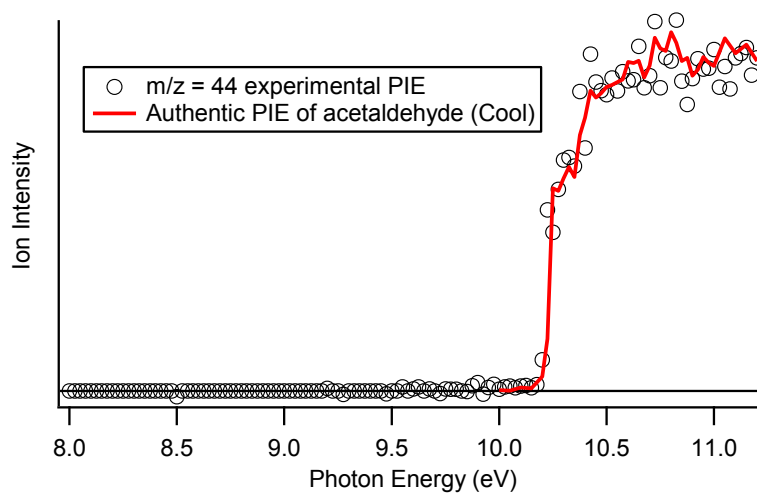


**Figure 5-3.** The literature photoionization spectrum of acetaldehyde (red line) recorded by Cool<sup>37</sup> superimposed onto the experimental photoionization spectrum of the  $m/z = 44$  (black open circles) product at 298 K.

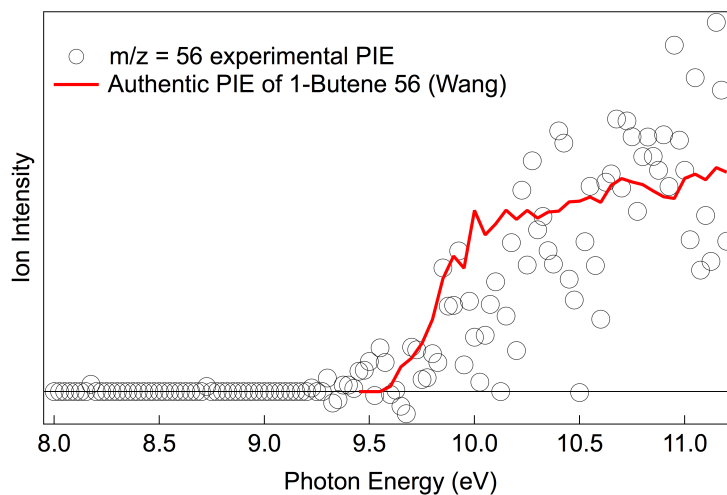


**Figure 5-4.** The literature photoionization efficiency spectrum of 1-butene<sup>38</sup> (red line) superimposed onto the experimental photoionization spectrum of the  $m/z = 56$  signal (black open circles) at 298 K.

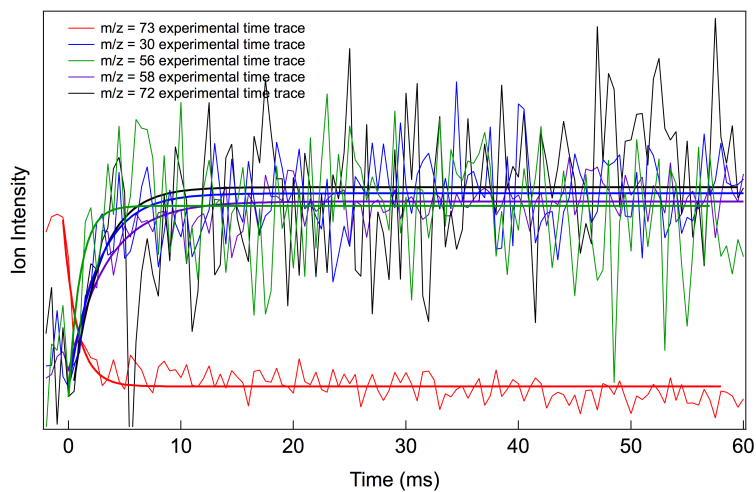


**Figure 5-5.** The comparison of the experimental time traces of  $m/z = 30$  (blue line),  $m/z = 56$  (green line),  $m/z = 58$  (purple line) and  $m/z = 72$  (black line) at 298 K with the depletion of the main dissociative ionization fragment of TAME ( $m/z = 73$ , red line).

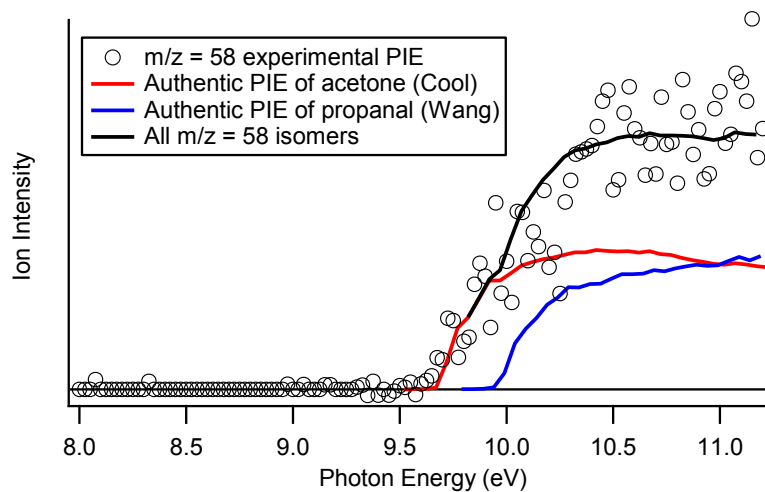


**Figure 5-6.** The summation (black line) of the literature photoionization energy spectra of acetone<sup>39-41</sup> (red line) and propanal<sup>38</sup> (blue line) superimposed onto the experimental photoionization spectrum of the  $m/z = 58$  signal (black open circles) at 298 K.

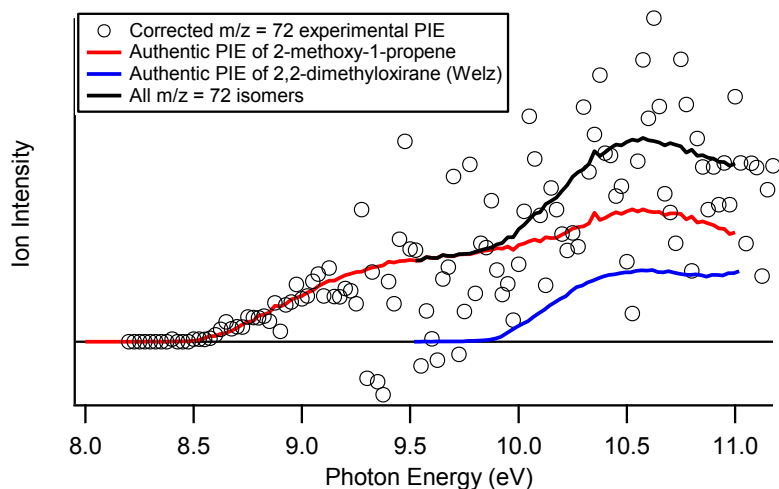


**Figure 5-7.** The summation (black line) of the authentic photoionization energy spectra of 2-methoxy-1-propene (red line) and 2,2-dimethyloxirane<sup>23</sup> (blue line) superimposed onto the corrected experimental photoionization spectrum of the  $m/z = 72$  signal (black open circles) at 298 K.

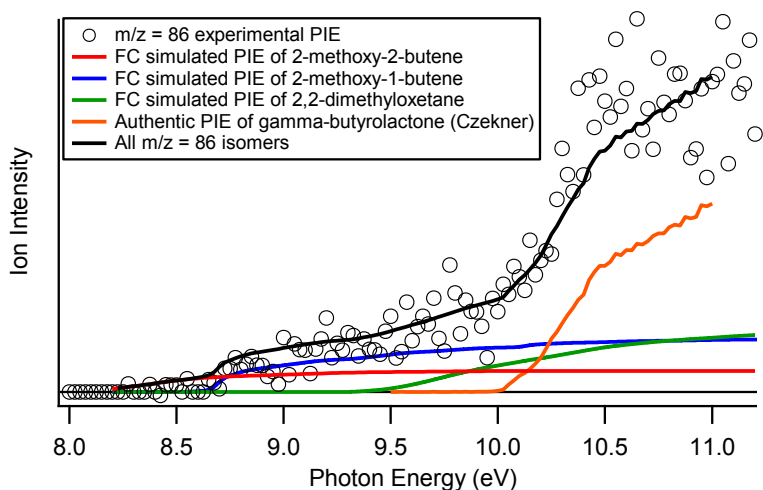


**Figure 5-8.** The summation (black line) of the Franck Condon simulated photoionization energy spectra of 2-methoxy-2-butene (red line), 2-methoxy-1-butene (blue line), 2,2-dimethyloxitane (green line), and the literature photoionization energy spectrum of  $\gamma$ -butyrolactone<sup>42</sup> (orange line) superimposed onto the corrected experimental photoionization spectrum of the  $m/z = 86$  signal (black open circles) at 298 K.



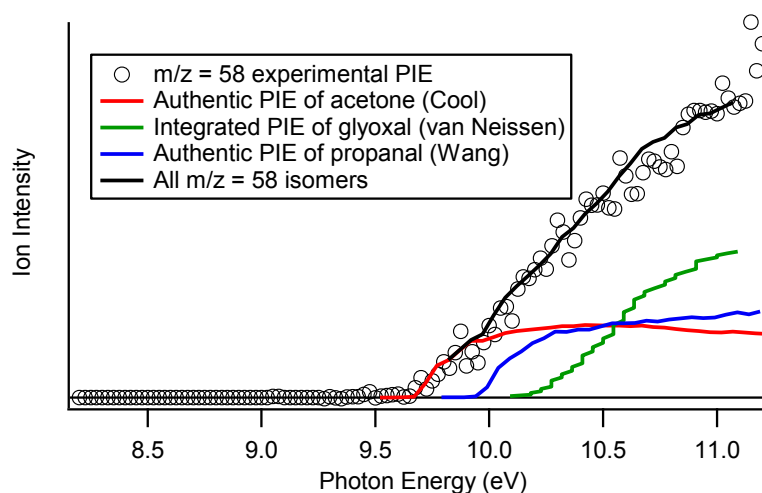


**Figure 5-9.** The summation (black line) of the literature photoionization spectrum of acetone<sup>28</sup> (red line), propanal<sup>38</sup> (green line), and the integrated photoionization energy spectrum of glyoxal<sup>43</sup> (blue line) superimposed onto the experimental photoionization spectrum of the  $m/z = 58$  signal (black open circles) at 550 K.

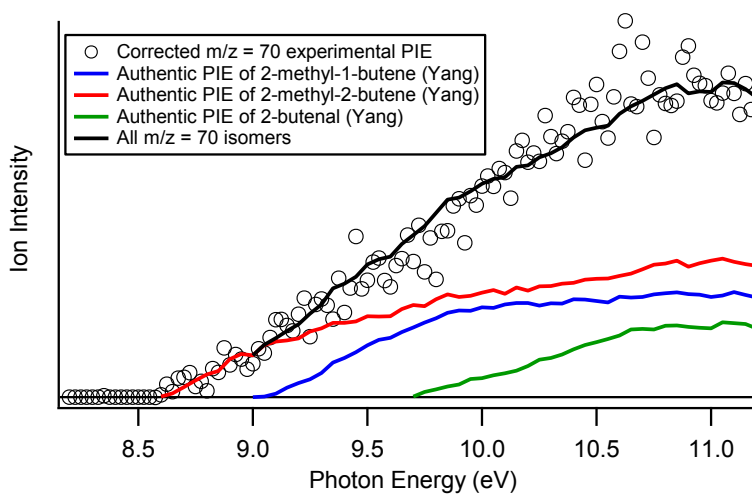


**Figure 5-10.** The summation (black line) of the literature photoionization energy spectra of 2-methyl-1-butene (red line), 2-methyl-2-butene (blue line), and 2-butenal<sup>44</sup> (green line) superimposed onto the experimental photoionization spectrum of the  $m/z = 70$  signal (black open circles) at 550 K.

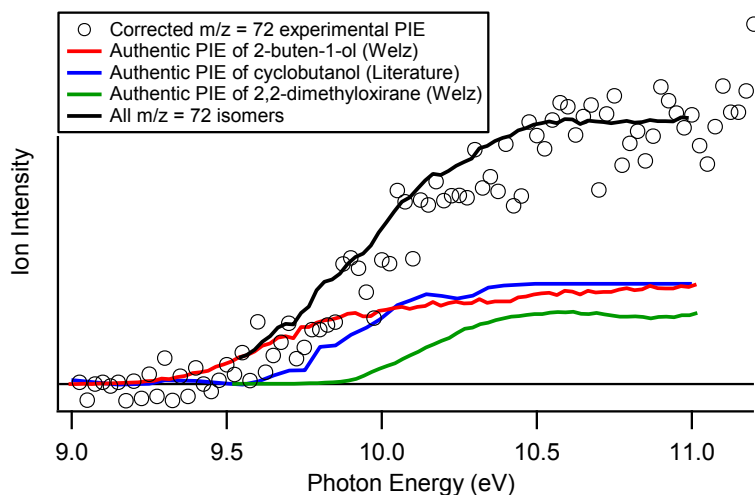


**Figure 5-11.** The summation (black line) of the literature photoionization energy spectra of 2-buten-1-ol<sup>23</sup> (red line), cyclobutanol<sup>45</sup> (blue line), and 2,2-dimethyloxirane<sup>23</sup> (green line) superimposed onto the corrected experimental photoionization spectrum of the  $m/z = 72$  signal (black open circles) at 550 K.

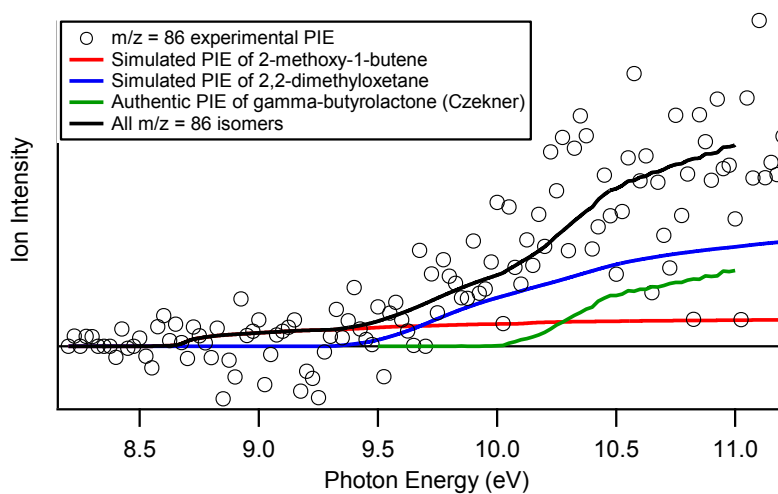


**Figure 5-12.** The summation (black line) of the Franck Condon simulated photoionization spectra of 2-methoxy-1-butene (red line), 2,2-dimethyloxetane (blue line), and the literature photoionization energy spectrum of  $\gamma$ -butyrolactone<sup>42</sup> (green line) superimposed onto the experimental photoionization spectrum of the  $m/z = 86$  signal (black open circles) at 550 K.

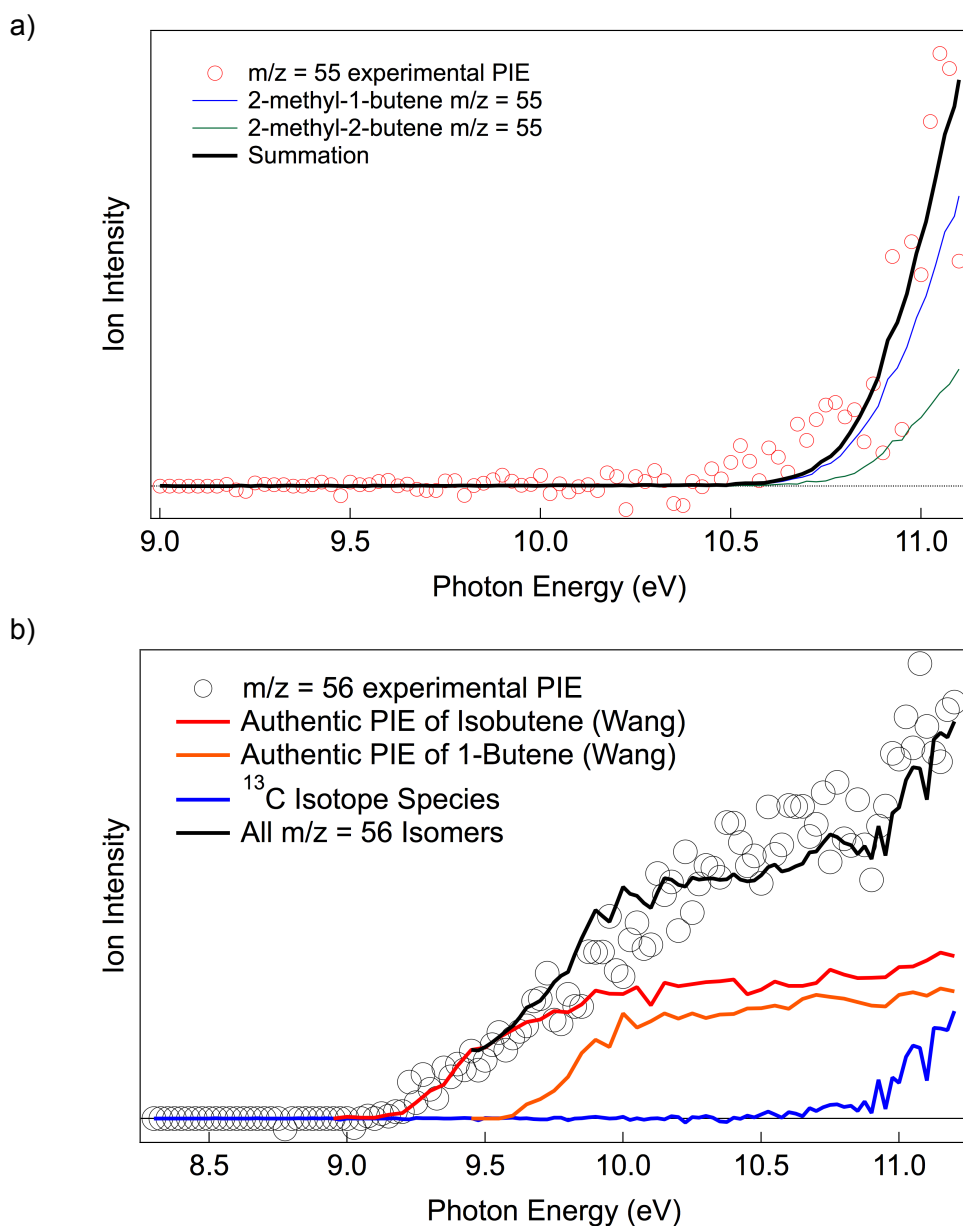


**Figure 5-13.** a) The comparison between the photoionization spectrum of  $m/z = 55$  and the dissociative ionization fragments ( $\text{C}_4\text{H}_9^+$ ,  $m/z = 55$ ) of 2-methyl-1-butene and 2-methyl-2-butene ( $\text{C}_4\text{H}_9^+$ ,  $m/z = 55$ ). b) The summation (black line) of literature photoionization spectra of isobutene (red line)<sup>38</sup> and 1-butene (orange line)<sup>38, 48</sup> and  $^{13}\text{C}$  contribution from  $m/z = 55$  dissociative fragment of 2-methyl-1-butene and 2-methyl-2-butene superimposed onto the experimental photoionization spectrum of the  $m/z = 56$  signal (black open circles) at 700 K.

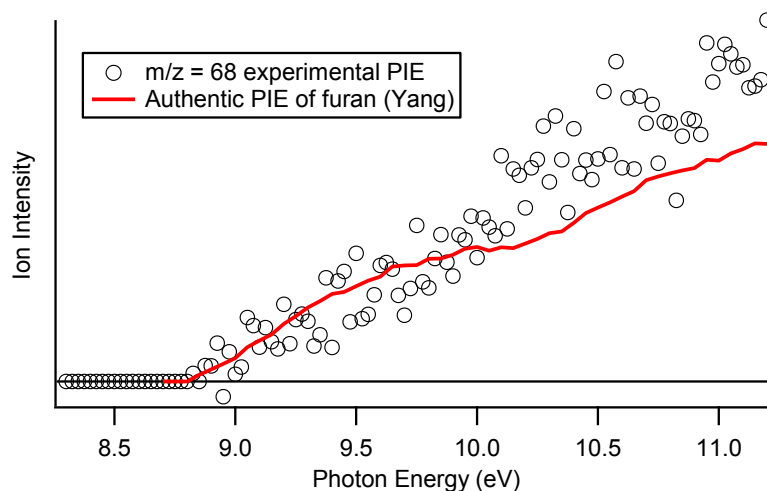


**Figure 5-14.** The literature photoionization spectrum of furan (red line) recorded by Yang<sup>44</sup> superimposed onto the experimental photoionization spectrum of the  $m/z = 68$  (black open circles) product at 700 K.

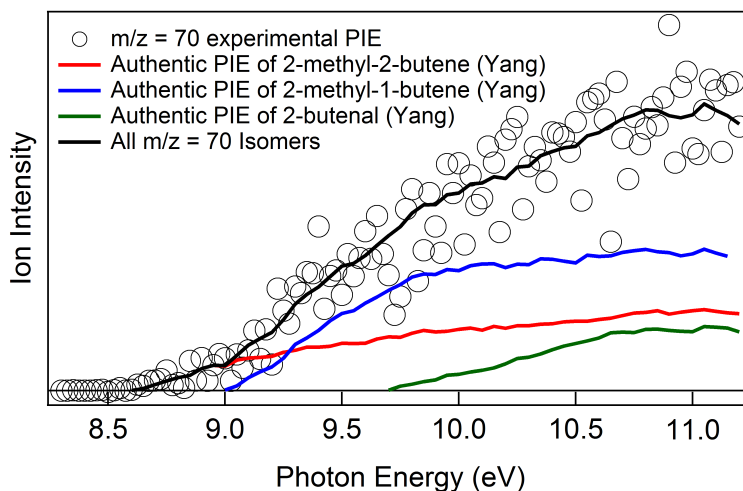
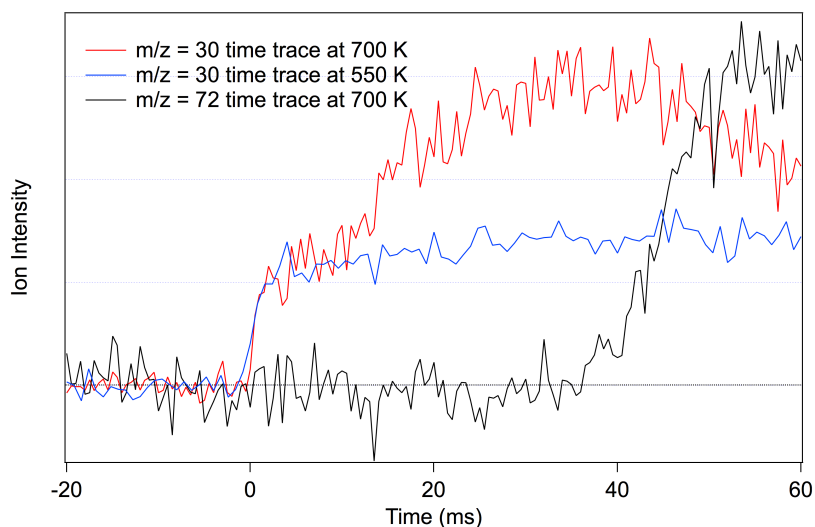


**Figure 5-15.** The summation (black line) of the literature photoionization efficiency spectra of 2-methyl-1-butene (red line), 2-methyl-2-butene (blue line), and 2-butenal<sup>44</sup> (green line) superimposed onto the experimental photoionization spectrum of the  $m/z = 70$  signal (black open circles) at 700 K.

a)



b)

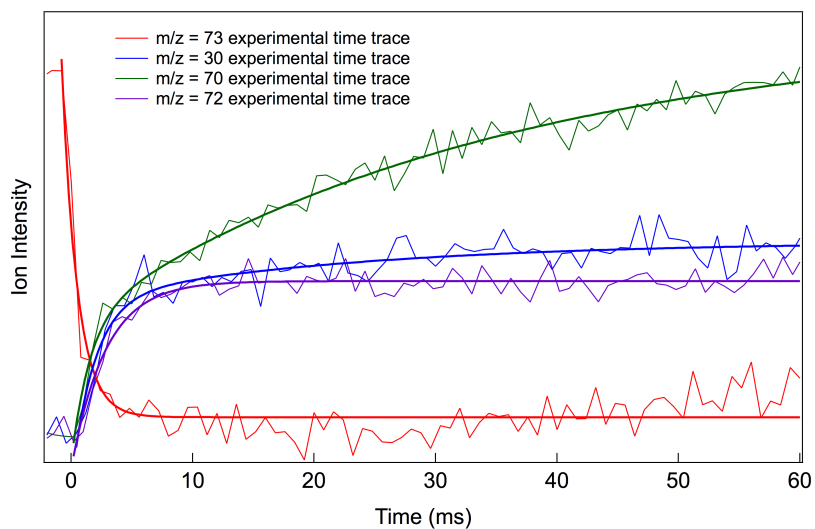


**Figure 5-16.** a) The comparison of the experimental time traces of  $m/z = 30$  (red line at 700 K and blue line at 550 K) and  $m/z = 72$  (black line) at 700 K. b) The comparison of the experimental time traces of  $m/z = 30$  (blue line),  $m/z = 70$  (green line),  $m/z = 72$  (purple line) products with that of the decay of TAME ( $m/z = 73$ , red line) at 550 K.

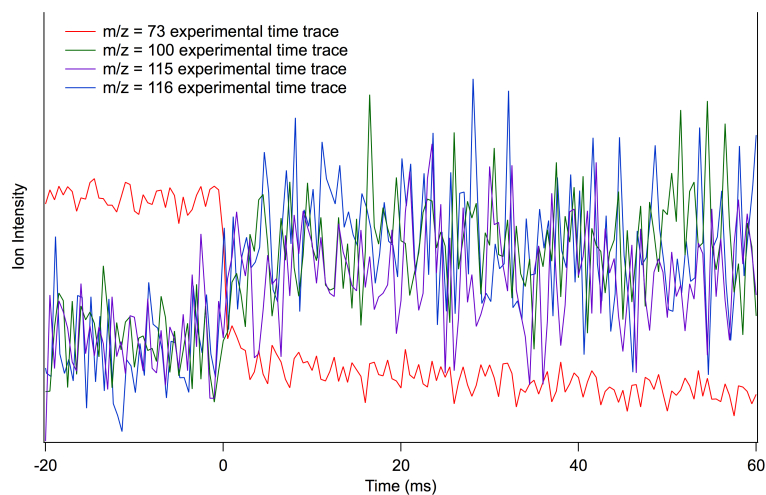


**Figure 5-17.** The comparison of the experimental time traces of  $m/z = 73$ , 100, 115, and 116 at 298 K.

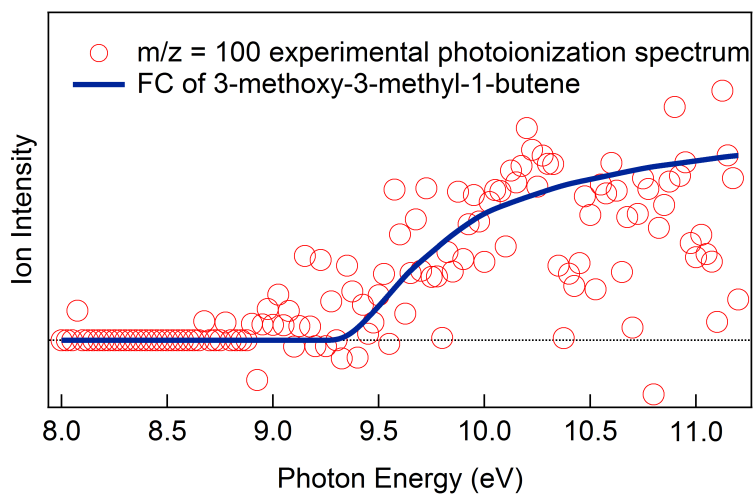


**Figure 5-18.** The  $m/z = 100$  experimental photoionization spectrum and the simulated photoionization spectrum of 3-methoxy-3-methyl-1-butene in the TAME + Cl + O<sub>2</sub> reaction at 298 K.

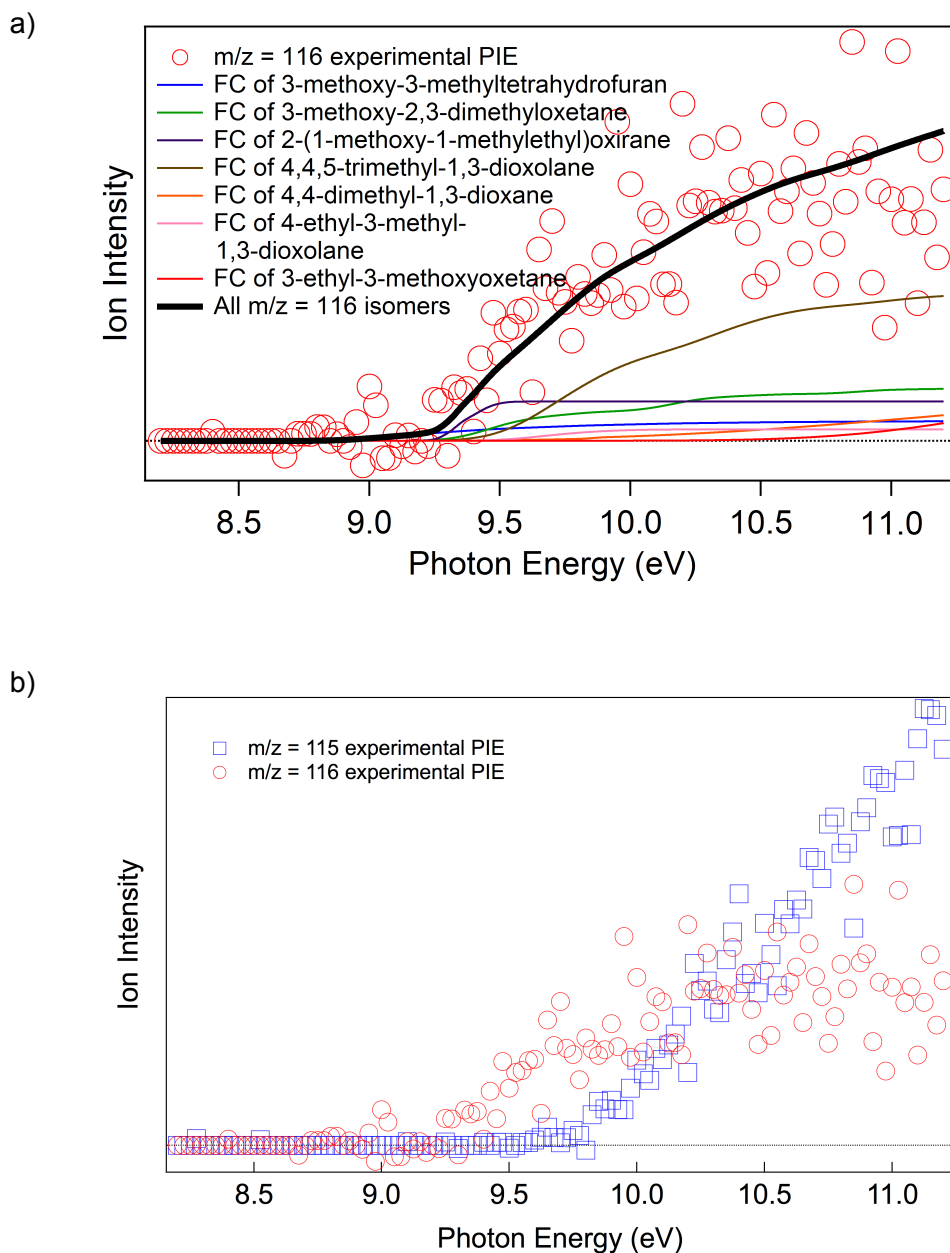


**Figure 5-19.** a) The summation of the simulated photoionization spectra of 3-methoxy-3-methyltetrahydrofuran, 3-methoxy-2,3-dimethyloxetane, 2-(1-methoxy-1-methylethyl)oxirane, 4,4,5-trimethyl-1,3-dioxolane, 4,4-dimethyl-1,3-dioxane, 4-ethyl-3-methyl-1,3-dioxolane and 3-ethyl-3-methoxyoxetane agrees well with the experimental photoionization spectrum of  $m/z = 116$  in the TAME + Cl + O<sub>2</sub> reaction at 550 K. b)  $m/z = 115$  product ionizes at a higher photon energy than  $m/z = 116$  at 298 K.

**Table 5-1.** The branching fractions for products of the reaction TAME + Cl in the presence of O<sub>2</sub> at each experimental temperature.

Compound	m/z	298 K	550 K	700 K
Formaldehyde	30	10	13	14
Acetone	58	3	3	2
2-methyl-1-butene	70	Not present	44	39
2-methyl-2-butene	70	Not present	15	10
2-methoxy-1-propene	72	8	8	1
2-methoxy-1-butene	86	Insignificant	2	Insignificant
2,2-dimethyloxetane	86	Insignificant	Insignificant	1
3-methoxy-3-methyl-1-butene	100	Insignificant	Insignificant	Insignificant
m/z = 116 isomers	116	Insignificant	Insignificant	Insignificant
<b>Total (%)</b>		<b>22</b>	<b>85</b>	<b>67</b>

**Table 5-2.** Estimated Photoionization Cross-Section Using the Bobeldijk method<sup>47</sup>

Name	m/z	Photoionization Cross-Section (Mb) at 11 eV
2-methoxy-1-butene	86	37.7
2,2-dimethyloxetane	86	35.9
2,2-diethyloxirane	86	42.0
3-methoxy-3-methyl-1-butene	100	40.6
3-methoxy-3-methyltetrahydrofuran	116	59.2
3-methoxy-2,3-dimethyloxetane	116	57.6
2-(2-methoxypropan-2-yl)oxirane	116	60.0
4,4,5-trimethyl-1,3-dioxolane	116	55.9
4,4-dimethyl-1,3-dioxane	116	32.3
4-ethyl-4-methyl-1,3-dioxolane	116	35.9
3-ethyl-3-methoxyoxetane	116	14.5



**Table 5-3.** Estimated Branching Fractions of  $m/z = 100$  and  $116$  Using the Bobeldijk method<sup>47</sup>

Name	$m/z$	298 K	550 K	700 K
3-methoxy-3-methyltetrahydrofuran	116	0.05%	0.02%	0.01%
3-methoxy-2,3-dimethyloxetane	116	0.02%	0.07%	0.04%
2-(2-methoxypropan-2-yl)oxirane	116	0.01%	0.05%	0.02%
4,4,5-trimethyl-1,3-dioxolane	116	0.01%	0.19%	0.01%
4,4-dimethyl-1,3-dioxane	116	0.03%	0.05%	0.03%
4-ethyl-4-methyl-1,3-dioxolane	116	0.01%	0.02%	0.02%
3-ethyl-3-methoxyoxetane	116	0.03%	0.05%	0.02%
3-methoxy-2,3-dimethyloxetane	116	0.05%	0.02%	0.01%